UNIVERSITY OF ROCHESTER
LABORATORY FOR LASER ENERGETICS

Volume 158
January–March 2019
DOE/NA/3856-1498

LLE Review

Quarterly Report

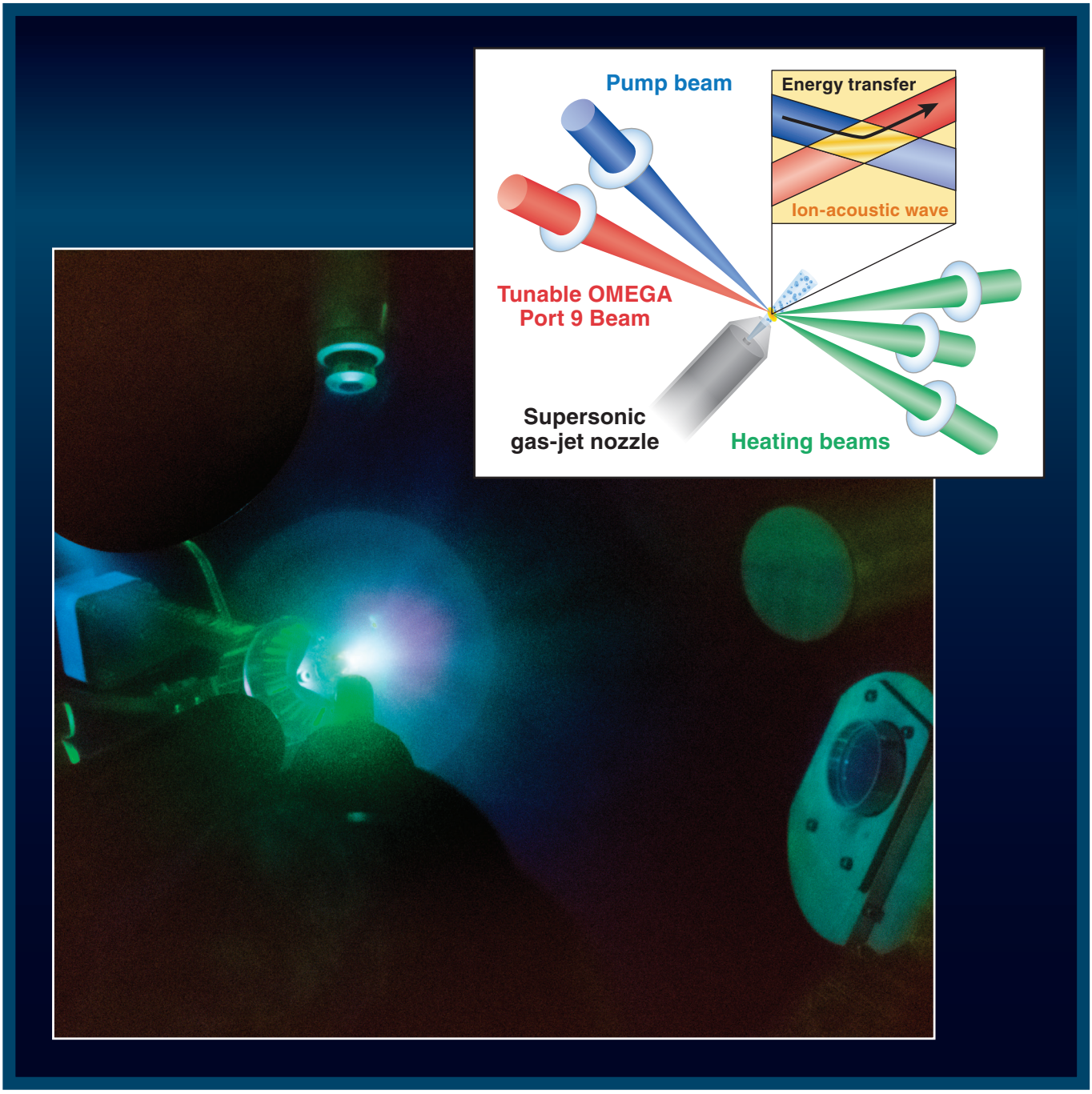

About the Cover:

The cover photo shows the Tunable OMEGA P9 (TOP9) beam firing in a cross-beam energy transfer experiment. OMEGA heater and pump beams, as well as the TOP9, interact in a supersonic flow of plasma delivered by a gas jet (left center) inserted into the target chamber. Thomson-scattered radiation is collected with a re-entrant reflective telescope (lower right). The beam geometry for this experiment is shown as a schematic in the inset. This flexible and comprehensive experimental and diagnostic suite enables critical research into the fundamental behavior of plasmas under the influence of laser radiation. In this volume we feature two such examples of work in this area: Evidence of the distortion of electron distribution function from laser-plasma heating (p. 63), a resolution to a decades-old prediction in plasma physics; and a look to the future of laser–plasma interactions (p. 75) enabled by emerging technologies.

The TOP9 beam originates in the OMEGA EP Laser Bay (left) where it is then transported across the laboratory to the OMEGA Target Bay (right) to be directed into the target chamber for experiments.

The work described in this volume includes current research at the Laboratory for Laser Energetics, which is supported by New York State Energy Research and Development Authority, the University of Rochester, the U.S. Department of Energy Office of Inertial Confinement Fusion under Cooperative Agreement No. DE-NA0003856, and other agencies.

Printed in the United States of America
Available from
National Technical Information Services
U.S. Department of Commerce
5285 Port Royal Road
Springfield, VA 22161
www.ntis.gov

For questions or comments, contact Steven T. Ivancic, Editor, Laboratory for Laser Energetics, 250 East River Road, Rochester, NY 14623-1299, (585) 275-5515.

www.lle.rochester.edu

UNIVERSITY OF ROCHESTER
LABORATORY FOR LASER ENERGETICS

Volume 158
January–March 2019
DOE/NA/3856-1498

LLE Review

Quarterly Report

UR LLE

Contents

In Brief

This volume of LLE Review 158, covering the period January–March 2019, is sectioned among research areas at LLE and external users of the Omega Laser Facility. Articles appearing in this volume are the principal summarized results of long-form research articles. Readers seeking a more-detailed account of research activities are invited to seek out the primary materials appearing in print, detailed in the publications and presentations section at the end of this volume.

Highlights of research presented in this volume include the following:

- D. Turnbull *et al*. present measurements indicating the presence of super-Gaussian electron distribution functions in laser-heated plasmas consistent with the predictions of Langdon *et al*. (p. 63). Standard Maxwellian calculations of electron distribution function overpredict power transfer in cross-beam energy transfer compared with the observed super-Gaussian distribution.

- D. Cao *et al*. present findings on the interpretation of x-ray–inferred electron temperature for direct-drive inertial confinement fusion (ICF) implosions on OMEGA (p. 65). The electron temperature inferred from hard x-ray continuum emission was shown to be an emission-weighted, harmonic mean electron temperature.

- S. C. Miller *et al*. investigate fuel–shell interface instability growth in warm shell surrogate implosions on OMEGA for different fuel compositions (p. 69). It was found that the hot spot is relatively insensitive to changes in the deuterium:tritium ratio, in accordance with 2-D *DRACO* simulations.

- A. Kar *et al*. introduce a method to measure laser-driven shocks using refraction-enhanced x-ray radiography (REXR) at the shock interface (p. 72). REXR provides information during critical moments in shock formation, when velocity interferometers do not provide any information as a result of blanking from x-ray photoionization.

- J. P. Palastro *et al*. present a white paper detailing opportunities for laser–plasma interactions made possible by emerging technologies (p. 75). *Plasma optics*, i.e., optical components consisting of plasma with tailored dielectric properties, can provide the disruptive technology to enable high-intensity laser research for decades to come.

- P. M. Nilson *et al*. present a technique for studying laser-driven magnetic reconnection in the laboratory (p. 84). Proton radiography was used to demonstrate the technique by mapping the changes in magnetic connectivity at the target surface. The data show where the magnetic fields are located, where they are transported, how they merge and reconnect, and where they reside post reconnection.

- A. M. Hansen *et al*. demonstrate a new method for mitigating self-focusing of probe radiation in Thomson-scattering experiments (p. 87). The Thomson-scattered signal-to-noise ratio can be improved by 10× using a distributed phase plate, effectively distributing the laser's power across many lower power speckles.

- R. K. Follett *et al*. define thresholds for absolute laser–plasma instabilities driven by a broadband laser (p. 89). Calculations suggest that the threshold can be increased by 2× with 1.5% bandwidth of the broadband laser.

- A. J. Tu *et al*. detail a complex ray-tracing and cross-beam energy transfer code for laser-plasma simulations (p. 92). The new algorithm performs calculations 10× faster than previous cross-beam energy transfer codes.

- M. Zaghoo presents new thermodynamic constraints on the mechanical, thermal, and magnetic properties of super-Earth–sized planets (p. 95). The results support the concept of "super-habitability" in which some terrestrial planets have enhanced characteristics suitable for habitability.

- V. V. Karasiev *et al*. discuss exchange-correlation thermal effects in shocked deuterium (p. 97). Exchange-correlation thermal effects may become important at 0.1 Fermi temperature, where standard density functional theory codes currently consider a temperature-independent exchange correlation functional.

- J. Katz *et al*. outline a process for the spatiotemporal flat field for gated optical imagers (p. 101). In the fastest gated optical imagers, the gating process is both spatially and temporally dynamic, necessitating quantitative knowledge of the detector sensitivity to compare data recorded at different image positions.

- W. R. Donaldson and A. Consentino demonstrate the co-timing of UV and IR laser pulses on the OMEGA EP Laser System (p. 104). Typical variations are shown to be less than 20 ps in routine laser operation.

- S.-W. Bahk details the current status of chirped-pulse–amplification (CPA) technology and its applications (p. 108). CPA has revolutionized laser technology and opened the way for studying advanced science in large and small laboratories across the world.

- D. Broege and J. Bromage present measurements of heat flow from surface defects in lithium triborate (p. 111). These measurements are the first interferometric measurements of temperature distributions in a nonlinear optic resulting from absorption from a local defect.

- M. Chorel *et al*. discuss the role of Urbach tail optical absorption in the subpicosecond laser-induced damage threshold (LIDT) of hafnia and silica coatings (p. 113). The results suggest the presence of a correlation between absorption at the Urbach tail to the coating's intrinsic LIDT at 1053 nm with subpicosecond pulses.

- T. Z. Kosc *et al*. present a method of measuring angularly dependent spontaneous Raman scattering in crystalline materials (p. 115). This new and flexible configuration makes it possible to measure any crystal cut in any pump or probe configuration.

- D. R. Harding *et al*. compare shadowgraphy and x-ray phase contrast methods for the characterization of DT ice layers in ICF targets (p. 118). It is shown that x-ray phase contrast provides the best assessment of low-mode roughness, while shadowgraphy provides the best contrast for detecting individual grooves in an ice layer.

- B. S. Rice *et al*. have developed a method to predict DT ice-layer uniformity in ICF capsules (p. 120). The predictive capability is developed through a multiphase heat-transfer numerical model.

- K. Kopp and S. G. Demos introduce a curriculum for microscopy with ultraviolet surface excitation (MUSE) into a high school science classroom (p. 122). MUSE can eliminate the need for lengthy microscope slide fixation and preparation, providing a far more engaging experience for biology and physics students.

- J. Puth *et al*. summarize operations of the Omega Laser Facility during the second quarter of the FY19 reporting period (p. 124).

Steven T. Ivancic
Editor

Impact of the Langdon Effect on Cross-Beam Energy Transfer

D. Turnbull,[1] A. Colaïtis,[1,2] A. M. Hansen,[1] A. L. Milder,[1,2] J. P. Palastro,[1] J. Katz,[1] C. Dorrer,[1] B. E. Kruschwitz,[1] D. J. Strozzi,[3] and D. H. Froula[1]

[1]Laboratory for Laser Energetics, University of Rochester
[2]Centre National da la Recherche Scientifique
[3]Lawrence Livermore National Laboratory

The prediction that laser-plasma heating distorts the electron distribution function (EDF) away from Maxwellian dates back four decades.[1] In conditions relevant to laser-based fusion, however, no direct evidence of this so-called "Langdon effect" has previously been observed. Here, measurements of the complete Thomson-scattering spectrum indicate the presence of super-Gaussian EDF's that are consistent with Langdon theory. In such plasmas, ion-acoustic wave (IAW) frequencies increase monotonically with super-Gaussian exponent.[2] To match experiments that measured power transfer between crossed laser beams mediated by IAW's, a model that accounts for the non-Maxwellian EDF is required, whereas the standard Maxwellian calculations overpredict power transfer over a wide region of parameter space. Including this effect is expected to improve the predictive capability of cross-beam energy transfer (CBET) modeling at the National Ignition Facility (NIF) and may restore a larger operable design space for inertial confinement fusion experiments. This is also expected to motivate further inquiry in other areas impacted by non-Maxwellian EDF's, such as laser absorption, heat transport, and x-ray spectroscopy.

Laser fusion experiments require many overlapping laser beams to propagate through long, underdense plasmas in order to precisely deposit their energy at desired locations, but laser–plasma interactions can complicate the intended result. Cross-beam energy transfer is one example, whereby a frequency difference between two lasers in the plasma rest frame resonantly drives an ion-acoustic wave that scatters light from one beam to the other. The ability to manipulate this process in indirect-drive hohlraum targets via laser frequency detuning was initially seen as beneficial, providing control over implosion symmetry while operating the NIF at its maximum energy. However, when integrated observables indicated that there was less CBET than calculated, a tunable saturation clamp on IAW amplitudes was added to models, although the level ($\delta n/n = 10^{-3}$ to 10^{-4}) was too small to be explained by known saturation mechanisms.[3] Moreover, it varied between platforms—undermining the predictive capability of simulations and limiting fusion performance.

This motivated the development of a CBET platform at LLE, where a wavelength-tunable laser (TOP9) was built to study CBET in a well-characterized quasi-stationary plasma. Initial experiments reported here suggest that the Langdon effect may be responsible for overpredicting power transfer in indirect-drive–relevant conditions. The term comes from a 1980 Letter in which A. B. Langdon explained that inverse bremsstrahlung absorption of electromagnetic radiation in plasma preferentially heats low-energy electrons, distorting the electron distribution function away from Maxwellian and toward a super-Gaussian of the order of $m = 5$ (Ref. 1). He defined the scaling parameter $\alpha = Z_{\text{eff}} v_{\text{osc}}^2 \big/ v_{\text{th}}^2$, where Z_{eff} is the effective ion charge state, v_{osc} is the velocity of electrons oscillating in the laser field, and v_{th} is the electron thermal velocity. Subsequent Fokker–Planck simulations under a wide range of laser heating conditions demonstrated that intermediate super-Gaussian EDF's are produced in the form $f_m(v) = C_m \exp[-(v/v_m)^m]$, where $v_m^2 = \left(3k_{\text{B}}T_{\text{e}} \big/ M_{\text{e}}\right)\left[\Gamma(3/m)/\Gamma(5/m)\right]$, $C_m = \left(N_{\text{e}} \big/ 4\pi\right)\left\{m \Big/ \left[\Gamma\left(3/m\right) v_m^3\right]\right\}$, Γ is the gamma function, and $m(\alpha) = 2 + 3\Big/\left(1 + 1.66\Big/\alpha^{0.724}\right)$ is only a function of α (Ref. 4).

Although it is often assumed that the Langdon effect only impacts absorption in high-Z plasmas, such non-Maxwellian distribution functions are known to affect the ion-acoustic wave dispersion relation $\omega = kc_{\text{s}}[3\Gamma^2(3/m)/\Gamma(1/m)/\Gamma(5/m)]^{1/2}$, which would

directly impact CBET by shifting the ion-acoustic resonance.[2] The square root term modifies the usual dispersion relation and leads to a monotonic increase of IAW frequency with super-Gaussian order, which results from the smaller number of low-energy electrons [$f(v \approx 0)$] available to shield the ion oscillations.

In the CBET experiments, TOP9 was crossed with a single nearly co-propagating pump beam in a plasma that was preformed from a mixture of hydrogen and nitrogen gas; its power was then diagnosed using a transmitted beam diagnostic. Results will be shown with and without nearly counter-propagating heater beams, which (when present) enhanced the Langdon effect without contributing significantly to the CBET gain. Both spatially and temporally resolved Thomson scattering were used to characterize the plasma conditions (including m) in order to constrain the CBET modeling. A heater-only intensity (I) scan was performed by varying the number of beams from 1 to 4. In addition to electron temperature increasing with I to the ≈0.2 power, the non-Maxwellian super-Gaussian exponent m was observed to increase from 2.4 up to 2.85 in excellent agreement with theory.

On the CBET experiments with three heaters plus one pump, m was determined to be 2.82 from the Thomson-scattering spectrum, whereas it was only 2.4 for the case of the pump only. In the former case, accounting for the non-Maxwellian EDF (again, using the modified electron susceptibility) was required to match the data, whereas the standard Maxwellian model currently used in inertial fusion calculations overpredicted the energy transfer [shown in Fig. 1(a)]. Without heater beams, the effect is smaller and the data cannot easily distinguish between the Maxwellian and non-Maxwellian models [Fig. 1(b)]. Calculations for NIF-like plasma conditions yield $\alpha = 0.7$ and $m = 2.96$—even further from Maxwellian than the conditions produced in the TOP9 experiments because of the large number of overlapping beams. Since the Langdon effect suppresses gain on the rising edge of the ion-acoustic resonance and most resonances are outside the NIF's available wavelength tuning range in an indirect-drive fusion experiment, calculations suggest the Langdon effect uniformly reduces CBET gain on the NIF by 27.7% on average. This level of CBET reduction would significantly impact implosion symmetry. Accounting for the Langdon effect might therefore remove the need for an artificial saturation clamp and should improve the predictive capability of integrated modeling.

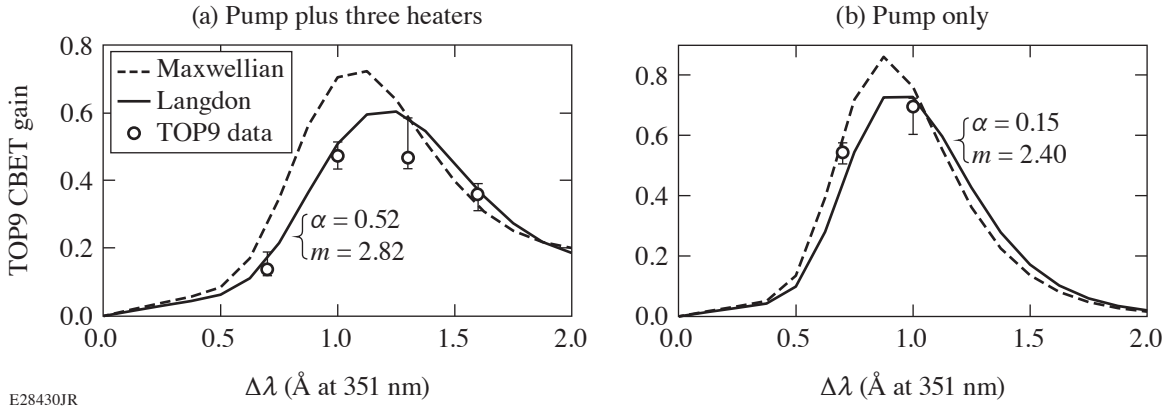

Figure 1
TOP9 CBET results. (a) TOP9 data are shown for the case in which three heater beams coexisted temporally with the pump and wavelength-tunable beam. A calculation that accounts for the non-Maxwellian EDF measured by Thomson scattering agrees with the data, but the Maxwellian calculation is discrepant. (b) Without the heater beams, the EDF was closer to Maxwellian and the data cannot easily distinguish between the two models.

This material is based upon work supported by the Department of Energy National Nuclear Security Administration under Award Number DE-NA0003856, the University of Rochester, and the New York State Energy Research and Development Authority.

1. A. B. Langdon, Phys. Rev. Lett. **44**, 575 (1980).

2. B. B. Afeyan *et al.*, Phys. Rev. Lett. **80**, 2322 (1998).

3. P. Michel *et al.*, Phys. Rev. Lett. **109**, 195004 (2012).

4. J. P. Matte *et al.*, Plasma Phys. Control. Fusion **30**, 1665 (1988).

Interpreting the Electron Temperature Inferred from X-Ray Continuum Emission for Direct-Drive Inertial Confinement Fusion Implosions on OMEGA

D. Cao, R. C. Shah, S. P. Regan, R. Epstein, I. V. Igumenshchev, V. Gopalaswamy, A. R. Christopherson, W. Theobald, P. B. Radha, and V. N. Goncharov

Laboratory for Laser Energetics, University of Rochester

We present findings on which the x-ray–inferred electron temperature T_e will be interpreted for direct-drive ICF implosions on OMEGA: (1) an analytic description of the electron temperature as the emission-weighted, harmonic mean temperature; (2) an optimal x-ray energy that gives emission weighting closest to neutron weighting; (3) simulation results showing disparity between hot-spot electron temperature and ion temperature, even without fluid motion biasing for OMEGA-scale implosions; and (4) simulation results showing correlation of the implosion degradation with the hot-spot electron temperature and x-ray yield.

It can be shown that the inferred T_e from x-ray continuum emission represents an emission-weighted, harmonic average temperature of the emitting body. From an x-ray spectrum that can be both time and spatially integrated, the emitting body's temperature can be obtained by applying a linear fit in log space and calculating that fit's negative inverse slope, as shown in Fig. 1 for an example profile. This inferred temperature is found to follow the harmonic average relation

$$\frac{1}{kT_{\text{fit}}} = \frac{1}{I_\nu}\iint \varepsilon_\nu^{\text{FF}}\left[\frac{1}{kT_e(\mathbf{r})}\right]\mathrm{d}V\mathrm{d}t = \left\langle \frac{1}{kT_e(\mathbf{r})}\right\rangle, \tag{1}$$

where T_{fit} is the inferred electron temperature, k is the Boltzmann constant, I_ν is the total x-ray yield at photon energy $h\nu$, V is the volume, t is time, T_e is the true electron temperature, and $\varepsilon_\nu^{\text{FF}}$ is the free–free bremsstrahlung emissivity assuming full ionization.

As shown in Fig. 1(c) for the example profile, results from applying Eq. (1) give the same value as performing the linear fit exercise in Fig. 1(b). Since the inferred electron temperature will be a harmonic average, it will be generally lower than an emission-weighted, arithmetic average by ~100 eV as shown in Fig. 1(c).

With a physical understanding of the inferred temperature and its weighting on photon energy, it is next important to know the photon energy most optimal for inferring the hot-spot electron temperature. Given that complementary ion temperature measurements are neutron weighted, it would be most meaningful for the electron temperature to be weighted by the same spatial distribution as the neutron emission for the purpose of assessing implosion performance. By using a power law approximation $\varepsilon_\nu^{\text{FF}} \propto T^\eta$ for the emissivity, where the exponent η is given by

$$\eta = \frac{h\nu_0}{kT_0}, \tag{2}$$

it is found that photons with energies near $4kT_0$, where T_0 is the characteristic hot-spot temperature (e.g., has a neutron-weighted temperature of ~3.75 keV for OMEGA), are produced with a T^4 dependence (i.e., the same temperature dependence as neutron

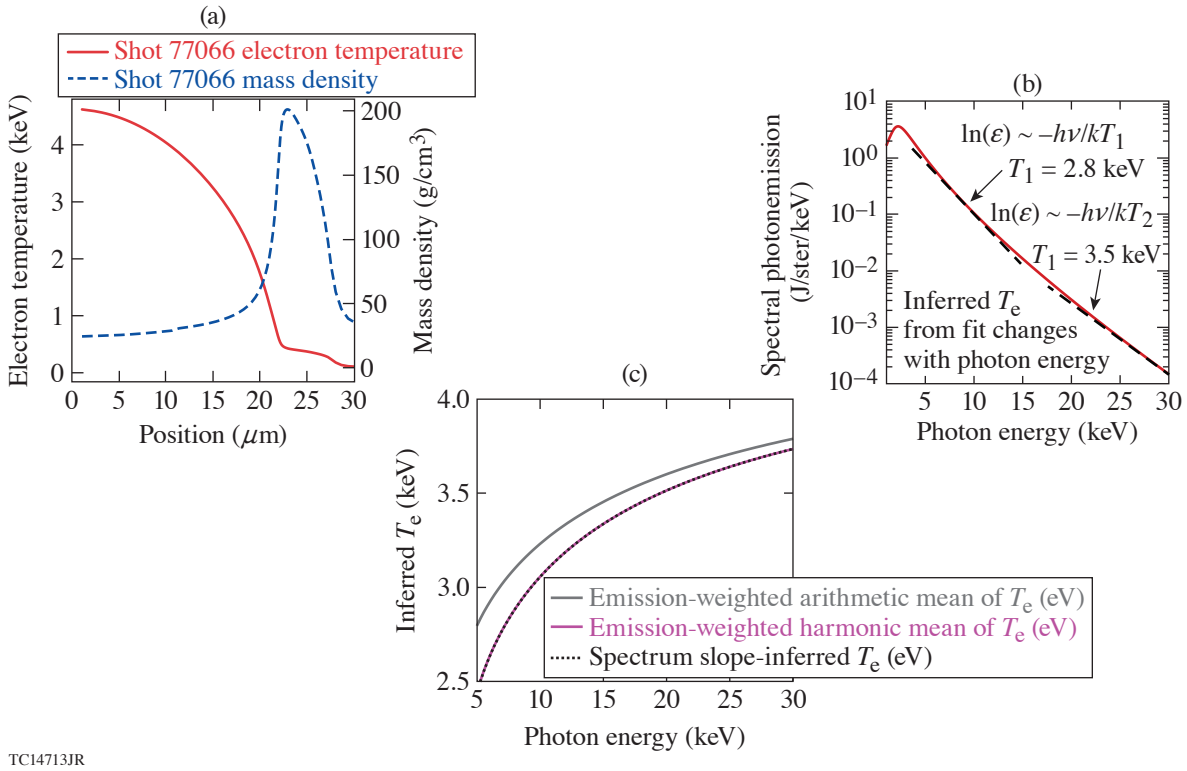

Figure 1

The process used to extract instantaneous, spatially averaged hot-spot temperature from hard x-ray emission. From a hot spot represented by the profiles in (a), the escaping photons create the x-ray spectrum[1] in (b). The electron temperature is inferred from the log slope of the spectrum in (b) and changes with photon energy caused by the distribution of temperatures within the hot spot. This in turn creates an array of slope-inferred temperatures as shown in (c). This inferred electron temperature is equivalent to the emission-weighted harmonic mean electron temperature from the hot spot and is generally lower than the emission-weighted, arithmetic mean electron temperature. A time-integrated T_e can be inferred using the same process from a time-integrated x-ray spectrum.

production from deuterium–tritium fusion). At this photon energy, the inferred electron temperature can be said to have an emission weighting that closely, but not equally, resembles neutron weighting. This can be seen in Fig. 2(a), which compares the normalized x-ray emission and neutron production for an isobaric temperature and density profile.[2]

For OMEGA-scale implosions, simulations show that the neutron-weighted ion temperature is not well approximated by the electron temperature, regardless of the photon energy used. This is shown in Fig. 2(b) using *LILAC*[3] post-shot simulations of all past DT cryogenic shots performed on OMEGA that are stored in the simulation database.[4] At all photon energies, the functional mapping between the electron temperature and the neutron-weighted ion temperature does not follow a clear $y = x$ trend. Moreover, the consequent mapping uncertainty in ion temperature can be as large as ~400 eV according to scatter in Fig. 2(b), compared to the precision error of ~130 eV from current neutron time-of-flight diagnostics on OMEGA.

This imprecise surrogacy between the ion and electron temperatures is caused by the hot spot's thermal nonequilibrium state for the simulated OMEGA implosions. The persistence of this thermal nonequilibrium can be surprising, considering that the equilibration time, which scales[5] as $\tau_{ei} \sim T^{3/2}\rho^{-1}$, is typically of the order of 10 ps or only about 10% of the burnwidth FWHM. It was found, however, that electron thermal conduction was responsible for inhibiting thermal equilibration from dominating. It is expected that hot spots will be more equilibrated for higher convergence ratio implosions at a larger scale.

Despite the non-surrogacy between the electron and ion temperatures, 3-D simulations suggest the difference of the electron temperature from the 1-D prediction $\left(\Delta T_e = T_e^{\text{inferred}} - T_e^{\text{1-D}}\right)$ can be useful as an implosion diagnostic. Figure 3 shows a comparison of the inferred electron temperature and x-ray yield between the two cases. One simulation represented an ideal case where the

implosion was perfectly 1-D and another included perturbations typically observed on OMEGA from target offset ($\Delta r = 5.4\ \mu$m), beam imbalance ($\sigma_{rms} = 3.5\%$), and beam port geometry as well as laser imprint modulations ($\ell_{max} = 200$). Both simulations use target parameters from OMEGA shot 89224, an $\alpha \sim 5$ implosion with an in-flight aspect ratio $\left(\text{IFAR} = R_{shell}/\Delta R_{shell}\right)$ of ~40 and peak implosion velocity of 480 km/s.

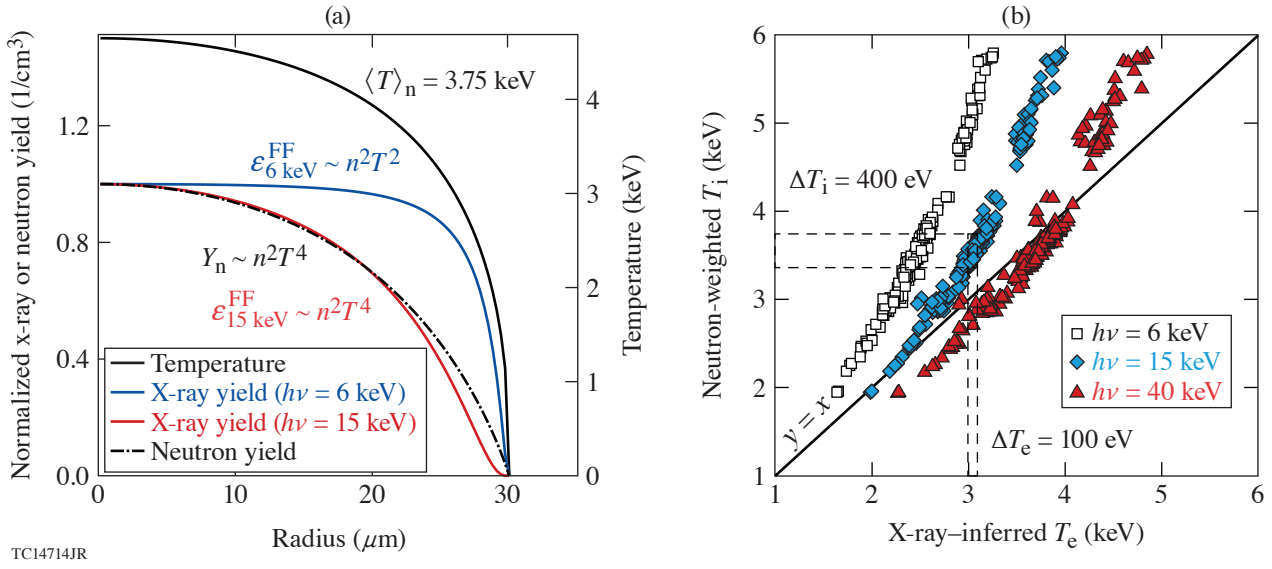

Figure 2
(a) Normalized x-ray and neutron yields comparison for a representative, isobaric hot-spot profile,[2] where $T_e = T_i$. At photon energy near 4× the neutron-weighted temperature, the emission approximately follows the neutron production. (b) The neutron-weighted ion temperature to the x-ray inferred electron temperature for all OMEGA DT cryogenic post-shot simulations in the simulation database.[4] The scatter in both plots suggests that direct surrogacy between the inferred electron temperature and the neutron-weighted ion temperature is not robust.

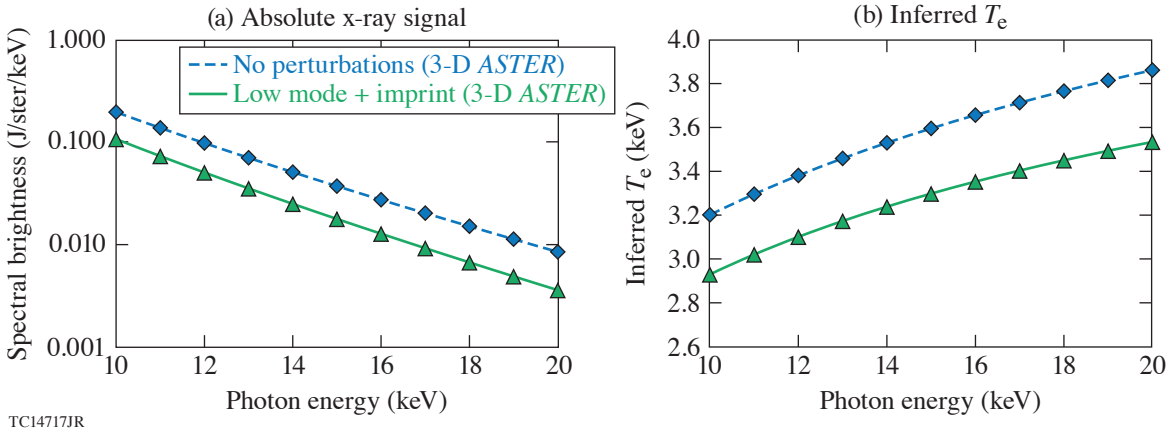

Figure 3
(a) Comparison of the electron temperature inferred from x-ray continuum emission as a function of photon energy between two *ASTER*[6] simulations with different levels of implosion perturbations. (b) Comparison of the x-ray emission as a function of photon energy for the same two *ASTER* simulations. The inferred electron temperature and the x-ray yield are not only sensitive to implosion degradation but are also sensitive enough to be measurable in experiments. The additional information these observables provide not only gives more opportunities for validating simulations, but also expands the capability of diagnosing fuel assembly during stagnation.

Between the 1-D and perturbed simulations, the neutron-weighted ion temperature dropped from 4.67 keV to 4.35 keV, and the neutron yield dropped from 4 to 2×10^{14}, a result stemming from decreased hot-spot compression. Similar to the neutron-weighted ion temperature, the electron temperature dropped by almost the same amount (~300 eV) throughout the 10- to 20-keV emission energy range. These changes being similar is not a coincidence; the 10- to 20-keV emission energy range is centered on the optimal energy range at which emission weighting is closest to neutron weighting. The drop being almost consistent across the entire range suggests the weighting is robust across a wide energy space. Most importantly, these changes in the electron temperature and absolute x-ray emission are larger than the expected detector uncertainty of ~5% and, therefore, expected to be observable. Measuring the electron temperature for a variety of cryogenic implosions on OMEGA should reveal trends more reliable than those depending on the neutron-weighted ion temperature. In addition, methods published by R. Epstein *et al.*[7] and T. Ma *et al.*[8] can be used for estimating hot-spot mix amounts with the absolute x-ray emission measurements. With the existence of a T_e measurement, the thermal-equilibrium assumption can also be removed and thereby improve the estimate's accuracy for implosions on OMEGA.

Interpretation and sensitivity analysis of the hot-spot electron temperature inferred from hard x rays have been performed. The electron temperature inferred from hard x-ray continuum emission was shown to be an emission-weighted, harmonic mean electron temperature. As this value varies with photon energy, it was shown both analytically and with simulations that the optimal photon energy for approximate neutron weighting is near 15 keV or more generally near 4× the neutron-weighted hot-spot temperature. Simulations also suggest, however, that one should not expect the hot-spot electron and ion temperatures to be equal in value for OMEGA-scale implosions caused by thermal nonequilibrium. For perturbed implosions, the deviation of the inferred electron temperature from 1-D is predicted to be sensitive to implosion performance. The drop in electron temperature is of the same order as the drop in the ion temperature, and the x-ray yield-over-clean ratio should similarly track the neutron yield-over-clean ratio. This sensitivity is expected to be significant enough to be observed in experiments and will be exploited for evaluating and optimizing future OMEGA DT cryogenic implosions.

This material is based upon work supported by the Department of Energy National Nuclear Security Administration under Award Number DE-NA0003856, the University of Rochester, and the New York State Energy Research and Development Authority.

1. J. J. MacFarlane *et al.*, High Energy Density Phys. **3**, 181 (2007).
2. R. Betti *et al.*, Phys. Plasmas **8**, 5257 (2001).
3. J. Delettrez *et al.*, Phys. Rev. A **36**, 3926 (1987).
4. V. Gopalaswamy *et al.*, Nature **565**, 581 (2019).
5. S. Atzeni and J. Meyer-ter-Vehn, *The Physics of Inertial Fusion: Beam Plasma Interaction, Hydrodynamics, Hot Dense Matter*, 1st ed., International Series of Monographs on Physics, Vol. 125 (Oxford University Press, Oxford, 2004).
6. I. V. Igumenshchev *et al.*, Phys. Plasmas **23**, 052702 (2016).
7. R. Epstein *et al.*, Phys. Plasmas **22**, 022707 (2015).
8. T. Ma *et al.*, Phys. Rev. Lett. **111**, 085004 (2013).

Fuel–Shell Interface Instability Growth Effects on the Performance of Room-Temperature Direct-Drive Implosions

S. C. Miller,[1,2] J. P. Knauer,[1] C. J. Forrest,[1] V. Yu. Glebov,[1] P. B. Radha,[1] and V. N. Goncharov[1,2]

[1]Laboratory for Laser Energetics, University of Rochester
[2]Department of Mechanical Engineering, University of Rochester

Performance degradation in direct-drive inertial confinement fusion implosions is caused by several effects, one of which is Rayleigh–Taylor (RT) instability growth during the deceleration phase. In room-temperature plastic target implosions, deceleration-phase RT growth is enhanced by the density discontinuity and finite Atwood number at the fuel–shell interface (see Fig. 1). The Atwood number $\left[A_T = \left(\rho_{shell} - \rho_{fuel}\right)/\left(\rho_{shell} + \rho_{fuel}\right)\right]$ of the interface is systematically varied by altering the ratio of deuterium to tritium (D:T) within the DT gas fill. The stability of the interface is best characterized by the effective Atwood number, which is primarily determined by radiation heating of the shell. Both simulation and experimental data show that yield performance scales with the fraction of D and T present in the fuel and that the observed inferred ion-temperature asymmetry $\left(\Delta T_i = T_i^{max} - T_i^{min}\right)$, which indicates the presence of long-wavelength modes, has a small sensitivity to the different D:T ratios. Three D:T ratios (10:90, 25:75, and 50:50) were chosen based on the material interface A_T to create *stable*, *neutrally stable*, and *unstable* conditions, respectively, during the deceleration phase.

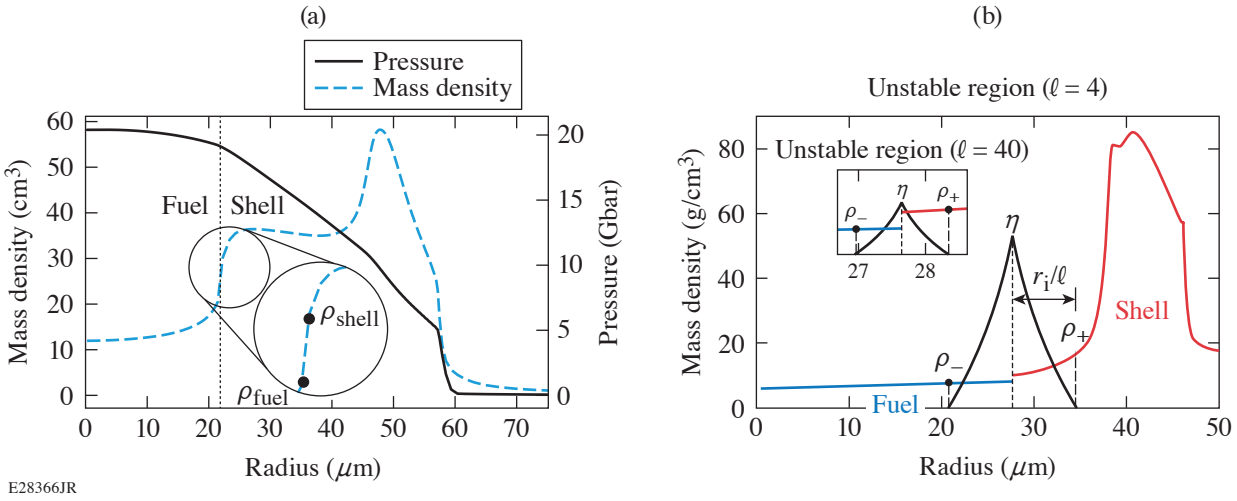

Figure 1
(a) The fuel–shell interface of room-temperature targets during the deceleration phase is classically unstable because of the jump in density. (b) Any ℓ-mode perturbations (η) present at the interface (r_i) will grow if $A_T > 0$. The size of the unstable region is proportional to the wavelength of the perturbation.

The fuel–shell interface Atwood number ($A_{T,i}$) is found to be *stable* for 10:90 ($A_{T,i} = -0.03$), *neutrally stable* for 25:75 ($A_{T,i} \approx 0.0$), and *unstable* for 50:50 ($A_{T,i} = 0.05$) using the ideal-gas equation of state and continuity conditions for pressure and temperature across the interface:

$$\frac{\rho_{\text{shell}}}{\rho_{\text{fuel}}} = \frac{m_{\text{i}}^{\text{shell}}}{m_{\text{i}}^{\text{fuel}}} \frac{1 + Z_{\text{fuel}}}{1 + Z_{\text{shell}}}.$$

Unstable modes present at the material interface grow during the deceleration phase of the implosion. Linear stability analysis of RT instability growth in semi-infinite density profiles has shown that these unstable modes are local to the interface, and that within the linear growth regime, the size of the unstable region is proportional to the perturbation wavelength.[1] The amplitude of the perturbation is highest on the interface itself and decays exponentially as the distance from the interface increases. In spherical geometry, the velocity perturbations decay as $\left(r_{\text{i}}/r\right)^{\ell+2}$ for $r > r_{\text{i}}$ and $(r/r_{\text{i}})^{\ell-1}$ for $r < r_{\text{i}}$, according to the radial distance (r) from the material interface (r_{i}) and mode number (ℓ). The effective Atwood number,[2] defined as $A_{\text{T}} = \left(\rho^{+} - \rho^{-}\right)/\left(\rho^{+} + \rho^{-}\right)$, uses the mass density averaged over the perturbation region $\left(\pm r_{\text{i}}/\ell\right)$ rather than the fuel and shell densities at the material interface (c.f., $A_{\text{T,i}}$). Figure 1(b) illustrates mass-density profiles with unstable regions for $\ell = 4$ and $\ell = 40$ perturbations. During the deceleration phase, these unstable regions are influenced by x-ray radiation that is released in the DT fuel of the hot spot. This x-ray radiation is absorbed into the colder CH shell, causing the material to heat up and expand inward, and results in a thicker shell with increased density and A_{T} near the material interface. This radiation preheat effect is present in both D:T 10:90 and 50:50 targets and causes their respective effective Atwood numbers to be comparable across a range of unstable modes.

Small-amplitude ($k\eta < 1$), single-mode perturbations grow exponentially in time, and since the Atwood number affects the exponential growth rates, 10:90 experiences significantly smaller growth factors (by a factor of ~5) compared to 50:50. As perturbation amplitudes become nonlinear ($k\eta > 1$), the growth changes from exponential to linear in time[2,3] and the difference in the growth factors between 10:90 and 50:50 becomes much smaller (only ~20%). Perturbations must grow to significant levels and become nonlinear in order for target performance to be affected. This explains why target performance should have small sensitivity to the Atwood number variations used in the experiment described below.

Multiple targets were fabricated to meet the design specification based on the classical material interface $A_{\text{T,i}}$. Each target was designed to be 860 μm in diameter with 27-μm-thick CH shells and a DT fuel fill pressure of 10 atm. Additional targets were created and opened up to measure the actual fuel D:T ratios after fabrication. Significant levels of protium (^{1}H) were found and were much higher than the initial D:T fill ratios. The yield-over-clean ratios $\left(Y_{\text{exp}}/Y_{\text{1-D}}\right)$, which used post-shot 1-D simulations that included the measured fuel levels, were consistent across all D:T ratios (see Fig. 2). This suggests that each shot experienced

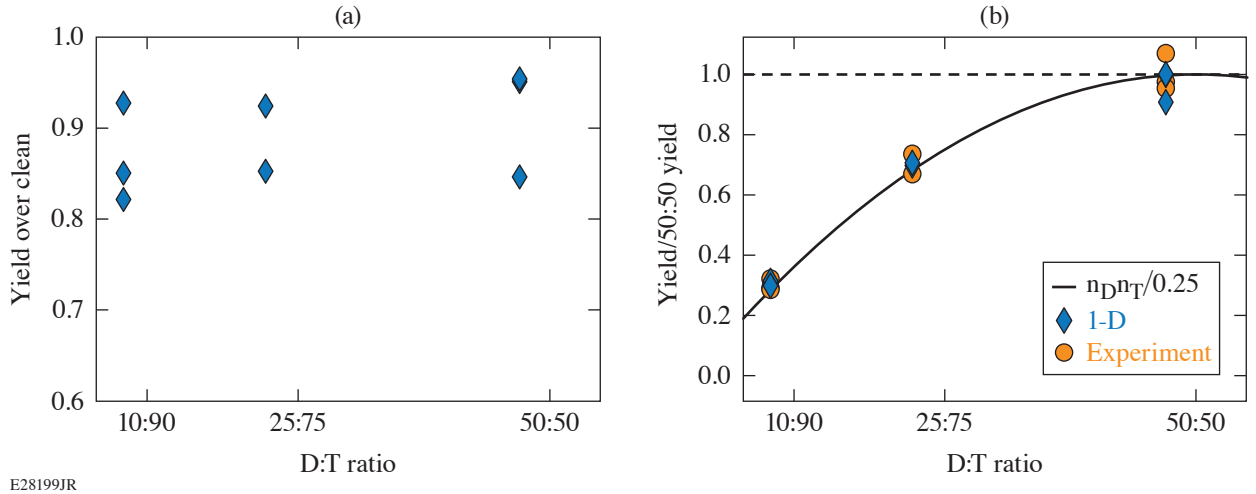

Figure 2
(a) Yield over clean $\left(Y_{\text{exp}}/Y_{\text{1-D}}\right)$ and (b) yield scaling. In (b), D:T 50:50 data points that lie above the dashed line at $y = 1.0$ indicate a higher than average yield. The solid black curve represents a simple yield scaling relation based on the DT number densities in the fuel.

the same level of asymmetry and instability growth. Additionally, the yield of each target, for both measured and simulated, scaled according to the fraction of deuterium and tritium in the fuel. Figure 2(b) illustrates the DT yield of each shot normalized to the respective (simulated or experimental) average 50:50 yield. Close clustering of the data points around the solid black curve indicates that the yield scaled according to the fuel composition.

Performance of the implosion is also assessed through inferred ion temperatures (T_i). These observations are taken from different lines of sight within the OMEGA target chamber. Ion temperature asymmetry $\left(\Delta T_i = T_i^{max} - T_i^{min}\right)$, currently taken from the set of six different neutron time-of-flight (nTOF) measurements, is used to identify significant differences in T_i caused by velocity broadening. Large ΔT_i indicates that there are significant nonradial components of velocity in the hot spot near peak neutron-production time, most likely caused by instability growth and highly directional flow variance. Figure 3 shows ΔT_i for each D:T ratio for both simulated and experimental results. Both simulated and experimentally inferred T_i indicate a comparable level of asymmetry across all D:T ratios. The experimental error bars (±100 eV) arise from the noise level in the detector signal, uncertainty in the numerical fit analysis,[4] and instrument response function of each detector.

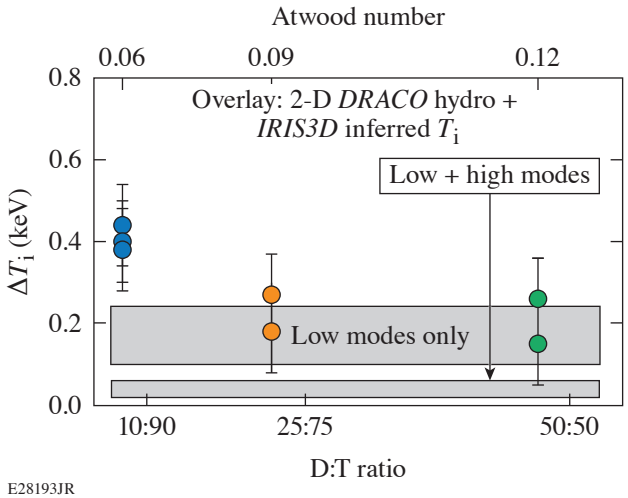

Figure 3
Inferred DT T_i asymmetry $\left(\Delta T_i = T_i^{max} - T_i^{min}\right)$, as a function of the D:T ratio and estimated Atwood number. The 2-D *DRACO* simulations provided the hydrodynamics and *IRIS3D*[5] provided the synthetic neutron diagnostics.

Simulations indicate that radiation preheat in all D:T ratios cause the interface to have comparable density profiles near the fuel–shell interface, and therefore similar A_T and instability growth factors. While 10:90 and 50:50 experience different linear instability growth factors for small-amplitude perturbations, nonlinear perturbations that impact target performance grow at comparable rates in either D:T configuration. In both experiments and simulations, the yield of all target configurations scales according to the composition of the fuel. Significant ΔT_i outside measurement uncertainty requires highly directional flow variance in order for detectors to observe differences from various lines of sight. Because both 10:90 and 50:50 had similar effective Atwood numbers, the simulated deceleration RT instability growth was nearly identical for nonlinear RT growth, and there was little influence on the inferred T_i and ΔT_i by altering the D:T ratio. Measurement uncertainty and noise levels make behavior trends inconclusive, and it is likely that the hot spot is relatively insensitive to changing the D:T ratio, as simulations suggest.

This material is based upon work supported by the Department of Energy National Nuclear Security Administration under Award Number DE-NA0003856, the University of Rochester, and the New York State Energy Research and Development Authority.

1. V. N. Goncharov, Phys. Rev. Lett. **88**, 134502 (2002).
2. V. N. Goncharov, "Self-Consistent Stability Analysis of Ablations Fronts in Inertial Confinement Fusion," Ph.D. thesis, University of Rochester, 1998.
3. U. Alon *et al.*, Phys. Rev. Lett. **74**, 534 (1995).
4. R. Hatarik *et al.*, J. Appl. Phys. **118**, 184502 (2015).
5. F. Weilacher, P. B. Radha, and C. J. Forrest, Phys. Plasmas **25**, 042704 (2018).

Simulated Refraction-Enhanced X-Ray Radiography of Laser-Driven Shocks

A. Kar, T. R. Boehly, P. B. Radha, D. H. Edgell, S. X. Hu, P. M. Nilson, A. Shvydky, W. Theobald, D. Cao, K. S. Anderson, V. N. Goncharov, and S. P. Regan

Laboratory for Laser Energetics, University of Rochester

X-ray radiography is a useful diagnostic in inertial confinement fusion (ICF) implosions to obtain shock positions by imaging shock waves. Specifically, it has been demonstrated that refraction-enhanced x-ray radiography[1] (REXR) can infer shock-wave positions of more than one shock wave, launched by a multiple-picket pulse in a planar plastic foil. REXR relies on the density gradient across a shock front that deflects x rays from their trajectory through refraction. It also accounts for the attenuation of the x rays as they travel through a denser medium with lower transmission by tracking their intensities. The benefit of this technique over existing x-ray postprocessors such as *Spect3D*[2] is that it includes x-ray refraction.

REXR is successful in overcoming some of the limitations of a velocity interferometer system for any reflector (VISAR) by locating shock waves before shocks merge and during the early time and the main drive of the laser pulse. VISAR does not provide any information about the shock wave early in time because of a time lag associated with the critical surface formation for the diagnostic to work. During the main drive, the high intensity of the laser leads to x-ray photoionization of the target ahead of the shock front. This blanks out the VISAR signal, preventing it from determining the shock wave's location.[3]

A point-projection radiography system was used to image a shock wave in a planar plastic foil on OMEGA [Fig. 1(a)]. The laser drive was comprised of a square pulse with ~350 J of energy that generated the shock wave in the foil. For the x-ray radiography, x rays of 5.2-keV energy corresponding to the He_α emissions of vanadium were projected from a 10-μm pinhole to image the shock wave onto an x-ray framing camera. The framing camera started to acquire the image at 8.63 ± 0.1 ns after the start of the laser pulse that generated the shock. The target was placed in the middle, 14 mm away from the pinhole and 533 mm away from the x-ray framing camera. This setup was simulated using the hydrodynamic code *DRACO* and the density profiles obtained from it were used to generate the simulated radiograph in Fig. 1(b). Figure 1(c) shows that the relative degree of transmission in the unshocked plastic, shocked plastic, and shocked aluminum with respect to the vacuum was in good agreement between the experiment and REXR. REXR showed that it is necessary to incorporate refraction and attenuation of x rays along with the appropriate opacity and refractive-index tables to interpret experimental images.

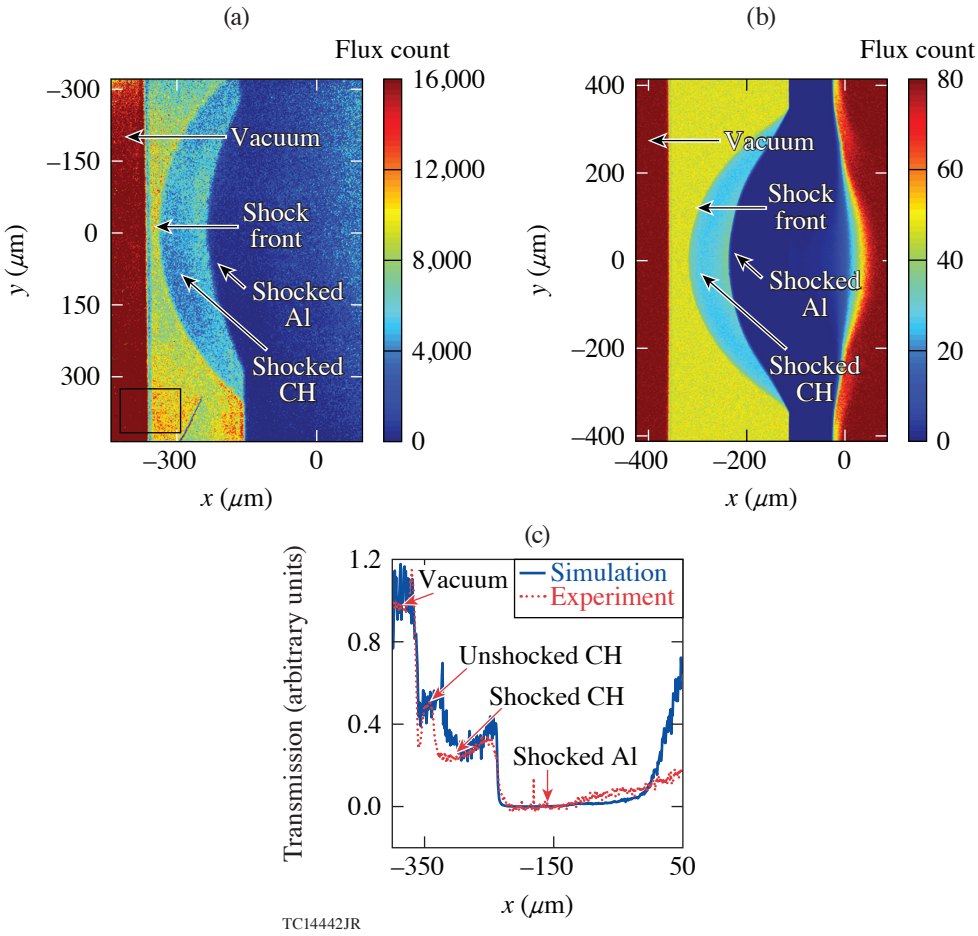

Figure 1
(a) Image obtained from an x-ray framing camera on OMEGA showing the bowing effect of the shock wave in plastic with the main features labeled. (b) Simulated radiograph for the same OMEGA experiment shows the shock profile in a plastic ablator. The x-ray flux is representative of the degree of transmission of the x rays through the different areas: vacuum (in red), unshocked plastic (in yellow), shocked plastic (in cyan), and shocked aluminum (in blue). (c) The transmission curves along the center of the beam axis obtained from the simulated radiograph and the experimental image showed good agreement between them for plastic and aluminum. For reference, the transmission in the vacuum region is set to 1 since there is no attenuation.

An experimental design to image multiple shock waves with REXR was proposed for the laser pulse in Fig. 2(a). Figure 2(b) shows the shock positions early in time and during main drive pulse that can be inferred from REXR when experimental diagnostics such as VISAR fail to locate the shock positions. REXR can be applied to design multiple-picket pulses with a better understanding of the shock locations. This will be beneficial to obtain the required adiabats for ICF implosions.

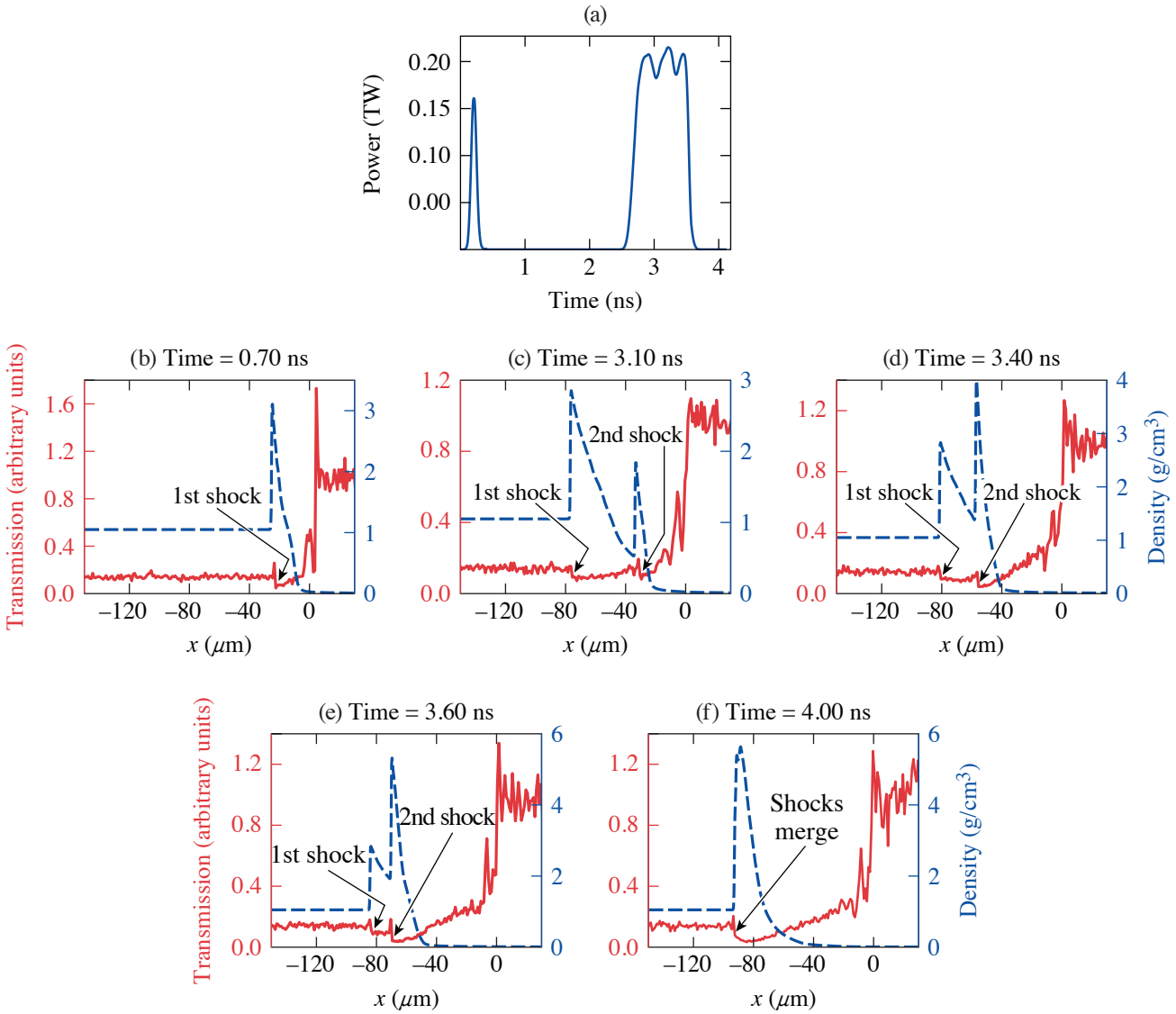

Figure 2

(a) A single-picket pulse with a main drive pulse of 190-J energy that launches two shock waves whose positions were inferred. [(b)–(f)] The transmission (red) and density profiles (blue) across the center of the beam axis obtained for the pulse shape in (a). The transmission has been scaled so that the intensity in the vacuum region is 1. The spikes followed by the dip (local minimum) in the transmission curve correspond to the shock fronts as labeled. The density profile also spikes at those points to illustrate this fact.

This material is based upon work supported by the Department of Energy National Nuclear Security Administration under Award Number DE-NA0003856, the University of Rochester, and the New York State Energy Research and Development Authority.

1. J. A. Koch *et al.*, J. Appl. Phys. **105**, 113112 (2009).

2. J. J. MacFarlane *et al.*, High Energy Density Phys. **3**, 181 (2007).; Prism Computational Sciences Inc., Madison, WI, Report PCS-R-041, Ver. 3.0 (2002).

3. T. R. Boehly *et al.*, Phys. Plasmas **13**, 056303 (2006).

Laser–Plasma Interactions Enabled by Emerging Technologies

J. P. Palastro,[1] F. Albert,[2] B. Albright,[3] T. Antonsen Jr.,[4] A. Arefiev,[5] J. W. Bates,[6] R. L. Berger,[2] J. Bromage,[1] E. M. Campbell,[1] T. Chapman,[2] E. Chowdhury,[7] A. Colaïtis,[8] C. Dorrer,[1] E. Esarey,[9] F. Fiúza,[10] N. Fisch,[11] R. K. Follett,[1] D. H. Froula,[1] S. H. Glenzer,[10] D. Gordon,[6] D. Haberberger,[1] B. M. Hegelich,[12,13] T. Jones,[6] D. Kaganovich,[6] K. Krushelnick,[14] P. Michel,[2] H. Milchberg,[4] J. Moloney,[15] W. Mori,[16] J. F. Myatt,[17] P. M. Nilson,[1] S. P. Obenschain,[6] J. L. Peebles,[1] J. Peñano,[6] M. Richardson,[18] H. G. Rinderknecht,[1] J. Rocca,[19] A. J. Schmitt,[6] C. Schroeder,[9] J. L. Shaw,[1] L. O. Silva,[20] D. Strozzi,[2] S. Suckewer,[11] A. Thomas,[14] F. Tsung,[16] D. Turnbull,[1] D. Umstadter,[21] J. Vieira,[20] J. Weaver,[6] M. S. Wei,[1] S. C. Wilks,[2] L. Willingale,[14] L. Yin,[3] and J. D. Zuegel[1]

[1]Laboratory for Laser Energetics, University of Rochester
[2]Lawrence Livermore National Laboratory
[3]Los Alamos National Laboratory
[4]University of Maryland, College Park
[5]University of California, San Diego
[6]Naval Research Laboratory
[7]Ohio State University
[8]Université de Bordeaux, Centre Lasers Intenses et Applications, France
[9]Lawrence Berkeley National Laboratory
[10]SLAC National Accelerator Laboratory
[11]Princeton University
[12]Gwangju Institute of Science and Technology, Center for Relativistic Laser Science
[13]University of Texas, Austin
[14]University of Michigan
[15]University of Arizona
[16]University of California, Los Angeles
[17]University of Alberta
[18]University of Central Florida
[19]Colorado State University
[20]Instituto Superior Técnico, Portugal
[21]University of Nebraska, Lincoln

Introduction

The recent awarding of the Nobel Prize to Donna Strickland, Ph.D., and Gerard Mourou, Ph.D., for chirped-pulse amplification (CPA) has highlighted the impact that broadband laser systems have had throughout science.[1] Plasma physics, in particular, has developed a unique synergy with CPA's: plasma has provided the only medium that can withstand the increases in intensity delivered by CPA's over the last 30 years. CPA is not, however, the only breakthrough in optics technology that has or promises to expand the frontier of laser–plasma interactions. Over the past ten years, creative optical solutions have produced unprecedented intensities, contrast, repetition rates, and gain bandwidths; renewed interest in long-wavelength drivers; and provided novel methods for spatiotemporal pulse shaping. Over the next ten years, these emerging technologies will advance diverse fields of plasma physics, including

- direct drive, indirect drive, and magnetized inertial confinement fusion
- nonperturbative nonlinear propagation and material interactions
- advanced accelerators
- plasma-based radiation sources
- ultrahigh-magnetic-field generation
- high-field and electron–positron plasmas
- structured light–plasma interactions

One such field—*plasma optics*—promises to overcome fundamental limitations of solid-state optical technology and will usher in the next frontier of plasma research. Progress and science discovery in pursuit of this frontier will require a community approach to experiments, simulations, and theory, together with investments in an ecosystem of laser facilities and simulation software.

Inertial Confinement Fusion

With the global population rising to over 9 billion by the end of the 21st century and the rising tide of climate change, the pursuit of environmentally acceptable energy sources has become more critical than ever. While still in the research stage, controlled fusion could deliver an almost endless supply of power with relatively low environmental impact. The inertial confinement fusion (ICF) approach, in particular, was one of the earliest applications to harness high-power lasers and has, on several occasions, implemented innovative optical techniques to effect step changes in performance: efficient frequency tripling, spatial coherence control (phase plates), induced spatial incoherence, and smoothing by spectral dispersion.[2–6] While these successes have allowed ICF to push the intensity ever higher, designs must still navigate around laser–plasma instabilities and laser imprint.[7,8] Laser–plasma instabilities inhibit the deposition of energy in the ablator and put the laser at risk for damage by scattering light into unwanted directions. Moreover, these instabilities can generate superthermal electrons that preheat the fusion fuel, reducing its compressibility. Laser imprint, i.e., density nonuniformities on the capsule surface imparted by speckles, seeds the Rayleigh–Taylor instability and can cause the capsule to break up during compression.

Creative uses of the bandwidth available on current laser systems may inhibit low-frequency laser–plasma instabilities like stimulated Brillouin scattering by detuning the interaction between multiple laser beams or by moving speckles before the instability can grow.[9] *Modern broad-bandwidth lasers, on the other hand, could revolutionize ICF by providing unprecedented spatiotemporal control over laser–plasma interactions.* These lasers can deliver pulses with the temporal incoherence necessary to suppress high-frequency instabilities like two-plasmon decay and stimulated Raman scattering, while also providing smoothing sufficient to eliminate imprint.[10–12] Generally speaking, the broad bandwidth mitigates laser–plasma instabilities by detuning the interaction between multiple waves or incoherently drives many small instabilities instead of a single coherent instability. To this end, optical parametric amplifiers (OPA's) offer an excellent candidate for the next-generation ICF driver. OPA's create high-power, broad-bandwidth light that can be seeded with a variety of temporal formats, including the random intensity fluctuations of parametric fluorescence, spike trains of uneven duration and delay, or chirplets.[13] The bandwidth of the resulting pulses, or those from an existing wideband architecture, could be further increased by stimulated rotational Raman scattering during propagation to the final focusing optics. Preliminary experiments have demonstrated that this technique can broaden the spectrum of frequency-multiplied Nd:glass and KrF pulses to multiterahertz bandwidths.[14]

Nonperturbative Nonlinear Propagation and Material Interactions

The field of nonperturbative nonlinear propagation and material interactions spans the boundary of nonlinear optics and plasma physics with relevant dynamics occurring over a trillion orders of magnitude in time: starting with the attosecond dynamics of bound electrons that determine the nonlinear optical response, evolving into the femto- and picosecond formation and evolution of plasma, and concluding with the micro- and millisecond hydrodynamic evolution of the neutral medium. *The emergence of high-power, high-repetition-rate (>kHz) ultrashort-pulse lasers enables novel regimes of nonlinear propagation and material interactions governed by a combination of nonthermal and thermal modifications to matter*—regimes with scientific, industrial, and security applications such as understanding new states of warm dense matter, femtosecond micromachining, laser eye surgery, electromagnetic pulse generation, and long-range propagation through atmosphere for remote sensing.

For a single high-power pulse propagating in transparent media, plasma formation counteracts the nonlinear collapse during self-focusing, leading to high-intensity propagation over distances much longer than a Rayleigh range.[15–18] At high repetition rates, each laser pulse experiences a nonlinear environment modified by its predecessors, which combines traditional effects such as thermal blooming[19] with ultrafast nonthermal effects, including ionization and impulsive (molecular) Raman excitation.[20] Already, experiments have demonstrated that a train of laser pulses can heat air through these processes, leaving behind a long-lasting neutral density channel that can guide subsequent laser pulses[21] and enhance the collection efficiency in remote detection.[22]

For high-repetition-rate material interactions, a laser pulse will interact with matter that has been strongly modified by the nonthermal heating of previous pulses. This heating can create periodic surface structures, change the reflectivity and absorption, or alter the molecular composition altogether. The interaction involves multiple physics phenomena, including the time-dependent dielectric response, stimulated scattering mechanisms, phase changes, electronic band-gap structure, and combined optical–collisional photoionization. In many of the solid and liquid media relevant to applications, the material properties governing these phenomena are not well characterized or even measured. Expanded use of spectral interferometry measurements,[23,24] as well as the pursuit of new techniques, could greatly improve understanding and facilitate the development of applications.

Plasma Accelerators

Particle accelerators provide a looking glass into a subatomic world inhabited by the fundamental building blocks of the universe. Conventional accelerators, based on vacuum technology, continue to make impressive strides, routinely improving beam quality and achieving unprecedented energies. With each advance, however, conventional accelerators grow in size or cost. Laser-plasma accelerators promise to break this trend by taking advantage of the extremely large fields either inherent to or driven by ultrashort laser pulses and a medium—plasma—that can sustain them. Armed with a vision of smaller-scale, cheaper accelerators and empowered by advances in laser technology, these "advanced accelerators" have achieved rapid breakthroughs in both electron and ion acceleration.

Early laser-wakefield acceleration (LWFA) experiments made steady progress by trapping and accelerating electrons in plasma waves excited by unmatched laser pulses—pulses with durations exceeding the plasma period.[25,26] Such pulses confined LWFA to suboptimal regimes in which plasma waves were driven either by laser pulse self-modulation or beat waves. With the advent of high-power, broadband multipass amplifiers, progress exploded—to this day, the maximum electron energy continues to climb with laser power.[27–30] These amplifiers deliver ultrashort pulses with durations less than the plasma period, allowing experiments to access the forced, quasi-linear, and bubble regimes.[31–33] Aside from increasing the maximum energy of the electron beams, the ultrashort pulses enable transformative injection techniques, through self-trapping or controlled ionization, that greatly reduced the electron beam emittance and energy spread.[34–36] *The emergence of amplifiers that can operate at both high peak and high average power provide a technological path toward a LWFA-based electron–positron collider.* While many physics and technology challenges must still be overcome, the high repetition rates of these systems could deliver the luminosity needed to achieve a number of events comparable to traditional colliders.[37]

While the large inertia of ions precludes their efficient acceleration through LWFA, a high-intensity pulse incident on a solid or shocked target can drive several mechanisms that accelerate ultrashort, high-flux ion beams from rest.[38–45] These mechanisms can be broadly separated into a few categories: ions accelerated by the sheath field of hot electrons escaping the back side of a solid target or target-normal sheath acceleration;[38,39] ions gaining energy by reflecting off a moving electrostatic potential, caused by either radiation pressure (hole boring)[40] or thermal pressure (shock acceleration);[41,42] beam-plasma modes excited during relativistic transparency;[43] solitary wave generation;[44] or hybrid schemes that combine elements of these with other mechanisms. Developments in high-power, broadband amplifiers have made sources based on these mechanisms widely accessible for a range of applications, producing ion beams with energies comparable to longer, higher-energy pulses. Proton sources, for instance, are now routinely used to radiograph high-energy-density matter, providing an invaluable probe for resolving plasma dynamics on picosecond time scales.[38,46] *Advances in laser contrast and amplifiers that operate at both high peak and high average power would represent a transformative step toward the realization of laser-driven proton/ion beams as injectors for high-brilliance accelerators and medical therapy.* When integrated with recent developments in high-repetition-rate cryogenic targets, high-

repetition-rate lasers offer significantly greater control over the acceleration process and enable high-quality beams with tens to hundreds MeV and high particle flux. This integration would also provide an ideal platform for understanding the origin and evolution of magnetic instabilities in proton beams.[45]

Radiation Sources

The strong accelerations experienced by electrons in intense laser–plasma interactions unleashes a torrent of secondary radiation that spans the electromagnetic spectrum. *Leveraging increases in laser repetition rate and intensity with creative interaction configurations and plasma structuring could spark the development of plasma-based radiation sources that excel in throughput, brightness, coherence, power, or efficiency.* These plasma-based sources offer compact, low-cost alternatives to sources based on conventional accelerators that, if harnessed, could be widely accessible for applications.

The development of sources in two frequency bands in particular, x-ray and terahertz (THz), would have far-reaching benefits in medicine, defense, and basic science.[47] Laser–plasma interactions generate x rays through a number of diverse mechanisms: betatron radiation from electrons oscillating in wakefields,[48,49] bremsstrahlung emission from energetic electrons crashing into high-density matter,[50] laser photons double Doppler-upshifted by a counter-traveling, relativistic electron beam, i.e., Compton scattering,[51,52] stimulated emission of photons from relativistic electrons wiggling in a free-electron laser,[53] x-ray lasing through transient collisional excitation,[54,55] or high harmonic generation from electrons accelerated in and out of a surface by an intense laser field.[56] This diversity provides the flexibility to choose a mechanism that best meets the requirements of applications such as phase-contrast imaging, radiosurgery, lithography, and nuclear resonance fluorescence for standoff detection of radioactive or other threatening materials. On the opposite end of the spectrum, the interaction of intense laser pulses with structured plasmas can efficiently drive THz radiation. The ponderomotive force of a laser pulse excites a time-dependent current. In a nonuniform plasma, this current radiates into the far field, emitting frequencies within a band determined by the pulse duration.[57,58] This radiation could bridge the "terahertz gap"—the scarcity of sources between the frequency ranges accessible by electronics and lasers—and do so with high-power, ultrashort THz pulses. In contrast to x rays, THz radiation is non-ionizing and can be safely used for noninvasive biomedical imaging and medical tomography. Further, the energy separation of rotational–vibrational eigenstates makes THz radiation ideal for time domain spectroscopy and standoff detection of chemical and biological molecules.[59,60] In terms of discovery science, THz radiation can directly excite matter to highly excited phonon states, unlocking new regimes of high-energy-density physics.[61]

Magnetized Plasmas

Like plasmas, magnetic fields occur ubiquitously throughout the universe and play a critical role in shaping astrophysical environments. Emulating these environments in the laboratory with well-diagnosed experiments can provide a valuable complement to conventional astrophysical observations. High-power lasers facilitate these experiments by creating scale-equivalent plasma conditions with self-generated or external magnetic fields, or by directly driving up magnetic fields through laser–plasma interactions. Either way, the magnetic fields fundamentally alter the laser–plasma interaction. The presence of ultrastrong, quasi-static magnetic fields modifies the microscopic kinetics by diverting, confining, or undulating electrons; the collective behavior by bringing the cyclotron resonance within reach of optical excitation; and laser propagation through peculiar dispersive effects such as polarization rotation, slow light, and induced transparency.

The capability to perform controlled, focused experiments by generating strong magnetic fields with lasers has only recently emerged. The current approach, based on existing laser technology, uses a long, high-energy pulse to drive a current through induction coils. Aside from basic laboratory astrophysics, these platforms allow one to investigate magnetized high-energy-density physics related to the transport of high-energy particles and high-gain ICF schemes like fast ignition.[62] *The projected intensities delivered by next-generation laser systems could directly drive volumetric magnetic fields rivaling those occurring on the surface of neutron stars (~MT).* These extreme fields, created by the highly nonlinear currents driven by an intense laser pulse propagating through a relativistically transparent, high-density plasma, would result in a number of immediate breakthroughs:[63–65] they would significantly enhance the transfer of energy from a laser pulse to electrons and facilitate the emission of gamma rays from relativistic electrons by providing a powerful undulator.[64,66] The development of such a gamma-ray source would be critical for the development of nuclear and radiological detection systems. Furthermore, the gamma-ray source would enable discover-

ies linked to our understanding of the early universe and high-energy astrophysics, including the direct creation of matter and antimatter from light[67] and allow the direct control and study of nuclear excitation and structure.[68]

High Field and Electron–Positron Plasmas

Nonperturbative quantum electrodynamics (QED) represents the current frontier of laser–plasma interactions—a frontier in which ripping electron–positron pairs from the Dirac sea may make targets a thing of the past[69]—a frontier in which vacuum exhibits magnetization, polarization and birefringence[67]—a frontier in which the analogy of Hawking radiation in electric fields, Unruh radiation, could provide insight into the life-cycle of black holes.[70] Compared to any other physical theory, perturbative QED predictions have been experimentally confirmed to unprecedented accuracy. While electric fields strong enough to accelerate an electron to its rest mass over a Compton wavelength, i.e., at the Schwinger limit, are sufficient to test nonperturbative QED models, creative laser-plasma configurations can create highly nonlinear environments at much lower field strengths. This strategy has already proven successful in experimental demonstrations of nonlinear Compton scattering,[71] positron production,[72,73] and radiation reaction.[74] Nevertheless, the exotic theoretical and computational predictions of nonperturbative QED models have rapidly outpaced the experimental capabilities to test them. *By providing flexible laser-plasma configurations and extremely high intensities, a next-generation laser could access unexplored regimes of nonperturbative, collective QED effects in plasmas and test the exotic predictions of the models.* Such a facility could bring the mysteries of astrophysical objects, including black holes, pulsars, and magnetars, down to earth and uncover the dynamic interaction of inner shell electrons with highly ionized, heavy nuclei.[75,76]

Structured Light–Plasma Interactions

Beyond simply adjusting parameters like intensity and frequency, the spatiotemporal structure of light offers additional degrees of freedom for controlling the interaction of intense laser pulses with plasma. Structured light fields emerge spontaneously when two or more electromagnetic plane waves interfere. The interference of three waves, for instance, can produce phase singularities, which give rise to one of the most fascinating features of structured light—orbital angular momentum (OAM). OAM pulses can impart angular momentum to the plasma, modifying the topology and dispersion of driven waves and the phase space of the charged particles they accelerate.[77,78] As an example, a laser pulse with a helical intensity profile, or "light spring," can ponderomotively excite a wakefield that traps and accelerates a vortex electron beam, i.e., a beam that rotates around the optical axis.[78] OAM can also modify the nonlinear propagation and interaction of high-power pulses with transparent media, resulting in helical plasma filaments or high harmonic radiation with vortex phase structure.[79,80]

More-complex interference patterns exhibit striking properties that appear to violate special relativity: the peak intensity of a self-accelerating light beam follows a curved trajectory in space,[81] while the peak intensity of a "flying focus" pulse can travel at an arbitrary velocity, surpassing even the vacuum speed of light.[82] These arbitrary velocity intensity peaks result from the chromatic focusing of a chirped laser pulse. The chromatic aberration and chirp determine the location and time at which each frequency component within the pulse comes to focus, i.e., reaches its peak intensity, respectively. By adjusting the chirp, the velocity of the intensity peak can be tuned to any value, either co- or counter-propagating along the laser axis. This, in turn, grants control over the velocity of an ionization front or ponderomotive force—a control with the potential to advance several plasma-based applications, including Raman amplification, photon acceleration, wakefield acceleration, and THz generation.[83,84] While these unexpected features of structured light bring about new and rich laser–plasma interactions, they have remained relatively unexplored because of the technological challenges of creating such pulses. *The further development of ultrafast pulse-shaping techniques to manipulate the spatiotemporal degrees of freedom would provide a virtual forge for creating pulses to optimize or bring about novel laser–plasma interactions.* In doing so, these techniques would enrich all of the subfields discussed above.

Plasma Optics

Ultimately, advances in plasma physics will require repetition rates or intensities that exceed the damage limitations of solid-state optical components. Even with improvements in high-damage optical coatings, the size of solid-state optical components must increase to maintain tolerable fluences. Aside from the prohibitive cost of such large optics, this approach will eventually become counteractive: larger optics can withstand higher powers, but their fabrication introduces surface aberrations that reduce focusability and, as a result, the peak intensity. *Plasma-based optical components could provide the disruptive technology*

needed to usher in the next frontier of plasma research. Plasma optics, being already ionized, have substantially higher damage thresholds than solid-state components and can be inexpensively and rapidly replaced, for instance, at the repetition rate of a gas jet or capillary or the flow rate of a water jet.[85–89]

Similar to conventional optics, a laser pulse propagating in plasma acquires a spatiotemporal phase determined by the refractive index. By controlling the spatial variation, evolution, or nonlinearity of the plasma density, the plasma can provide dispersion, refraction, or frequency conversion, respectively, and, in principle, be made to mimic any solid-state optical component. Already, several such components routinely improve experimental performance: plasma gratings successfully tune the implosion symmetry of ICF capsules at the National Ignition Facility;[90] plasma waveguides combat diffraction, extending the interaction length in LWFA's;[91] and plasma mirrors (1) enhance intensity contrast by orders of magnitude, allowing for impulsive laser–matter interactions free of premature heating[92] and (2) redirect laser pulses in multistage LWFA's without degrading electron-beam emittance.[93] Several other plasma components, while still in the nascent stages of development, have been successfully demonstrated in experiments: lenses,[94,95] wave plates,[96] q-plates,[97] beam combiners,[98] compressors, and amplifiers.[99] Plasma amplifiers, in particular, could eventually replace CPA's in the final power-amplification stage of a laser, eliminating the need for large, expensive gratings.[100] In principle, these amplifiers can achieve intensities $10^3\times$ larger than CPA's in the infrared or operate in wavelength regimes inaccessible to CPA's altogether, e.g., the ultraviolet or x-ray range.[101] A next-generation high-power laser that implemented plasma components could deliver extremely high intensity pulses—pulses that would transform the landscape of laser–plasma interactions.

This material is based upon work supported by the Department of Energy National Nuclear Security Administration under Award Number DE-NA0003856, the University of Rochester, and the New York State Energy Research and Development Authority.

1. D. Strickland and G. Mourou, Opt. Commun. **55**, 447 (1985).
2. R. S. Craxton, IEEE J. Quantum Electron. **QE-17**, 1771 (1981).
3. J. Nuckolls *et al*., Nature **239**, 139 (1972).
4. Y. Kato and K. Mima, Appl. Phys. B **29**, 186 (1982).
5. R. H. Lehmberg, A. J. Schmitt, and S. E. Bodner, J. Appl. Phys. **62**, 2680 (1987).
6. S. Skupsky *et al*., J. Appl. Phys. **66**, 3456 (1989).
7. W. L. Kruer, *The Physics of Laser Plasma Interactions*, Frontiers in Physics, Vol. 73, edited by D. Pines (Addison-Wesley, Redwood City, CA, 1988).
8. S. E. Bodner, Phys. Rev. Lett. **33**, 761 (1974).
9. L. Divol, Phys. Rev. Lett. **99**, 155003 (2007).
10. J. W. Bates *et al*., Phys. Rev. E **97**, 061202 (2018).
11. R. K. Follett *et al*., Phys. Rev. Lett. **120**, 135005 (2018).
12. J. P. Palastro *et al*., Phys. Plasma **25**, 123104 (2018).
13. G. Cerullo and S. De Silvestri, Rev. Sci. Instrum. **74**, 1 (2003).
14. J. Weaver *et al*., Appl. Opt. **56**, 8618 (2017).
15. A. Couairon and A. Mysyrowicz, Phys. Rep. **441**, 47 (2007).
16. H. M. Milchberg *et al*., Phys. Plasma **21**, 100901 (2014).
17. P. Panagiotopoulos *et al*., Nat. Photonics **9**, 543 (2015).
18. S. Tochitsky *et al*., Nat. Photonics **13**, 41 (2019).

19. K. A. Brueckner and S. Jorna, Phys. Rev. **164**, 182 (1967).
20. J. P. Palastro, T. M. Antonsen, and H. M. Milchberg, Phys. Rev. A **86**, 033834 (2012); **90**, 069902(E) (2014).
21. N. Jhajj *et al*., Phys. Rev. X **4**, 011027 (2014).
22. E. W. Rosenthal *et al*., Optica **1**, 5 (2014).
23. Z. W. Wilkes *et al*., Appl. Phys. Lett. **94**, 211102 (2009).
24. T. Winkler *et al*., Appl. Surf. Sci. **374**, 235 (2016).
25. A. Modena *et al*., Nature **377**, 606 (1995).
26. E. Esarey, C. B. Schroeder, and W. P. Leemans, Rev. Mod. Phys. **81**, 1229 (2009).
27. T. Katsouleas, Nature **431**, 515 (2004).
28. X. Wang *et al*., Nat. Commun. **4**, 1988 (2012).
29. H. T. Kim *et al*., Phys. Rev. Lett. **111**, 165002 (2013).
30. W. P. Leemans *et al*., Phys. Rev. Lett. **113**, 245002 (2014).
31. V. Malka *et al*., Science **298**, 1596 (2002).
32. W. Lu *et al*., Phys. Rev. Lett. **96**, 165002 (2006).
33. W. Lu *et al*., Phys. Rev. ST Accel. Beams **10**, 061301 (2007).
34. D. H. Froula *et al*., Phys. Rev. Lett. **103**, 215006 (2009).
35. A. Pak *et al*., Phys. Rev. Lett. **104**, 025003 (2010).
36. C. McGuffey *et al*., Phys. Rev. Lett. **104**, 025004 (2010).
37. C. B. Schroeder *et al*., AIP Conf. Proc. **1086**, 208 (2009).
38. M. Roth *et al*., Phys. Rev. Spec. Top., Accel. Beams **5**, 061301 (2002).
39. L. Willingale *et al*., Phys. Rev. Lett. **96**, 245002 (2006).
40. A. Henig *et al*., Phys. Rev. Lett. **103**, 245003 (2009).
41. D. Haberberger *et al*., Nat. Phys. **8**, 95 (2012).
42. F. Fiuza *et al*., Phys. Rev. Lett. **109**, 215001 (2012).
43. L. Yin *et al*., Phys. Plasma **18**, 063103 (2011).
44. D. Jung *et al*., Phys. Rev. Lett. **107**, 115002 (2011).
45. S. Göde *et al*., Phys. Rev. Lett. **118**, 194801 (2017).
46. L. Willingale *et al*., Phys. Plasmas **17**, 043104 (2010).
47. F. Albert and A. G. R. Thomas, Plasma Phys. Control. Fusion **58**, 103001 (2016).
48. F. Albert *et al*., Phys. Rev. Lett. **111**, 235004 (2013).
49. J. P. Palastro, D. Kaganovich, and D. Gordon, Phys. Plasma **22**, 063111 (2015).
50. N. Lemos *et al*., Plasma Phys. Control. Fusion **60**, 054008 (2018).

51. S. Chen *et al*., Phys. Rev. Lett. **110**, 155003 (2013).
52. N. D. Powers *et al*., Nat. Photonics **8**, 28 (2014).
53. A. R. Maier *et al*., Phys. Rev. X **2**, 031019 (2012).
54. B. R. Benware *et al*., Phys. Rev. Lett. **81**, 5804 (1998).
55. Y. Wang *et al*., Nat. Photonics **2**, 94 (2008).
57. J. M. Mikhailova *et al*., Phys. Rev. Lett. **109**, 245005 (2012).
57. C. Miao, J. P. Palastro, and T. M. Antonsen, Phys. Plasma **23**, 063103 (2016).
58. C. Miao, J. P. Palastro, and T. M. Antonsen, Phys. Plasma **24**, 043109 (2017).
59. J. F. Federici *et al*., Semicond. Sci. Technol. **20**, S266 (2005).
60. H. Liu *et al*., Proc. IEEE **95**, 1514 (2007).
61. M. Kozina *et al*., Nat. Phys. **15**, 387 (2019).
62. G. Fiksel *et al*., Rev. Sci. Instrum. **86**, 016105 (2015).
63. J. Peebles *et al*., Phys. Rev. E **98**, 053202 (2018).
64. O. Jansen *et al*., Plasma Phys. Control. Fusion **60**, 054006 (2018).
65. T. Wang *et al*., Phys. Plasma **26**, 013105 (2019).
66. D. J. Stark, T. Toncian, and A. V. Arefiev, Phys. Rev. Lett. **116**, 185003 (2016).
67. M. Marklund and P. K. Shukla, Rev. Mod. Phys. **78**, 591 (2006).
68. D. Habs *et al*., Eur. Phys. J. D **55**, 279 (2009).
69. N. B. Narozhny and A. M. Fedotov, Eur. Phys. J. Spec. Top. **223**, 1083 (2014).
70. P. Chen and G. Mourou, Phys. Rev. Lett. **118**, 045001 (2017).
71. C. Bula *et al*., Phys. Rev. Lett. **76**, 3116 (1996).
72. H. Chen *et al*., Phys. Rev. Lett. **102**, 105001 (2009).
73. G. Sarri *et al*., Nat. Commun. **6**, 6747 (2015).
74. J. M. Cole *et al*., Phys. Rev. X **8**, 011020 (2018).
75. G. Brodin *et al*., Phys. Rev. Lett. **98**, 125001 (2007).
76. B. Hafizi, D. F Gordon, and J. P Palastro, Phys. Rev. Lett. **118**, 133201 (2017).
77. J. Vieira *et al*., Nat. Commun. **7**, 10371 (2016).
78. J. Vieira, J. T Mendonça, and F. Quéré, Phys. Rev. Lett. **121**, 054801 (2018).
79. N. Barbieri *et al*., Appl. Phys. Lett. **104**, 261109 (2014).
80. F. Sanson *et al*., Opt. Lett. **43**, 2780 (2018).
81. G. A. Siviloglou *et al*., Phys. Rev. Lett. **99**, 213901 (2007).
82. D. H. Froula *et al*., Nat. Photonics **12**, 262 (2018).

83. J. P. Palastro *et al*., Phys. Rev. A **97**, 033835 (2018).
84. D. Turnbull *et al*., Phys. Rev. Lett. **120**, 024801 (2018).
85. H. Sheng *et al*., Phys. Rev. E **72**, 036411 (2005).
86. D. Kaganovich *et al*., Phys. Rev. E **59**, R4769 (1999).
87. D. Panasenko *et al*., J. Appl. Phys. **108**, 044913 (2010).
88. D. F. Gordon *et al*., Phys. Plasmas **25**, 063101 (2018).
89. D. Kaganovich *et al*., Appl. Opt. **57**, 9392 (2018); **58**, 368(E) (2019).
90. P. Michel *et al*., Phys. Plasmas **17**, 056305 (2010).
91. C. G. Durfee and H. M. Milchberg, Phys. Rev. Lett. **71**, 2409 (1993).
92. A. Lévy *et al*., Opt. Lett. **32**, 310 (2007).
93. S. Steinke *et al*., Nature **530**, 190 (2016).
94. Y. Katzir *et al*., Appl. Phys. Lett. **95**, 031101 (2009).
95. J. P. Palastro *et al*., Phys. Plasmas **22**, 123101 (2015).
96. D. Turnbull *et al*., Phys. Rev. Lett. **116**, 205001 (2016).
97. K. Qu, Q. Jia, and N. J. Fisch, Phys. Rev. E **96**, 053207 (2017).
98. R. K. Kirkwood *et al*., Nat. Phys. **14**, 80 (2018).
99. Y. Ping *et al*., Phys. Rev. E **62**, R4532 (2000).
100. V. M. Malkin, G. Shvets, and N. J. Fisch, Phys. Rev. Lett. **82**, 4448 (1999).
101. V. M. Malkin, N. J. Fisch, and J. S. Wurtele, Phys. Rev. E **75**, 026404 (2007).

A Modified Technique for Laser-Driven Magnetic Reconnection

P. M. Nilson,[1] W. Fox,[2,3] J. Matteucci,[3] and D. H. Froula[1,4]

[1]Laboratory for Laser Energetics, University of Rochester
[2]Princeton Plasma Physics Laboratory
[3]Department of Astrophysical Sciences, Princeton University
[4]Department of Physics & Astronomy, University of Rochester

For over a decade, numerous experimental and computational studies have investigated magnetic reconnection in high-energy-density plasmas.[1–3] An improved understanding of the reconnection theory and its application to extreme astrophysical environments and controlled fusion motivates these studies. One method for driving reconnection uses the collision between two laser-produced plasmas at the surface of a solid target. As the plasmas expand, the oppositely oriented Biermann fields are forced together and reconnect. In all previous studies, the plasmas were generated up to several laser-spot diameters apart, allowing time for the plasmas to expand and the Biermann fields to grow before colliding and forcing reconnection at their outermost edges.

In this work, a modified technique for driving reconnection is proposed and demonstrated. Two high-energy laser pulses were focused to 2×10^{14} W/cm^2 and pointed one laser-spot diameter apart on the surface of a thick plastic foil. The closer spot separation minimizes the time for plasma expansion before the interaction occurs and allows the largest magnetic fields at the edge of each laser spot to interact and reconnect. Proton radiography was used to demonstrate the technique by mapping the changes in magnetic connectivity at the target surface. The data show where the magnetic fields are located, where they are transported to, how they merge and reconnect, and where they reside post reconnection.

Figure 1 shows the experimental setup carried out on the OMEGA EP Laser System. Two long-pulse beams with a 351-nm wavelength were focused on the surface of a 5×5-mm^2, 50-μm-thick plastic foil. Each beam delivered 2 kJ of energy in a 2.5-ns square pulse focused to an 820-μm-diam focal spot. The laser intensity was 2×10^{14} W/cm^2 and each laser beam included distributed phase plates. The main target interaction was probed with an ultrafast proton beam. The protons were accelerated from a 20-μm-thick Cu foil mounted inside a plastic tube facing the main target. The Cu foil was irradiated at normal incidence with

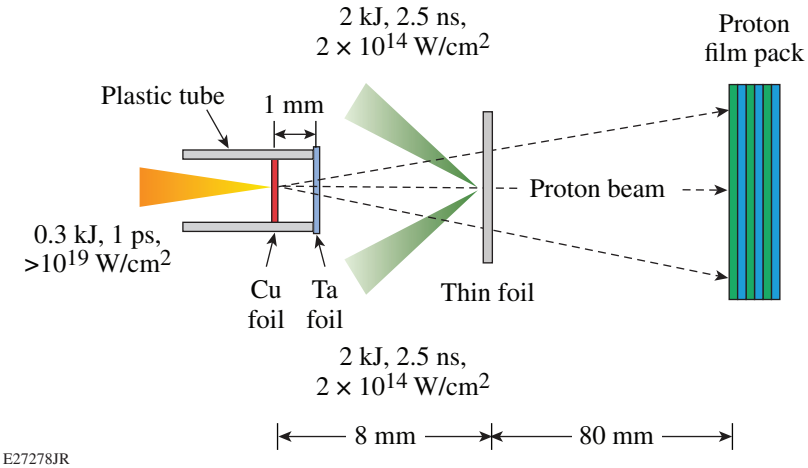

Figure 1
Experimental setup.

a 0.3-kJ, 1-ps pulse of 1.053-μm light at focused intensities above 10^{19} W/cm^2. A proton beam with energies up to several tens of MeV was accelerated by target normal sheath acceleration. To protect the rear surface of the Cu foil from the coronal plasma and x-ray preheat generated by the long-pulse interaction, a 5-μm-thick Ta foil was used to cap the end of the plastic tube. A filtered radiochromic film detector stack was used to measure the proton beam after it traversed the main target interaction.

Figure 2 shows proton radiographs of a series of two-beam interactions with a laser-spot separation of one focal-spot diameter (~820 μm). The laser pulses were co-timed. Data are shown at eight different times between $t = t_0 + 0.17$ ns and $t = t_0 + 1.97$ ns. Each time interval was measured on a different shot. The images were generated with 29-MeV protons. At $t = t_0 + 0.17$ ns [Fig. 2(a)], the radiograph shows a pair of dark rings consistent with two distinct Biermann fields at the edge of each laser focal region.[4] These dark rings remain continuous and physically separate at $t = t_0 + 0.27$ ns [Fig. 2(b)]. The plasmas have begun to merge at $t = t_0 + 0.37$ ns [Fig. 2(c)], and the detected proton flux at the intersection point is diminished. Over the next 800 ps, the inner dark rings progressively transform into a continuous oval-like pattern [Figs. 2(c)–2(f)]. This changing pattern is consistent with a transition from two isolated Biermann fields into a single global magnetic field that surrounds the laser focal regions. Post reconnection, the change in magnetic connectivity is sustained and the dark oval pattern is measured at $t = t_0$+ 1.47 ns [Fig. 2(g)] and $t = t_0 + 1.97$ ns [Fig. 2(h)].

The work described here uses a simple but crucial modification to the conventional laser-driven reconnection geometry that has significant physical implications. Compared to the original laser-driven reconnection technique, the geometry modifies where, when, and how magnetic reconnection occurs. The interaction between the neighboring plumes occurs earlier in time, the distance the largest magnetic fields must be transported before the reconnection layer forms is reduced, and the driven-reconnection process is less perturbed by plasma accumulation at the midplane. Most notably, the geometry allows for field-line reconnection

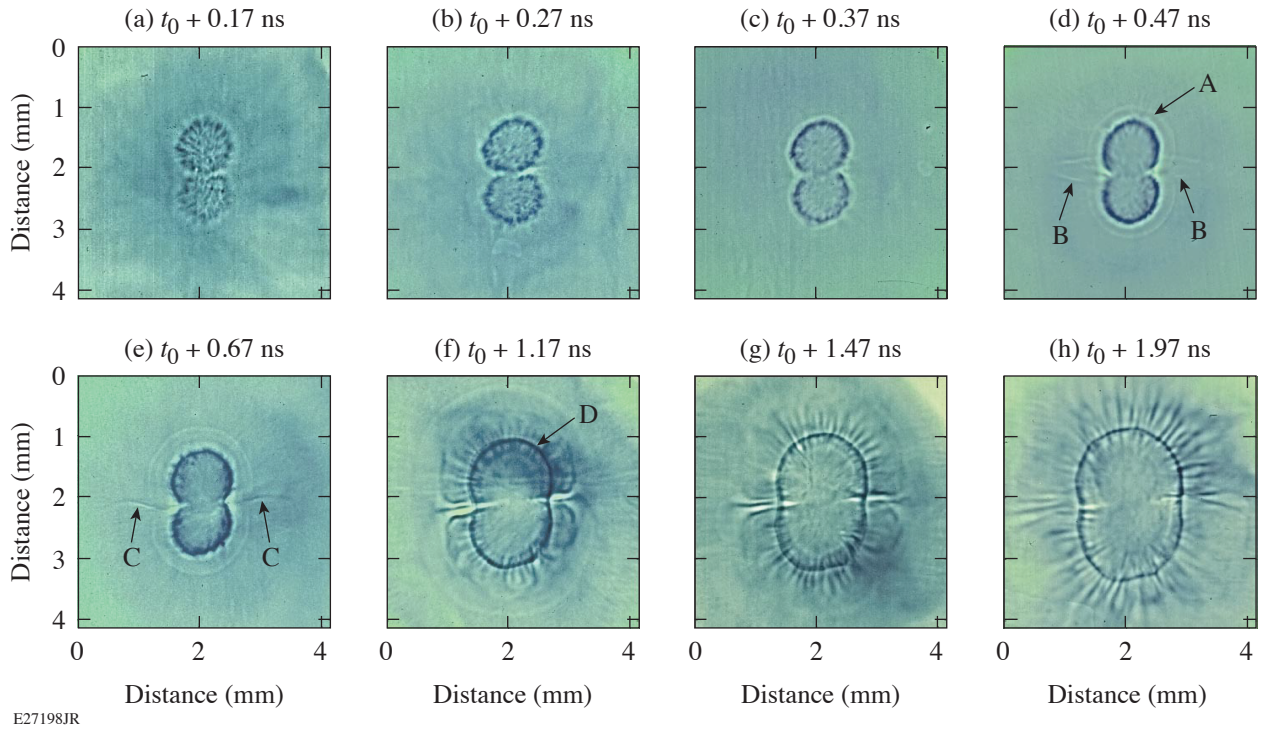

Figure 2
Proton radiographs of two-beam interactions with 50-μm-thick plastic foils taken at eight different times. Diagnostic signatures of the plasma–vacuum boundary (A), outflowing plasma (B and C), and magnetic fields (D) close to the laser focal regions are highlighted.

of the largest-magnitude magnetic fields that are generated at the edge of each laser spot, unhindered by stagnating plasma flows. It is important to note that no previous studies have identified this possibility or attempted to drive reconnection at such close laser-spot separation.

This material is based upon work supported by the Department of Energy National Nuclear Security Administration under Award Number DE-NA0003856, the University of Rochester, and the New York State Energy Research and Development Authority.

1. P. M. Nilson *et al*., Phys. Rev. Lett. **97**, 255001 (2006).
2. C. K. Li *et al*., Phys. Rev. Lett. **99**, 055001 (2007).
3. W. Fox, A. Bhattacharjee, and K. Germaschewski, Phys. Rev. Lett. **106**, 215003 (2011).
4. L. Gao *et al*., Phys. Rev. Lett. **114**, 215003 (2015).

Mitigation of Self-Focusing in Thomson-Scattering Experiments

A. M. Hansen, D. Turnbull, J. Katz, and D. H. Froula

Laboratory for Laser Energetics, University of Rochester

Accurately diagnosing plasma conditions is vital to the success of a wide variety of high-energy-density physics experiments. Optical Thomson scattering from collective ion-acoustic and electron wave features offers a method of measuring plasma parameters with spatial and temporal resolution. Analysis of Thomson-scattered spectra reveals an abundance of useful data including electron density, electron temperature, ion temperature, ionization state, ion species composition, bulk flow velocity, and heat flux.

A challenge associated with Thomson-scattering measurements arises from the small scattering cross section. To overcome this challenge, a high-energy probe laser beam is required to measure single-shot Thomson-scattering spectra with acceptable signal-to-noise ratio (SNR), but in order for the laser beam to propagate through the plasma, its power must remain below the self-focusing threshold,

$$P_c\left(W\right) = 3 \times 10^7 \frac{T_e\left(\text{keV}\right)}{n_e/n_c}, \tag{1}$$

where T_e is the electron temperature and n_e/n_c is the electron density normalized to the critical plasma density for the wavelength of the Thomson-scattering laser.

Figure 1 shows the limitations of the Thomson-scattering SNR introduced by limiting the incident probe laser power to the threshold for self-focusing. The region below the curves has a reduced SNR because of the lower-than-optimum incident laser power. Increasing the laser power to raise the SNR above the curves results in self-focusing. The small SNR demonstrates the challenges

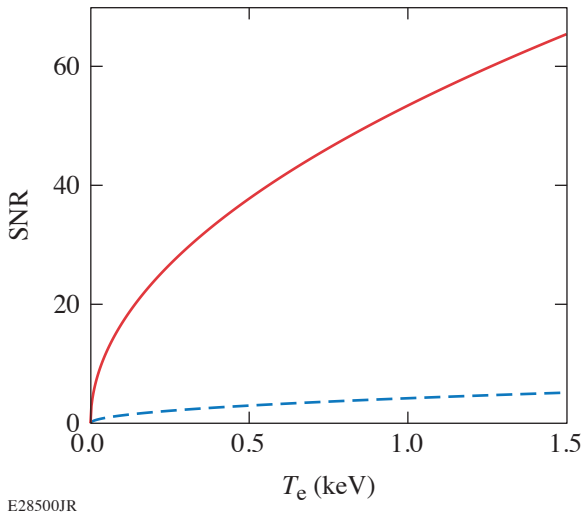

Figure 1
The curves represent the maximum measurable signal-to-noise ratio achievable in a Thomson-scattering experiment as a function of electron temperature assuming a Thomson-scattering probe beam with a power equal to the critical power for self-focusing for a beam with (dashed) and without (solid) a phase plate.

of obtaining high-fidelity Thomson-scattering spectra. The SNR can be improved by a factor of 10 by using a distributed phase plate (DPP). A DPP increases the filamentation threshold by distributing the laser's power across many lower power speckles.

Two-dimensional Thomson-scattering measurements (Fig. 2) show the limits of probe-beam propagation that are consistent with the limitations of self-focusing [Eq. (1)]. For experiments above the self-focusing threshold [Fig. 2(a)], the Thomson-scattering beam was observed to self-focus and no Thomson-scattering signals were observed from the Thomson-scattering volume located at the center (0, 0). By introducing a phase plate to the Thomson-scattering beam [Fig. 2(c)], excellent laser beam propagation was observed along with high-SNR Thomson-scattering spectra. The electron plasma and ion-acoustic wave features were measured, and these spectra were used to determine the electron density, temperature, and flow velocity as a function of time and space in a gas-jet plasma heated by a total of 1.8 kJ of laser energy on the OMEGA laser. The results show very uniform 1.5-mm density and temperature plateaus, which are ideally suited for future laser–plasma interaction experiments.

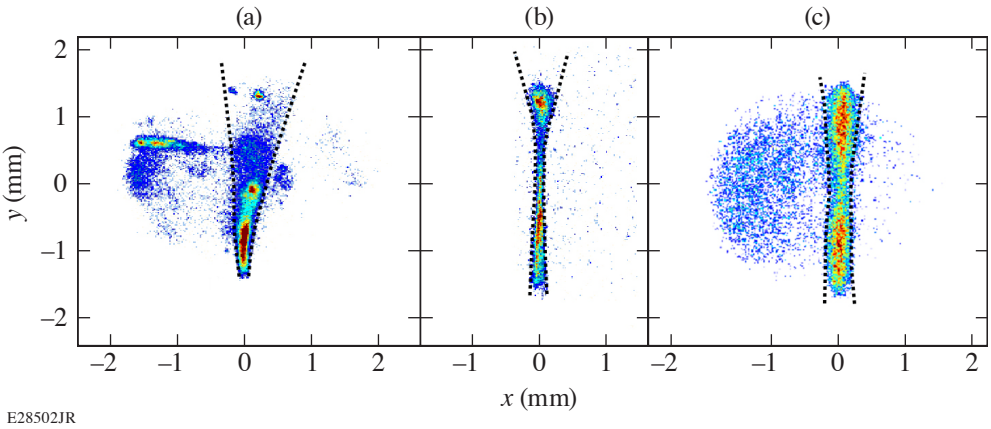

Figure 2
Two-dimensional images of Thomson-scattered light from a 2ω probe beam propagating through a gas-jet plasma (propagates from bottom to top). (a) No DPP, $P/P_c = 100$, $n_e = 4 \times 10^{20}$ cm^{-3}, $P = 45$ GW; (b) no DPP, $P/P_c = 4$, $n_e = 4 \times 10^{19}$ cm^{-3}, $P = 15$ GW; and (c) with DPP, $P/P_{c;DPP} = 0.1$, $n_e = 2 \times 10^{20}$ cm^{-3}, $P = 40$ GW.

This material is based upon work supported by the Department of Energy National Nuclear Security Administration under Award Number DE-NA0003856, the University of Rochester, and the New York State Energy Research and Development Authority.

Thresholds of Absolute Instabilities Driven by a Broadband Laser

R. K. Follett,[1] J. G. Shaw,[1] J. F. Myatt,[2] C. Dorrer,[1] D. H. Froula,[1] and J. P. Palastro[1]

[1]Laboratory for Laser Energetics, University of Rochester
[2]Department of Electrical and Computer Engineering, University of Alberta, Canada

In direct-drive inertial confinement fusion (ICF), a millimeter-scale spherical capsule is uniformly illuminated by symmetrically oriented laser beams.[1] The lasers ablate the outer layer of the capsule, which generates pressure to implode the fuel. The primary mechanism by which laser energy is converted into thermal energy in the ablator is through electron–ion collisional absorption, but a number of parametric instabilities can also occur when the lasers interact with the plasma corona of the imploding capsule, many of which can adversely affect the quality of the implosion.

Of particular importance are the stimulated Raman scattering (SRS) and two-plasmon–decay (TPD) instabilities, which correspond to the decay of an incident electromagnetic wave into an electromagnetic wave and an electron plasma wave (EPW) or into two EPW's, respectively.[2] The resulting high-phase-velocity EPW's can accelerate electrons to high energies. These energetic electrons can deposit their energy in the cold fuel, reducing the compressibility of the capsule.

It has long been known that introducing bandwidth into the drive lasers reduces the homogeneous growth rate for these instabilities,[3] and it has been shown analytically that bandwidth can increase the thresholds for absolute SRS and TPD.[4] There are no existing lasers, however, with sufficient energy and bandwidth to demonstrate instability suppression in ICF experiments. Optical parametric amplification of a broadband seed beam using a high-energy monochromatic pump beam provides a potential path toward high-energy broadband lasers. As an alternative, recent experiments have successfully demonstrated that stimulated rotational Raman scattering can increase the bandwidth of high-energy lasers.[5]

This summary presents a numerical study of absolute instability thresholds for SRS and TPD using a broadband pump beam. The calculations suggest that the absolute thresholds can be increased significantly with ~1% bandwidth at ICF-relevant conditions. Several different field spectra are considered, and it is found that the coherence time of the laser is the predominant factor in determining the effectiveness of a given pump spectrum.

Figure 1 shows absolute instability thresholds for SRS and TPD as a function of the laser period over the laser coherence time for Gaussian, Lorentzian, flat, and Kubo–Anderson process (KAP) power spectra (KAP bandwidth corresponds to a laser field that has a constant intensity but undergoes random Poisson-distributed phase jumps). The thresholds were calculated using the laser–plasma simulation environment (*LPSE*). The coherence time was defined as $\tau_c = \int_{-\infty}^{\infty} \left| g(\tau) \right|^2 d\tau$, where $g(\tau) \equiv \left\langle E_0^*(t) E_0(t+\tau) \right\rangle \Big/ \left\langle \left| E_0(t) \right|^2 \right\rangle$ and E_0 is the electric field of the pump beam. The thresholds are normalized to the analytic thresholds for a monochromatic pump[6,7]

$$I_{\mathrm{thr,SRS}}\left(10^{14}\ \mathrm{W/cm^2}\right) = \frac{858}{\left[L_n(\mu\mathrm{m})\right]^{4/3}\left[\lambda_0(\mu\mathrm{m})\right]^{2/3}}, \tag{1}$$

where L_n is the density scale length and λ_0 is the pump central wavelength.

As a function of coherence time, the thresholds for the various power spectra shown in Fig. 1 exhibit a universal scaling. This demonstrates that the pump coherence time is the predominant factor in determining how effective a laser with a given power spectrum will be for instability suppression. Despite being the only field spectrum that does not have amplitude modulation in the time domain, KAP bandwidth results in nearly the same thresholds as the other spectra, which indicates that amplitude modulation does not significantly impact the absolute threshold.

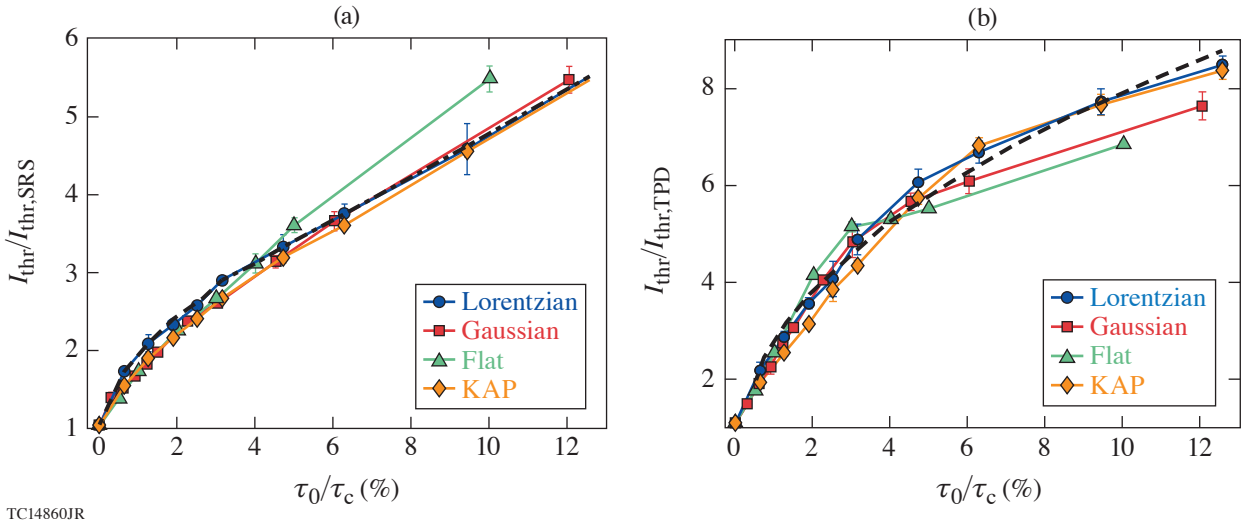

Figure 1
Absolute (a) SRS and (b) TPD thresholds from *LPSE* simulations plotted in terms of the laser period over the coherence time for an L_n = 208-μm scale length plasma with an electron temperature of T_e = 2 keV. The various field spectra are represented by blue circles (Lorentzian), red squares (Gaussian), green triangles (flat), and yellow diamonds (KAP). The error bars correspond to the standard deviation from four-run ensembles varying the random-number–generator seed for the pump spectra. τ_0 is the laser period.

Approximate scaling laws for the absolute instability thresholds were obtained by systematically varying the laser bandwidth, density scale length, central wavelength, and electron temperature:

$$I^{\tau}_{thr,SRS}\left(10^{14}\ \mathrm{W/cm^2}\right) \approx \frac{798}{L_n(\mu\mathrm{m})\,\lambda_0(\mu\mathrm{m})}\left(\frac{\tau_0}{\tau_c}\right)^{1/3}, \tag{2}$$

$$I^{\tau}_{thr,TPD}\left(10^{14}\ \mathrm{W/cm^2}\right) \approx \frac{232\left[T_e(\mathrm{keV})\right]^{3/4}}{\left[L_n(\mu\mathrm{m})\right]^{2/3}\left[\lambda_0(\mu\mathrm{m})\right]^{4/3}}\left(\frac{\tau_0}{\tau_c}\right)^{1/2}, \tag{3}$$

where T_e is the electron temperature. In addition to the bandwidth dependence in Eqs. (2) and (3), the threshold scalings with L_n, λ_0, and T_e have changed relative to the monochromatic result. Equations (2) and (3) predict that a laser with $\tau_0/\tau_c \approx 1.5\%$ would allow a doubling of the drive intensity in direct-drive implosions.

This material is based upon work supported by the Department of Energy National Nuclear Security Administration under Award Number DE-NA0003856, the University of Rochester, and the New York State Energy Research and Development Authority.

1. R. S. Craxton *et al*., Phys. Plasmas **22**, 110501 (2015).
2. W. L. Kruer, *The Physics of Laser Plasma Interactions*, Frontiers in Physics, Vol. 73 (Addison-Wesley, Redwood City, CA, 1988).
3. J. J. Thomson and J. I. Karush, Phys. Fluids **17**, 1608 (1974).
4. L. Lu, Phys. Fluids B **1**, 1605 (1989).
5. J . Weaver *et al*., Appl. Opt. **56**, 8618 (2017).
6. B. B. Afeyan and E. A. Williams, Phys. Fluids **28**, 3397 (1985).
7. A. Simon *et al*., Phys. Fluids **26**, 3107 (1983).

Complex Ray Tracing and Cross-Beam Energy Transfer for Laser-Plasma Simulations

A. J. Tu, R. K. Follett, and A. B. Sefkow

Laboratory for Laser Energetics, University of Rochester

Cross-beam energy transfer (CBET), which occurs when laser beams overlap in a plasma and drive ion-acoustic waves, may be responsible for a 50% decrease in hydrodynamic efficiency in OMEGA implosions.[1] A program was developed that models CBET for the simple case of two intersecting beams. The algorithms in this code followed a five-step process, which involved mapping ray trajectories to a grid, finding ray interactions, calculating gain coefficients for the interactions, and solving for final values through iteration.

A ray-tracing code was developed that propagates laser beams by representing them as bundles of rays and then evolving the rays in time according to the following set of differential equations:[2]

$$\frac{\mathrm{d}\mathbf{x}}{\mathrm{d}t} = v_{\mathrm{g}}, \tag{1}$$

$$\frac{\mathrm{d}\mathbf{v}_{\mathrm{g}}}{\mathrm{d}t} = -\frac{c^2 \nabla n_{\mathrm{e}}}{2n_{\mathrm{c}}}, \tag{2}$$

where $\mathbf{x}$ is the position vector, t is time, and $\mathbf{v_g}$ is the group velocity vector, defined by

$$\mathbf{v_g} = \frac{\partial \omega}{\partial \mathbf{k}} = \frac{c^2 \mathbf{k}}{\omega}, \tag{3}$$

where ω is the angular frequency, $\mathbf{k}$ is the wave-number vector, and n_{c} is the critical density, defined by

$$n_{\mathrm{c}} = \frac{\omega^2 m_{\mathrm{e}} \varepsilon_0}{e_{\mathrm{c}}^2}. \tag{4}$$

These equations take into account the dispersion relation and the density profile of the background plasma. The energy deposited by the beams, as well as the beam intensities and electric fields, can be calculated and plotted onto a grid using the first-order linear interpolation method.

To map ray trajectories and find interactions, we store an array of each ray's coordinates along its trajectory. We also keep track of the gridlines it crosses and the cells through which it passes. Two rays are said to intersect if they are from different beams and they both pass through the same grid cell.

For each interaction, we calculate the gain coefficient from the following formula:[3]

$$\left(L_s^{ijkl}\right)^{-1} = \frac{e^2 \left| E_{k0} \right|^2}{4 m_e c \omega_{ij} k_B T_e \left(1 + 3T_i / ZT_e\right)} \frac{n_e}{n_c} \frac{\omega_s}{\nu_{ia}} P\left(\eta_{ijkl}\right), \tag{5}$$

$$P(\eta) = \frac{\left(\nu_{ia}/\omega_s\right)^2 \eta}{\left(\eta^2 - 1\right)^2 + \left(\nu_{ia}/\omega_s\right)^2 \eta^2}, \tag{6}$$

$$\eta_{ijkl} = \frac{\omega_{kl} - \omega_{ij} - \left(\mathbf{k}_{kl} - \mathbf{k}_{ij}\right) \cdot \mathbf{u}}{\omega_s}, \tag{7}$$

where L_s^{ijkl} is the laser absorption length; e is the elementary charge; E_{k0} is the initial electric field of the pump ray; m_e is the electron mass; c is the speed of light; ω_{ij} and ω_{kl} are the frequencies of the seed beam and the pump beam, respectively; k_B is the Boltzmann constant; T_e is the electron temperature; T_i is the ion temperature; Z is the ionization state; n_e is the electron density; n_c is the critical density; ν_{ia} is the ion-acoustic wave energy damping rate; $\mathbf{k}_{ij}$ and $\mathbf{k}_{kl}$ are the seed and pump ray vectors, respectively; $\mathbf{u}$ is the plasma flow velocity; and ω_s is the acoustic frequency.

Once we determine the energy transfer for a single intersection, we must propagate the energy change to all downstream cells (see Fig. 1). After doing this for all possible ray intersections, we iterate the process, if necessary. This new program matches the results of Follett's CBET program,[3] which uses the same equations but different numerical algorithms; it also performs the calculations 10× faster.

Furthermore, a new ray-tracing method was investigated, namely complex ray tracing, which represents a laser beam with only five rays: a chief ray (a.k.a., base ray), two waist rays, and two divergence rays. The electric field or intensity at any point can be calculated by finding the distance between the point and three of the rays along a line perpendicular to the chief ray.[4]

We tried two different approaches to implement this technique: In the first approach (cell by cell), we traced all five rays at the beginning and then went cell by cell to calculate the intensity for each cell. While this method was very accurate, it was very slow when the number of cells became large. The second method (update outward along the chief ray) started by tracing the waist and divergence rays; then, while the chief ray was traced, we updated the intensities outward from the chief ray. This method worked quickly and accurately: it ran 4× faster than the standard ray-tracing method and produced a smoother plot.

With this program, we reproduced a basic version of Young's double-slit experiment, showing that complex ray tracing can model additional effects such as diffraction and interference. In the future, this work will be implemented into the 3-D hybrid fluid-kinetic code *CHIMERA*.

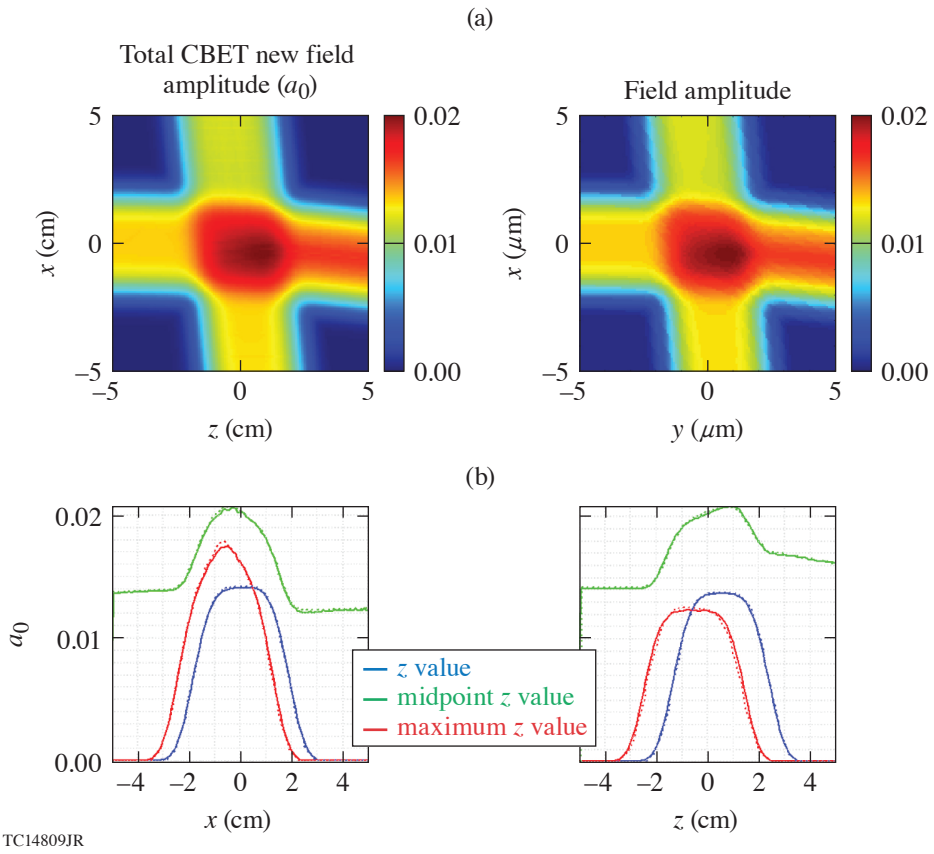

Figure 1
Comparison of Follett's CBET code[3] with the developed code. (a) Our results are on the left and Follett's results are on the right. Energy from the upward-traveling beam has been transferred to the rightward-traveling beam. (b) Our results are shown as solid lines and Follett's results are shown as dotted lines. The blue, green, and red lines show the electric-field profiles taken at the minimum z, midpoint z, and maximum z values, respectively.

This material is based upon work supported by the Department of Energy National Nuclear Security Administration under Award Number DE-NA0003856, the University of Rochester, and the New York State Energy Research and Development Authority.

1. J. F. Myatt *et al.*, Phys. Plasmas **24**, 056308 (2017).
2. T. B. Kaiser, Phys. Rev. E **61**, 895 (2000).
3. R. K. Follett *et al.*, Phys. Rev. E **98**, 043202 (2018).
4. H. Yu *et al.*, Appl. Opt. **55**, 6530 (2016).

New Thermodynamic Constraints on Internal, Thermal, and Magnetic States of Super-Earths

M. Zaghoo

Laboratory for Laser Energetics, University of Rochester

The discovery of exoplanetary systems orbiting host stars has revolutionized planetary astronomy. As we begin to understand the diversity of these planets' architectures across a wide range of planet–star separation, we rely on transit-based methods to characterize their masses, radii, albedo, and soon, atmospheres. Ascertaining planetary structure, evolution, and habitability require, however, a better understanding of key internal geophysical and geochemical processes that drive the planetary geochemical differentiation, internal composition, core sizes, and heat budgets, all of which depend on the behavior of planetary constituent materials, particularly silicates and iron, at extreme conditions.

In the past few years, advances in high-pressure physics experiments, particularly those employing ramp-dynamic compression tools, have addressed this challenge.[1] The experiments provided precise data on the compressibility of iron, its Grüneisen parameter,[2,3] and the solidus line of $MgSiO_3$ (Ref. 4) as well as its conductive behavior at conditions comparable to 4 to 5 M_E (Ref. 5). Additionally, recent static high-pressure experiments revealed that liquid iron's thermal conductivity at conditions corresponding to Earth's core mantle boundary (CMB) is substantially higher than values previously used in the geophysics literature.[6,7]

In this work, we derive new thermodynamic data using recent experimental results on both iron and silicates to better model the internal states for super-Earth (SE) planets ranging from 1 to 10 M_E (see Fig. 1). We combine the state-of-the-art equation of state and melting experimental data with parametric thermal evolution models to obtain new pressure, density, and temperature radial profiles of these planets. We reveal that for planets more massive than 3 M_E, a thick layer of deep magma oceans surrounding solid iron cores will develop. We present new theoretical data on the thermal conductivity of SE's iron cores at extreme conditions, based on the revised estimates for Earth's values, and carefully assess the power requirements required to maintain the convective state of these cores. We show that the drastic rise in the conductive losses along the CMB will dominate the heat

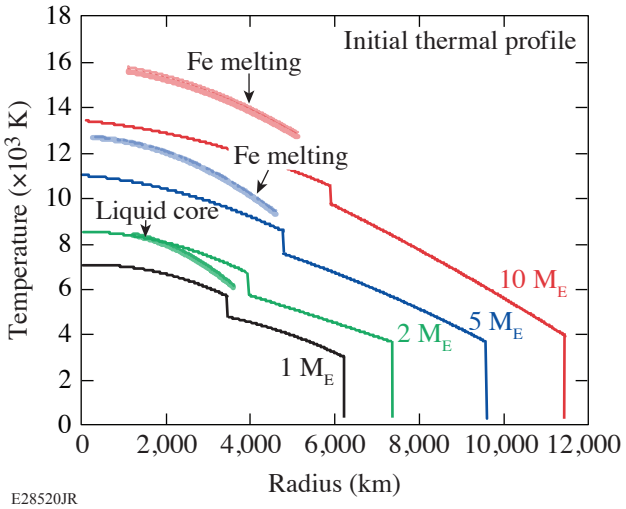

Figure 1
Radial thermal structure profiles of rocky SE planets ranging from 1 to 10 M_E calculated within the thermal boundary layer model. Also shown are the pure-Fe liquidus lines. The shaded area represents the reduction in the melting line caused by added impurities. The intersection of the thermal profile with the liquidus denotes the onset of iron crystallization, the inner core boundary. For planets 4 to 10 M_E, the liquidus does not cross the planetary thermal profile, meaning that these planets will likely lack an iron fluid core.

flux in the more-massive planets, driving their cores into a sub-adiabatic and non-convective state. Absent substantial intrinsic heat sources, the cessation of convection will consequently shut down the dynamo action in their cores. Our results lend support to the recently proposed concept of "super habitability," employed to describe terrestrial-like planets with enhanced characteristics amenable to their habitability.[8] We have shown that it most likely extends up to only ~4 M_E; beyond which, a new paradigm that describes the suitability of carbon-based life forms on more-massive rocky planets might be needed.

This material is based upon work supported by the Department of Energy National Nuclear Security Administration under Award Number DE-NA0003856, the University of Rochester, and the New York State Energy Research and Development Authority.

1. T. Duffy, N. Madhusudhan, and K. K. M. Lee, in *Treatise on Geophysics*, 2nd ed., edited by C. Schubert (Elsevier, Oxford, 2015), Vol. 2.
2. R. F. Smith *et al*., Nat. Astron. **2**, 452 (2018).
3. J. K. Wicks *et al*., Sci. Adv. **4**, eaao5864 (2018).
4. D. E. Fratanduono *et al*., Phys. Rev. B **97**, 214105 (2018).
5. R. M. Bolis *et al*., Geophys. Res. Lett. **43**, 9475 (2016).
6. H. Gomi *et al*., Phys. Earth Planet. Inter. **224**, 88 (2013).
7. K. Ohta *et al*., Nature **534**, 95 (2016).
8. R. Heller and J. A. Armstrong, Astrobiology **14**, 50 (2014).

Exchange-Correlation Thermal Effects in Shocked Deuterium: Softening the Principal Hugoniot and Thermophysical Properties

V. V. Karasiev, S. X. Hu, M. Zaghoo, and T. R. Boehly

Laboratory for Laser Energetics, University of Rochester

Reliably predicting the properties of hydrogen and its isotopes under extreme conditions remains a problem of great importance and broad scientific interest. Accurate knowledge of the equation of state (EOS) and transport properties over a wide range of thermodynamic conditions of this simplest and most-abundant element in the universe is used as input for planetary astrophysics models to describe interiors of planets[1] as well as the inertial confinement fusion (ICF) simulations to design targets.[2–4] The most-advanced theoretical and computational methods are used to interpret experimental results and to predict properties at thermodynamic conditions that are difficult to access experimentally.

On the other hand, new experimental measurements with improved accuracy[5,6] serve as an important benchmark to assess the accuracy of theoretical predictions. It was found[6] that recent shock-compression data for deuterium are well described by finite-temperature density functional theory (DFT) methods.[7–9] Standard generalized gradient approximation (GGA) exchange-correlation (XC) functionals such as Perdew–Burke–Ernzerhof (PBE)[10] describe the peak compression reasonably well, but at pressures above 250 GPa along the Hugoniot, the DFT calculations with the PBE functional predict a stiffer behavior than recent experimental data.[5]

All current DFT calculations of the Hugoniot data and transport coefficients are performed with temperature-independent XC functionals developed for ground state;[4,6,11–14] therefore, XC thermal effects, which play an important role in warm-dense-matter (WDM) conditions,[15] are not taken into account. Figure 1 shows the (r_s,t) domain where the temperature dependence of XC might be important for accurate predictions. The relative importance of XC thermal effects is shown as a function of the Wigner–Seitz radius $r_s = (3/4\pi n)^{1/3}$ and reduced temperature $t = T/T_F$, where $T_F = (3\pi^2 n)^{2/3}/2k_B$ is the Fermi temperature and n is the electron number density. XC thermal effects might become important for t values around a few tenths and above. Here we

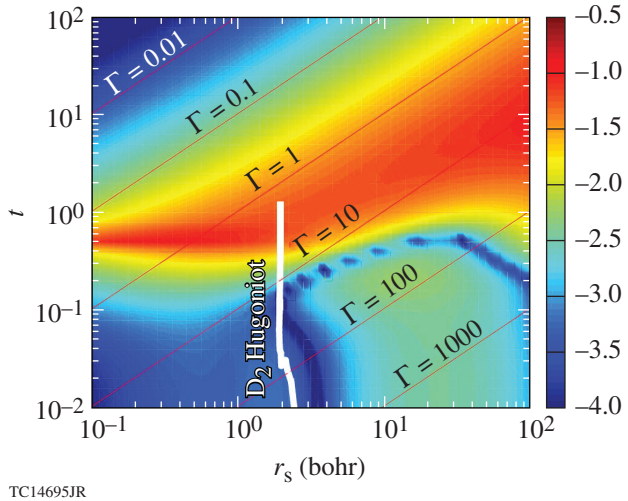

TC14695JR

Figure 1

The relative importance of explicit temperature dependence in the XC free-energy functional for the homogeneous electron gas measured as $\log_{10}\left\{\left|f_{xc}(r_s,t)-e_{xc}(r_s)\right|/\left[\left|f_s(r_s,t)\right|+\left|e_{xc}(r_s)\right|\right]\right\}$, where f_{xc} is the XC free-energy per particle given by the corrKSDT parameterization,[16,17] e_{xc} is the zero-temperature XC energy per particle,[18] and f_s is the noninteracting free energy per particle.[19] $\Gamma = 2\lambda^2 r_s/t$ with $\lambda = (4/9\pi)^{1/3}$ is the classical coupling parameter. The solid white line corresponds to the liquid deuterium principal Hugoniot path; the end point corresponds to $P = 1$ TPa.

focus on the study of the optical and transport properties along the principal Hugoniot of deuterium with a temperature-dependent Karasiev–Dufty–Trickey (KDT16) generalized gradient approximation XC functional.[16]

Figure 2 compares our theoretical predictions and experimental results across the molecular-to-atomic (MA) transition (low-pressure range $P < 150$ GPa) (Ref. 6). Both functionals, KDT16 and PBE, are in good agreement with experimental measurements in the range of pressure up to 200 GPa. At higher pressures, however, the PBE curve becomes noticeably stiffer as compared to the recent experimental data;[5] the disagreement reaches about 4% at $P = 550$ GPa. The KDT16 predicts a curve that is softer by slightly more than 1% beyond 250 GPa as compared to PBE. Increasing the simulation cell size from 64 to 128 atoms in this range of pressure leads to further softening of the Hugoniot. The KDT16 compressibility is within the experimental uncertainty in the entire pressure range (including high pressures $P > 250$ GPa). Therefore, the inclusion of XC thermal effects in calculations makes the deuterium Hugoniot softer at $P > 250$ GPa and improves agreement with the experimental data; the KDT16 XC functional is able to describe the principal Hugoniot of liquid deuterium consistently over the entire pressure range.

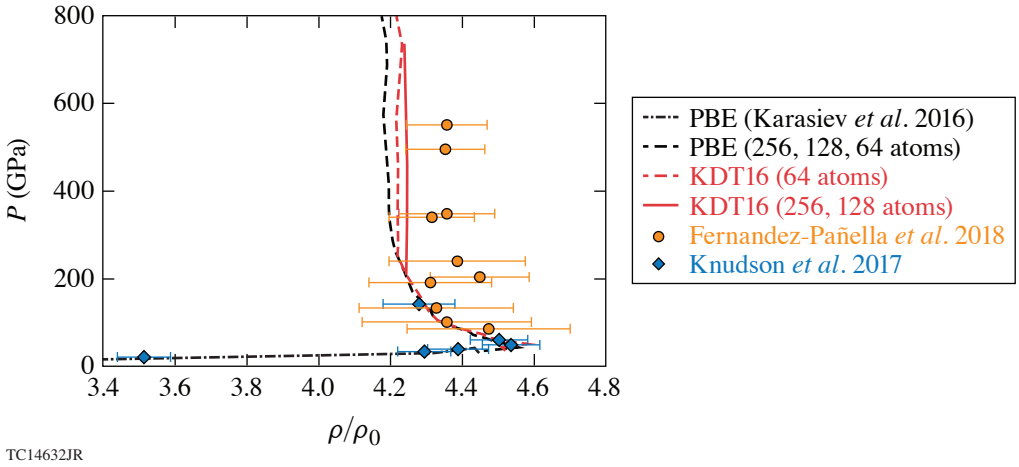

Figure 2
Deuterium principal Hugoniot derived from the initial state $\rho_0 = 0.172$ g/cm^3 and $T_0 = 20$ K. The PBE (dashed black) and KDT16 (dashed red) curves are obtained by combining results from simulations with 256 atoms ($6 \le T \le 20$ kK, pressure range between 34 and 86 GPa for both functionals), 128 atoms ($25 \le T \le 50$ kK, pressure range between 104 and 208 GPa for KDT16), 64 atoms ($60 \le T \le 150$ kK, pressure range between 253 and 736 GPa for KDT16), and 32 atoms for $T = 200$ kK. The solid red curve corresponds to the KDT16 results from simulations with 256 atoms ($6 \le T \le 20$ kK) and 128 atoms ($25 \le T \le 150$ kK).

The reflectivity along the deuterium Hugoniot was calculated at 532 and 808 nm with the KDT16 XC functional and our predicted value of the refractive index. Results of recent experiments[20] on OMEGA and previous measurements[21] are shown in Fig. 3. There is excellent agreement between the KDT16 values and experimental data at 808-nm wavelength for the range of shock speeds considered in calculations, even though the experimental data have relatively large error bars. The KDT16 results at 532 nm are in very good agreement with recent OMEGA experimental data for shock speeds below 50 km/s. The reflectivity is underestimated by the DFT calculations at high shock speeds $U_s > 50$ km/s as compared to the experiment. Experimental reflectance as a function of shock speed changes the slope at U_s near 45 km/s ($T \approx 0.4\ T_F = 60$ kK); this change in the slope is related to lifting of the Fermi degeneracy. The system starts to behave as a classical one at a significantly lower temperature as compared to T_F (see details in Ref. 20). Calculated KDT16 reflectivity at the same 532-nm wavelength rises very quickly from 0.29 at 16 km/s ($T \approx 6$ kK) to 0.39 at 20 km/s ($T \approx 12$ kK), which roughly corresponds to maximum compression near molecular-to-atomic transition; it slowly continues to increase and near 43 km/s the slope also increases.

The deuterium system along the Hugoniot experiences transformations from an insulating molecular liquid to atomic poor metallic liquid and finally to nondegenerate classical plasma. The signature of the molecular-to-atomic transition is found in a sharp increase of electrical dc conductivity and reflectivity at shock speeds in the range between 16 and 20 km/s (a range of temperature

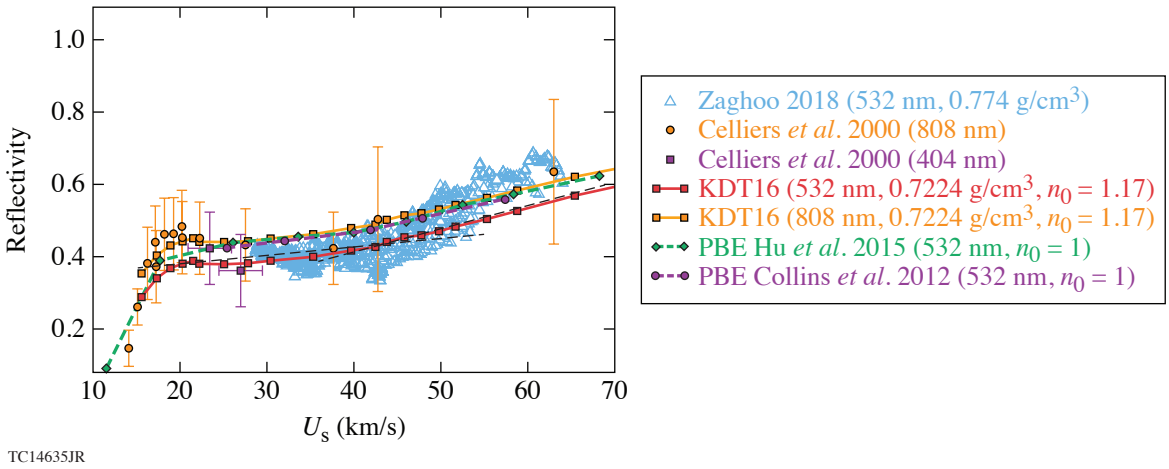

Figure 3
Reflectivity of shocked deuterium. Theoretical DFT predictions and experimental data are compared.

between 6 and 12 kK). An increase in the slope of calculated reflectivity at $U_s \approx 43$ km/s ($T \approx 0.4\ T_F = 60$ kK), related to the breakdown of the electrons' degeneracy and emergence of classical statistics,[20] is in agreement with experimental measurements.

Our results confirm that the crossover between the quantum and classical statistics occurs below the $T = T_F$ limit. This is apparent in the observed change in the transport and the thermodynamic properties of the deuterium fluid in the region of 0.4 to 0.65 T_F. Future work should investigate the dependence of the onset of this crossover on density.

This material is based upon work supported by the Department of Energy National Nuclear Security Administration under Award Number DE-NA0003856 and U.S. National Science Foundation PHY Grant No. 1802964.

1. J. J. Fortney and N. Nettelmann, Space Sci. Rev. **152**, 423 (2010).
2. S. X. Hu *et al*., Phys. Rev. B **84**, 224109 (2011).
3. S. X. Hu *et al*., Phys. Rev. E **90**, 033111 (2014).
4. S. X. Hu *et al*., Phys. Plasmas **22**, 056304 (2015).
5. A. Fernandez-Pañella *et al*., "Shock Compression of Liquid Deuterium up to 1 TPa," to be published in Physical Review Letters.
6. M. D. Knudson and M. P. Desjarlais, Phys. Rev. Lett. **118**, 035501 (2017).
7. N. D. Mermin, Phys. Rev. **137**, A1441 (1965).
8. M. V. Stoitsov and I. Zh. Petkov, Ann. Phys. **184**, 121 (1988).
9. R. M. Dreizler, in *The Nuclear Equation of State. Part A: Discovery of Nuclear Shock Waves and the EOS*, edited by W. Greiner and H. Stöcker, Nato Science Series B (1989), pp. 521–532.
10. J. P. Perdew, K. Burke, and M. Ernzerhof, Phys. Rev. Lett. **77**, 3865 (1996); **78**, 1396(E) (1997).
11. B. Holst, R. Redmer, and M. P. Desjarlais, Phys. Rev. B **77**, 184201 (2008).
12. L. Caillabet, S. Mazevet, and P. Loubeyre, Phys. Rev. B **83**, 094101 (2011).
13. L. A. Collins *et al*., Phys. Rev. B **63**, 184110 (2001).
14. L. A. Collins, J. D. Kress, and D. E. Hanson, Phys. Rev. B **85**, 233101 (2012).

15. V. V. Karasiev, L. Calderín, and S. B. Trickey, Phys. Rev. E **93**, 063207 (2016).

16. V. V. Karasiev, J. W. Dufty, and S. B. Trickey, Phys. Rev. Lett. **120**, 076401 (2018).

17. V. V. Karasiev *et al*., Phys. Rev. Lett. **112**, 076403 (2014).

18. J. P. Perdew and A Zunger, Phys. Rev. B **23**, 5048 (1981).

19. R. P. Feynman, N. Metropolis, and E. Teller, Phys. Rev. **75**, 1561 (1949).

20. M. Zaghoo *et al*., Phys. Rev. Lett. **122**, 085001 (2019).

21. P. M. Celliers *et al*., Phys. Rev. Lett. **84**, 5564 (2000).

Spatiotemporal Flat Field of the Gated Optical Imager Used on the 3ω Beamlets Diagnostic

J. Katz, N. Whiting, and S. T. Ivancic

Laboratory for Laser Energetics, University of Rochester

Introduction

Gated optical imagers (GOI's) use microchannel-plate (MCP)–type intensifier tubes to electronically control the exposure duration of a 2-D image. Short exposure durations can be used to reduce motion blur in a dynamic scene or reject late-time sources of background noise such as ghost reflections or persistent thermal emission. The current state-of-the-art high-speed GOI's that use 18-mm-diam image tubes can achieve gate times of the order of 100 ps (Refs. 1 and 2). In the gated-off state, the entrance face of the MCP is negatively biased relative to the photocathode, preventing the flow of electrons to the MCP. The tube is gated on by applying a positive voltage pulse to a photocathode that temporarily overcomes a preimposed bias. Photoelectrons can then pass through the MCP amplification stage and are imaged on a phosphor screen. The MCP tube geometry and electrical capacitance of the photocathode influence the speed at which a transient voltage can be applied to the tube surface. In the fastest regimes the gating process is both spatially and temporally dynamic. Different regions of the image see different on/off times and exposure durations as the gate pulse propagates across the photocathode. Quantitative knowledge of the overall detector sensitivity as a function of position and time is required to accurately compare data recorded at different image positions. This type of calibration is critical to the 3ω beamlets diagnostic on OMEGA, which simultaneously records a four-frame image on a single exposure.[3] The beamlet energy, polarization state, and temporal evolution are determined by comparing the individual beamlet signals in each subimage.

Calibration Apparatus

A short-pulse laser was used to map out the optical gate profile over a series of image acquisitions by triggering the GOI at different times with respect to the incoming pulse (Fig. 1). A frequency-doubled Ti:sapphire (λ = 395-nm) laser with 1-ps pulse duration was up-collimated to ~20-mm diameter and free-space propagated to the GOI photocathode. The up-collimator produced a relatively flattop beam profile by selecting only the central 1/10th of the original Gaussian laser near field. A sample of the laser pulse was split and fiber coupled for use as an energy and timing reference. Once fiber coupled, the pulse was split again with one leg sent to a time-integrated energy meter and the second leg sent to a high-speed (90-ps) photodiode. The photodiode output and an electrical monitor pulse produced from the GOI pulser were recorded on separate channels of an 8-GHz oscilloscope

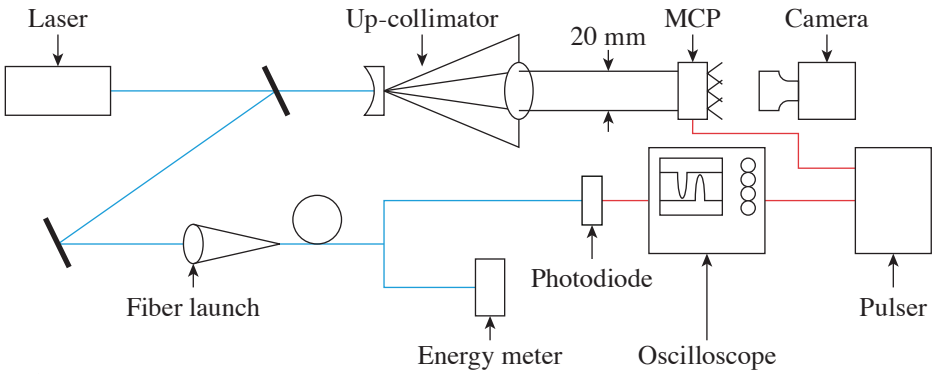

E28514JR

Figure 1
A laser with 1-ps pulse duration is used to characterize the GOI gate as a function of time and image position. The arrival time of the laser pulse relative to the GOI trigger is varied over a series of image acquisitions to map out the gate profile. An oscilloscope measures the laser timing relative to a monitor of the GOI gating pulse. The energy of each incident pulse is quantified using an energy meter.

sampling at 40 Gs/s. The relative trigger time for each image frame was measured by comparing the reference pickoff timing to the monitor pulse and was determined with 5-ps accuracy. The pulse energy was also measured by integrating the photodiode oscilloscope trace. Agreement between the two pulse energy measurements was 2.5% rms, allowing fluctuations in laser pulse energy to be corrected for in each image frame.

Generation of a Flat-Field Calibration

To establish the baseline spatial uniformity of the illumination beam, a series of images were collected with the GOI in slow gate exposure mode. The slow gate setting provides millisecond exposure durations using separate gating circuitry. The flat-field images are used to quantify intensity nonuniformities introduced by the laser near field, diffraction from the up-collimator, and dust particles on the transport optics. The scan of the fast gate included ~85 shots. A system jitter of ±50 ps prevents the scan from being generated with equal spacing time steps but timing information can be recovered to ±5 ps by fitting the monitor and diode traces in post-processing. By sorting the acquisitions by trigger time, a gain history with approximately 5-ps sample intervals is generated. As shown in Fig. 2(a), the 3ω beamlets' GOI has an exposure duration of approximately 250 ps. A sensitivity figure of merit $G(x,y)$ is calculated by integrating the gate history as a function of time on a pixel-by-pixel basis, given by Eq. (1).

$$G(x,y) = \frac{1}{\mathrm{FF}(x,y)} \sum_{i}^{n} \frac{I_{i+1}(x,y) + I_i(x,y)}{2E_i} \left(t_{i+1} - t_i\right), \tag{1}$$

where $I(x,y)$ is the signal intensity of a given image pixel on the ith image in the set, t_i is the relative time that the image was acquired, E_i is the corresponding pulse energy, and FF is the normalized image from the slow-gate flat field. Equation (1) generates a composite image that contains the time-integrated gain sensitivity as a function of image position [Fig. 2(b)].

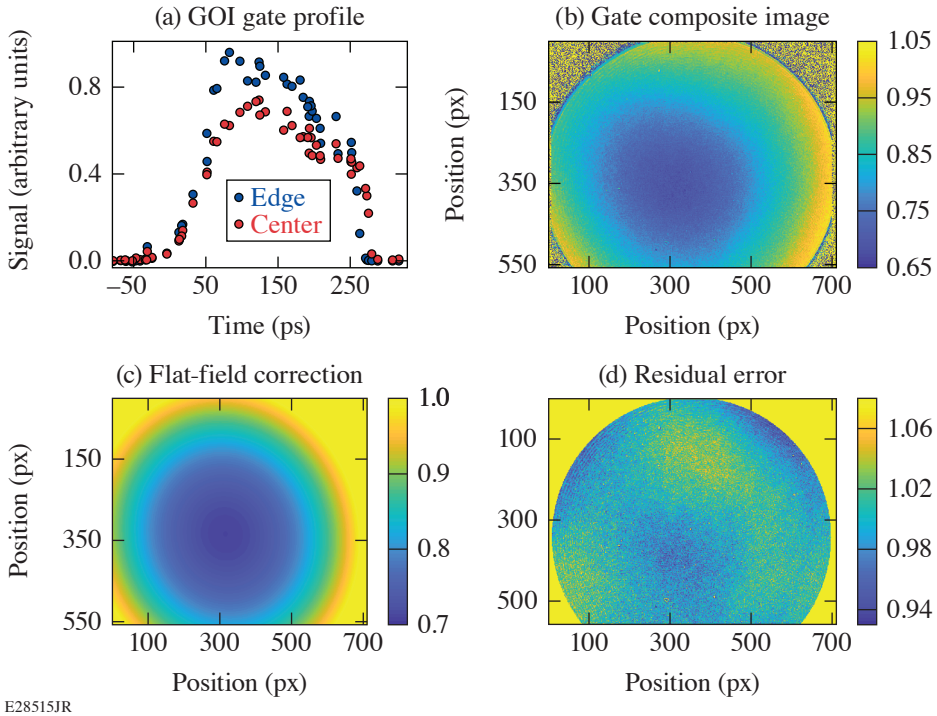

Figure 2

(a) The gain as a function of time is shown at two different pixel locations on the GOI image. (b) A composite image is generated by integrating the gain history at each point in the image. (c) The flat-field calibration function is generated by fitting the composite image fit with a 2-D second-order polynomial. (d) Dividing the composite image by the flat-field function corrects the spatial variations in gain to 2.2% rms.

Figure 2(b) shows the measured sensitivity as a function of image position. The edges of the MCP tube are more sensitive than the center. The magnitude of sensitivity variation is a function of bias voltage. In general, faster gate times can be achieved for a given electrical gate pulse by increasing the MCP to photocathode bias. In this case, electrons flow only during the peak portion of the gate pulse. However, this also results in a lower electron extraction field, making the gating process more sensitive to variations in extraction field uniformity. Excessive bias produces fast gate profiles but can result in a complete lack of sensitivity in the image center. Ultimately the bias setting is a compromise between spatial sensitivity uniformity and gate speed. Recording the spatiotemporal flat field at different settings allows the bias voltage to be optimized. In the case of the standard beamlets configuration, the 250-ps gate duration is accompanied by a 40% peak-to-valley (p–v) variation in sensitivity from the image center to the edge.

A smooth and continuous calibration function was generated from the composite gate image by fitting it to a 2-D second-order polynomial [Fig. 2(c)]. The fitting process averages out pixel-to-pixel statistical noise and smooths residual features from diffraction and dust that persisted after flat fielding. Figure 2(d) shows the residual sensitivity variation of the original composite image after the flat-field correction. Dividing the composite image by the correction function results in a 2.2% rms variation in measured signal intensity with a p–v of ~6%.

Conclusions

A short-pulse laser and precision trigger monitor system were used to generate a spatiotemporal flat field for a high-speed GOI used in the 3ω beamlets. Measuring the detector sensitivity as a function of time and image position makes it possible to optimize the GOI operating voltages. A method for averaging calibration data into a single scalar correction function is described. Implementation of the correction function reduces spatial gain variations from ~40% p–v and 9.3% rms to 6% p–v and 2.2% rms.

This material is based upon work supported by the Department of Energy National Nuclear Security Administration under Award Number DE-NA0003856, the University of Rochester, and the New York State Energy Research and Development Authority.

1. P. E. Young *et al*., Rev. Sci. Instrum. **59**, 1457 (1988).
2. B. Little, Rev. Sci. Instrum. **89**, 10E117 (2018).
3. D. H. Edgell *et al*., Rev. Sci. Instrum. **89**, 10E101 (2018).

Co-Timing UV and IR Laser Pulses on the OMEGA EP Laser System

W. R. Donaldson and A. Consentino

Laboratory for Laser Energetics, University of Rochester

Independently managing the timing of individual beams so they all arrive at the target at the time specified by the principal investigator is crucial to the success of experiments on the OMEGA EP Laser System. A streak camera is used to observe the x rays emitted when the laser beams strike a gold target, while an optical streak camera is used to measure the UV pulses. Correlating the signal on the two instruments gives a timing accuracy of 10 ps for the short-pulse IR beams and 20 ps for the long-pulse UV beams.

OMEGA EP is a four-beam, kilojoule-class laser system.[1] The four beams can be configured to produce different pulse shapes with durations ranging from 100 ps to 10 ns and energies up to 10 kJ with a wavelength of 351 nm, or up to two of the beams may propagate to the target chamber without being converted to the UV. Instead, the IR light passes through a grating compressor[2] and is delivered to the target as a 1- to 10-ps Gaussian pulse with up to 1 kJ of optical energy. The users of this facility can perform experiments where the beams arrive at the target with adjustable relative delays.

If two pulse shapes are identical, an overlap can be used for alignment as in shown in Fig. 1(a). For non-identical pulse shapes, the timing criteria become more complicated as shown in Figs. 1(b) and 1(c).

OMEGA EP has adopted the following conventions for co-timing the various beam configurations: UV pulses are considered to be co-timed when the points on the rising edge, corresponding to the 2% level of the peak, reach the target simultaneously. For the IR beams, co-timing means that the peak of the Gaussian pulse shape arrives at the target simultaneously, regardless of the width of the pulses. When both IR and UV pulses are co-timed, the peak of the IR Gaussian is aligned with the 2% point on the rising edge of the UV pulse. Of course, any of the beams can be mistimed to produce the arrival times desired by the principal investigator, but the mistimings are always specified relative to the timed definitions.

The co-timing system begins by recording the UV pulse shapes on an optical streak camera[3] as shown in Fig. 2. The signals arrive at the streak camera arbitrarily but at deterministic and reproducible times resulting from the optical-path differences from the pickoff. The arrival times at target chamber center are determined by x rays generated by the optical pulses and measured on an x-ray streak camera. Also recorded on the optical streak camera is an eight-pulse, 1.8-GHz comb pulse tied to the master clock of OMEGA EP. This fiducial links the measured optical pulse to the outputs of the other diagnostics on the system, thereby enabling one to convert the relative timings measured on the streak camera into absolute system times. The PJX x-ray streak camera, developed at LLE,[4] allows one to measure an x-ray pulse with picosecond time resolution and can be mounted in a ten-inch manipulator directly on the OMEGA EP target chamber. Figure 3 shows the output image of the PJX streak camera for the two different timing configurations.

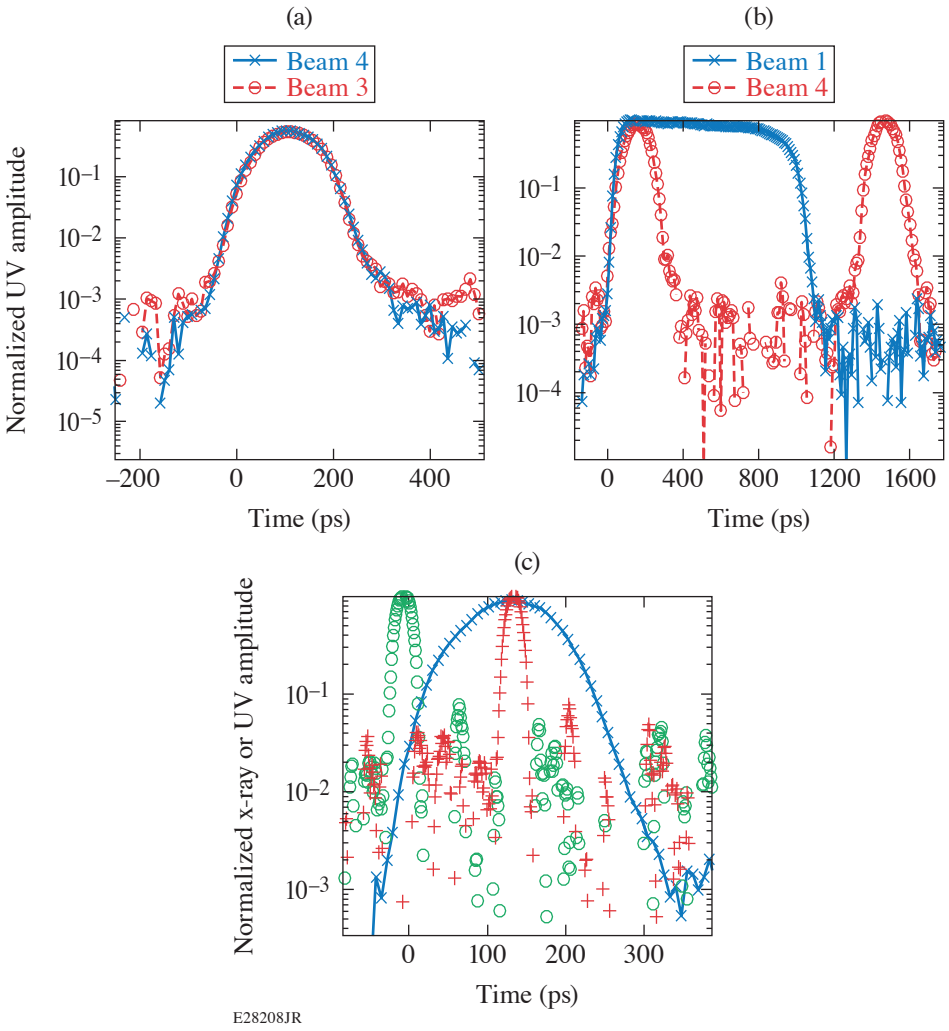

Figure 1
(a) The temporal alignment of two UV pulses with identical shapes. Any point can be used for the alignment. (b) Two dissimilar UV pulse shapes must be aligned by matching equal normalized amplitude points on the rising edge. (c) The UV (blue ×'s) and IR (green circles) are timed such that the peak of the IR pulse coincides with the 2% point of the UV pulse. An alternative timing where the peaks coincide is shown by the red crosses. This timing is not applicable with all UV shapes.

If the system is properly co-timed, the leading x-ray image of each of the four UV beams, shown in Fig. 3(a), should align in the temporal (vertical) direction. In the short-pulse to long-pulse configuration, shown in Fig. 3(b), the peaks of the two short-pulse beams should align with the 2% point on the leading edge of the long-pulse UV beam. Exact timing at the picosecond level requires a quantitative analysis of these images.

The target consists of a 25-μm-thick, 3-mm × 3-mm sheet of polyimide coated with 0.5 μm of gold. The total energy in each UV beam is ~170 J, giving ~85 J in each of the two 100-ps Gaussians; therefore, the peak intensity is ~5×10^{15} W/cm^2. At this intensity, at 351 nm, the temporal profile of the x-ray pulse matches that of the UV pulse as seen in Fig. 4. The x-ray temporal

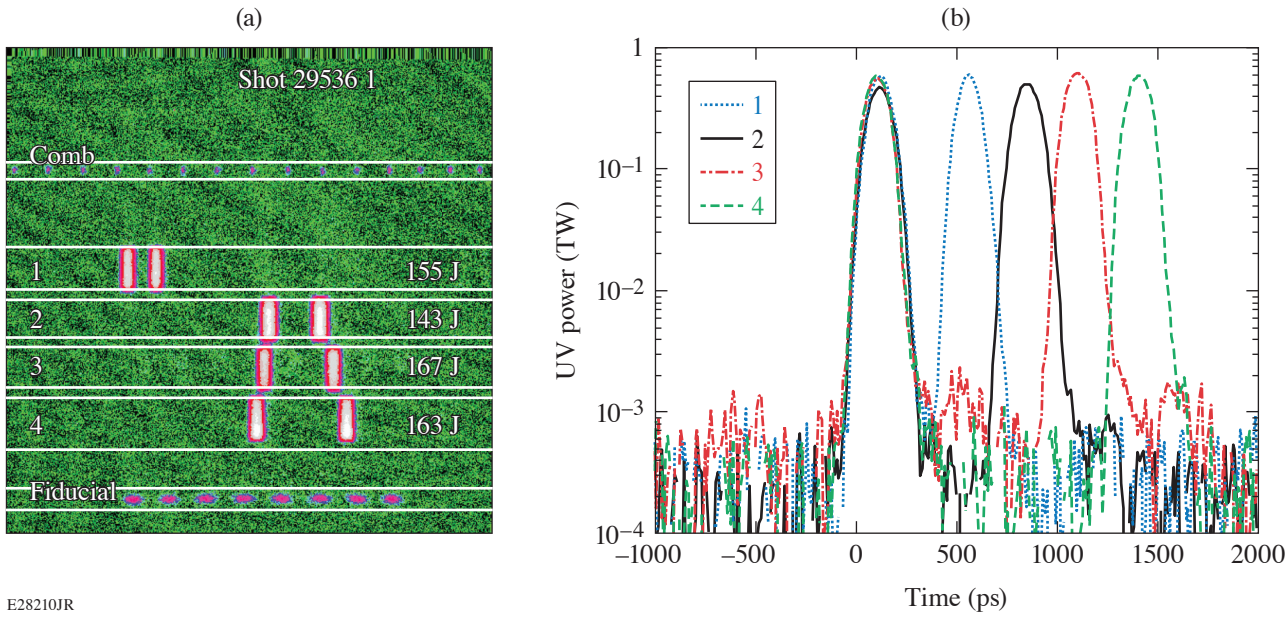

Figure 2
(a) The raw image from the UV streak cameras showing the four double-Gaussian pulse shapes and the two timing comb pulses; (b) the integrated lineouts from the UV ROSS camera of the four beams with the calibrated temporal alignment applied.

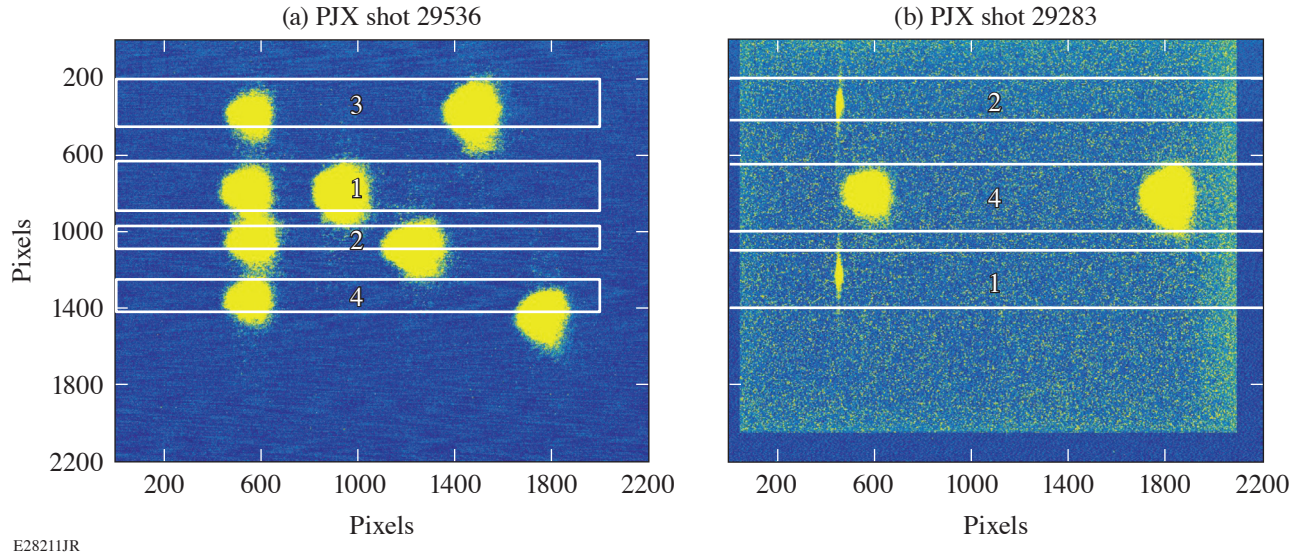

Figure 3
(a) The x-ray streak-camera image of a four-beam, long-pulse shot showing eight pulses from the four beams. (b) Two short-pulse IR beams and one UV beam strike the target. The temporal calibration is ~1 ps per pixel.

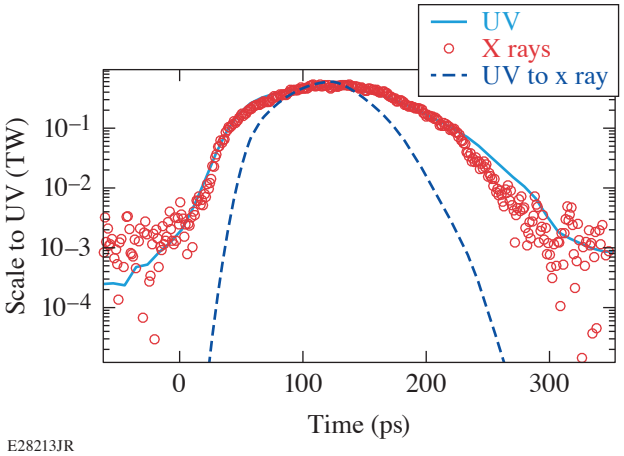

Figure 4
The x-ray temporal pulse shape (red circles) matches the measured UV pulse shape (solid blue line). The dashed blue line is the UV optical power raised to the 3.4 power, which is typical of UV to x-ray conversion at lower powers and obviously does not match the x ray at these intensities.

pulse shape matches the measured UV pulse shape. At intensities below 10^{14} W/cm^2, the emitted x rays typically follow the UV power to the 3.4 power.[5] When the UV optical power is raised to 3.4 power, the power-law conversion obviously does not match the x-ray temporal profile. This is advantageous in processing the data because when the x-ray and UV peaks are aligned, the 2% points on the leading edge, which are the actual timing points, are also aligned.

This is particularly important when timing the short-pulse beams. The IR pulses are treated differently. The shortest pulse duration, 1 ps, is at or below the resolution limit of the PJX streak camera, so the timing campaigns operate with IR pulse durations of 10 ps at best focus of the laser system. No substructure can be discerned in the x rays generated by the IR pulses. The IR x-ray data are fitted with a Gaussian to find the peak. It is worthwhile to note that the 2% point on the IR-generated x ray is at or below the noise floor, making that point inaccessible.

The UV-to-UV and UV-to-IR timing campaigns are run every three months, typically with a three-month separation between the two types of campaigns. The typical variations are less than the 20 ps, which is actually better than the current OMEGA EP timing specification of 25 ps for all beams. Therefore, OMEGA EP maintains a beam-to-beam timing of 20 ps by simultaneously measuring the optical pulse and the x rays generated when that optical pulse strikes a gold target. By operating in a high-intensity regime, the x ray's pulse shape closely tracks the optical pulse, which facilitates the timing.

This material is based upon work supported by the Department of Energy National Nuclear Security Administration under Award Number DE-NA0003856, the University of Rochester, and the New York State Energy Research and Development Authority.

1. J. H. Kelly *et al.*, J. Phys. IV France **133**, 75 (2006).
2. J. Qiao *et al.*, in *The International Conference on Ultrahigh Intensity Lasers: Development, Science and Emerging Applications (ICUIL 2008)* (ICUIL, Tongli, China, 2008), p. 107.
3. W. R. Donaldson *et al.*, Rev. Sci. Instrum. **73**, 2606 (2002).
4. P. A. Jaanimagi *et al.*, Proc. SPIE **5580**, 408 (2005).
5. F. J. Marshall *et al.*, Phys. Plasmas **11**, 251 (2004).

Current Status of Chirped-Pulse–Amplification Technology and Its Applications

S.-W. Bahk

Laboratory for Laser Energetics, University of Rochester

Chirped-pulse amplification (CPA) is a technology that has become the basis of high-peak-power lasers.[1] The intensity of the electromagnetic field has been dramatically increased since its invention. CPA is an amplification scheme that allows safe amplification of a pulse to high energy. A short low-energy pulse is stretched in time and is injected into an amplifier. After amplification to high energy, the pulse is compressed back to the original short pulse. We discuss key components of CPA in this summary.

We will first discuss the optical pulse compressor and stretcher. The compressor is made up of two parallel gratings in double pass or four gratings in single pass.[2] The accumulated holographic phase through the grating pair is a quadratic function of the frequency, which introduces chirp in time. Large-scale tiled compressors for petawatt facilities have been demonstrated at OMEGA EP[3] and PETAL.[4] A stretcher is a compressor with an imaging system.[5] The imaging system renders the effective optical distance between the two gratings negative as the image of the first grating is formed behind the second grating. The original lens-based imaging system in the stretcher has been replaced with a reflective Offner imaging system.[6]

Amplifiers are based on either optical pumping and stimulated emission or parametric amplification. Laser-diode pumping is most efficient but flash lamps or secondary pump lasers are commonly used for optical pumping. The most widely used femtosecond amplification medium is titanium sapphire, which can amplify a wide range of frequencies, is not easily saturated even at high-energy pulses, and has high amplification efficiency. It is pumped mainly by the second-harmonic pulse of the neodymium lasers. The internal self-lasing problem is a disadvantage but it can be prevented by adding a black coating around the crystal. In the parametric amplification process, the energy in the pump beam is instantaneously transferred to the injection seed beam. Since there is no energy remaining in the crystal, there is no thermal lensing problem. On the other hand, since the temporal and spatial nonuniformity of the pump pulse is directly transferred to the input pulse, a complicated and expensive hardware system is required to manage the pulse. In addition, the limited temporal and spatial overlap reduces the amplification efficiency because the group velocity and direction of the input and pump pulses in the crystal are different. The angle of the pump and the input must be precisely adjusted to meet the phase-matching requirements of the broad frequency band. Lithium triborate, beta-barium borate, and potassium dihydrogen phosphate (KDP) crystals are often used. Stimulated-emission amplifiers and parametric amplifiers may be mixed in some cases.[7] Since deuterated KDP has already been developed for use as a frequency-conversion medium in laser fusion facilities, efforts are being made to utilize it for amplifying large-scale, high-energy broadband pulses.[8]

The spatial and temporal control of a pulse are important to provide the necessary experimental conditions. The focused beam intensity can be greatly increased by an adaptive optic system,[9] which consists of a deformable mirror and a feedback system connected to a wavefront sensor. The deformable mirror has a number of piezoelectric or mechanical actuators attached to the back side of the mirror substrate. The mechanical type has the advantage of maintaining the state even after the power is off. The quality of pulse compression can be similarly improved by controlling the spectral phase of the pulse. It is possible to remove the third-order dispersion by slightly adjusting the angle of the compressor, but the fourth- or higher-order terms can be removed by an acousto-optic programmable dispersion filter.[10] When the dispersion of the pulse is not spatially uniform, spatiotemporal coupling occurs at focus. The radial group delay in refractive image relays disperses the focus in the longitudinal direction and significantly reduces the intensity of the light. A diffractive lens has the opposite angular dispersion than a refractive lens and,

therefore, can eliminate radial group delay.[4] Another application of the diffractive lens is "flying focus." The longitudinal chromatic aberration of the diffractive lens and the chirp of the pulse are combined to create the effect of longitudinal focal spot sweeping in time.[11] The efficiency of laser wakefield acceleration might be improved by this scheme. Another example of spatiotemporal effects is "wavefront rotation." This effect was used to isolate low-energy x-ray attosecond pulses.[12]

High-power lasers can generate secondary light sources/particles that can be used in medical, industrial, security, and pure scientific research, but they are less efficient than other alternatives because of their low repetition rate. To increase the repetition rate, the heat accumulation problem of the main amplifiers and the pump laser amplifiers must be solved (not for parametric amplifiers). For thin-disk Yb:YAG crystals used in pump lasers, a laser beam can be shined on one side of the disk and a cooling system can be attached to the other side to remove heat. Since the thickness is much thinner than the width, thermal gradients are formed only in the direction perpendicular to the surface, so that the lens effect of heat and polarization mixing is minimized. The thin-disk laser is used as a pump laser for the L1 optical parametric chirped-pulse–amplification laser at the ELI Beamlines Facility; it is aimed to supply pulses of 20 fs, 100 mJ at 1 kHz (Ref. 13). In large-scale petawatt lasers, the amplifier is stacked with several slabs and then cooled between the slabs by using room-temperature or low-temperature helium gas or water. The team at Lawrence Livermore National Laboratory has successfully constructed a 3.3-Hz petawatt laser based on this scheme [High-Repetition-Rate Advanced Petawatt Laser System (HAPLS)].[14]

Damage risk in the compressor remains the biggest concern for CPA. This risk is highest at the fourth grating, where the pulse is the shortest, because the damage threshold is lowered as the pulse becomes shorter. A multilayer dielectric grating was introduced to improve the damage threshold.[15] The uppermost layer is an etched dielectric grating, and a dielectric layer of high and low refractive indexes is repeatedly stacked under it for high reflectance. The damage threshold is improved by a factor of 10 (1 J/cm^2) compared to gold gratings, but the available bandwidth is narrow. To increase the bandwidth, a metal–dielectric grating has been considered with a dielectric top layer structure and metal layer at the bottom.[16] The thermal loading on gratings at a high repetition is another challenge.

We discuss applications in laser eye surgery and electron acceleration. Femotosecond lasers have been successfully used to cut out cornea flap in refractive surgery.[17] Femotosecond pulses provide better-controlled damage threshold. In electron acceleration, when a strong laser pulse focus passes through a plasma, the electrons are pushed out from focus by ponderomotive forces and a wakefield is formed in the ion density. When the electron is injected into the low potential of the ion wakefield, it moves with the wake as the pulse continues. Since this process occurs very quickly, the electrons accelerate to high energy. Lawrence Berkeley National Laboratory demonstrated 4.2 GeV using a microdischarge tube on the BELLA laser.[18]

CPA has revolutionized laser technology but it is also important to keep inventing new methods. For example, to overcome energy limitations, research is underway to amplify pulses using the Raman amplification phenomenon in a medium of plasma state.[19] In addition, efforts are being made to improve the system using new optical fibers and metamaterials. CPA opened the way for studying exciting advanced science in small laboratories. More commercialized petawatt lasers are becoming available in large laboratories and medical/industrial facilities.

This material is based upon work supported by the Department of Energy National Nuclear Security Administration under Award Number DE-NA0003856, the University of Rochester, and the New York State Energy Research and Development Authority.

1. D. Strickland and G. Mourou, Opt. Commun. **56**, 219 (1985).
2. E. B. Treacy, IEEE J. Quantum Electron. **QE-5**, 454 (1969).
3. J. Qiao *et al*., Opt. Express **15**, 9562 (2007).
4. J. Néauport *et al*., Appl. Opt. **46**, 1568 (2007).
5. O. E. Martinez, IEEE J. Quantum Electron. **QE-23**, 59 (1987).
6. G. Chériaux *et al*., Opt. Lett. **21**, 414 (1996).
7. L. Xu *et al*., Opt. Lett. **38**, 4837 (2013).
8. K. Ogawa *et al*., Opt. Express **17**, 7744 (2009).
9. N. Lefaudeux *et al*., Proc. SPIE **8600**, 86000W (2013).
10. P. Tournois, Opt. Commun. **140**, 245 (1997).
11. J. P. Palastro *et al*., Phys. Rev. A **97**, 033835 (2018).
12. F. Silva *et al*., Nat. Commun. **6**, 6611 (2015).
13. P. Bakule *et al*., Proc. SPIE **10241**, 102410U (2017).
14. T. M. Spinka and C. Haefner, Opt. Photonics News **28**, 26 (2017).
15. M. D. Perry *et al*., Opt. Lett. **20**, 940 (1995).
16. F. Canova *et al*., Opt. Express **15**, 15324 (2007).
17. T. Juhasz *et al*., Proc. SPIE **4633**, 1 (2002).
18. W. Leemans, Phys. Today **62**, 44 (2009).
19. V. M. Malkin, G. Shvets, and N. J. Fisch, Phys. Rev. Lett. **82**, 4448 (1999).

Measurements of Heat Flow from Surface Defects in Lithium Triborate

D. Broege and J. Bromage

Laboratory for Laser Energetics, University of Rochester

With laser sources being pushed to larger bandwidths and higher average powers every day, the importance of thermal effects in nonlinear optics has become an increasingly important area of study. It has been shown that absorption in the bulk of crystals, as well as their coatings, can lead to significant changes in temperature that can have a negative impact on nonlinear processes. One common but often overlooked source of heat in optics exposed to high average powers is the more-localized type, which can be the result of crystal defects, contamination, or damage spots. We have performed what is to our knowledge the first interferometric measurements of temperature distributions in a nonlinear optic resulting from absorption in a localized defect. A supporting analytical model is shown to elucidate features of the resulting temperature distribution and assist in estimating the total absorbed power at the site, with a sensitivity of one part in 10^5. This technique also provides a method of measuring absorption from a defect without the need for collection and measurement of a transmitted beam.

The setup used to perform these measurements consisted of a Mach–Zehnder interferometer with the sample in one arm. A 1064-nm kilowatt beam with a diameter of 2 mm was passed through the sample at a slight angle to induce heating. Changes in optical path length were measured across the face of the crystal, and a differential measurement was made between path lengths under ambient conditions and when the heated crystal reached equilibrium. These values were then used to calculate the corresponding longitudinally integrated temperature change with published material parameters.

The materials used in this study were all uncoated low-bulk-absorption lithium triborate (LBO) crystals, principally cut into 1-cm cubes and polished on four sides. This allowed for pump and probe beams to sample single crystallographic axes. This was used to qualify the measurements, in that a particular heat distribution could be probed with two separate polarizations, yielding two similar signals, but with different amplitudes. The ratio of these amplitudes could be calculated from material parameters and were shown to agree with measured values to within ~10%. The localized absorbers—the focus of our study—were single unintentionally produced damage spots on the crystal surfaces.

The 2-D changes in optical path length that were measured from these crystals showed a distinctive shape. It consisted of a sharp central peak, no larger than 100 μm, with rapidly decaying amplitude moving outward from the source. This stands in stark contrast to the more Gaussian-like distributions seen when heating is the result of absorption in the bulk or in a coating. Thermal imaging measurements showed that the heating occurred on only one face of the crystal, indicating that it was solely the result of localized absorption. Also observable was an asymmetry in the vertical direction, but not the horizontal, indicating that the crystal was warmer at the top surface than at the bottom, which was the result of heat loss into the mount.

With access to finite element analysis tools, calculations of heat flow can be made, but the higher resolutions required to accurately model such a small source require significant memory. We instead employed an analytical model that can be easily derived by relating the total absorbed power to heat flow through a spherical surface at distance r from the absorber through Fourier's law. This results in a temperature distribution of the following form for all points outside the absorber:

$$T(r) = \frac{P}{4\pi\kappa r} \tag{1}$$

and can be shown to be

$$T(r) = \frac{-Pr^2}{8\pi\kappa R^3} + \frac{3P}{8\pi\kappa R} \tag{2}$$

for all points inside the absorber, where r is the observation radius, κ is the thermal conductivity, R is the radius of the absorber, and P is the total absorbed power. For this model to be valid, the source must be small compared to the length of the crystal, and the heat flow through the crystal must be large compared to convective cooling at the surface.

What is immediately evident from the functional form of this distribution is that outside the absorber, its amplitude is proportional to the absorbed power, but completely insensitive to the size of the absorber. Calculations show that a 20-fold decrease in the size of the heat source results in only a factor-of-2 increase in the resulting peak temperature. *This implies that without detailed knowledge of the morphology of the absorber, a decent estimate can be made of the total power absorbed*. Figure 1 shows an overlay of measured changes in optical path length and a simulated data set using the simple model, with an absorbed power of 15.5 mW. The matching between the two is sensitive to the mW level, allowing for a very sensitive estimation of absorbed power at a localized defect. With this knowledge, one can use microscopy to determine the maximum spatial extent of the defect and determine a range of possible absorbances and sizes. In the case of our test spot, with a maximum possible size of 100 μm, assuming absorption is uniform across its face results in an average absorbance of 5%. If, on the other hand, absorbance is 100%, the size of the spot can be no smaller than 22 μm.

This material is based upon work supported by the Department of Energy National Nuclear Security Administration under Award Number DE-NA0003856, the University of Rochester, and the New York State Energy Research and Development Authority.

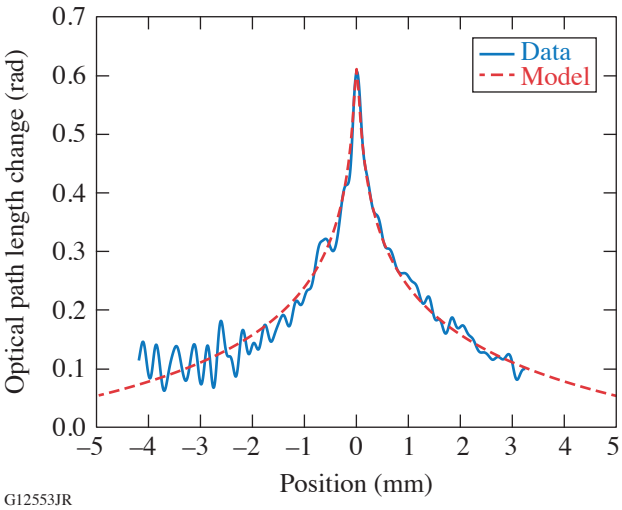

Figure 1
Comparison of measured optical path length change in LBO with an analytical model for 15.5 mW. This model was used along with interferometric measurements of temperature to estimate power absorbed at a localized spot with a sensitivity of one part in 10^5.

The Role of Urbach-Tail Optical Absorption on Subpicosecond Laser-Induced Damage Threshold at 1053 nm in Hafnia and Silica Monolayers

M. Chorel,[1] T. Lanternier,[1] É. Lavastre,[1] L. Lamaignère,[1] N. Roquin,[1] J. Néauport,[1] S. Papernov,[2] A. A. Kozlov,[2] B. N. Hoffman,[2] J. B. Oliver,[2] and S. G. Demos[2]

[1]Commissariat à l'Energie Atomique et aux Energies Alternatives, Centre d'Etudes Scientifiques et Techniques d'Aquitaine, France
[2]Laboratory for Laser Energetics, University of Rochester

Hafnia and silica are widely used as the principal materials in multilayer dielectric (MLD) mirrors for petawatt-class laser facilities such as the OMEGA EP Laser System at LLE. Damage initiation in such dielectric coatings under excitation with pulses shorter than about 2.5 ps is associated with the formation of plasma that facilitates, via a complex energy deposition process, superheating of the affected volume.[1] Assuming a crystalline material, the buildup of the electron density in the conduction band originates with multiphoton excitation between the ground state and conduction band. However, the layers in MLD coatings are generally amorphous with a structure that varies based on the deposition method. Consequently, the optical absorption edge properties can be characterized by an optical gap that most often is analyzed using two methods. At photon energies above the optical gap, the absorption (α) behaves according to the Tauc formula, i.e., $\alpha\hbar\omega \propto (\hbar\omega - E_T)^2$, where E_T is known as the *Tauc gap*. Below the optical gap, the absorption is described by the Urbach tail[2] that arises from localized states in the band gap. In addition, defect states can further extend the absorption edge toward lower energies. As a result, transitions from the ground state to the conduction band are not limited to intraband transitions but include additional pathways through intermediate states at the Urbach tail and defects. It has been previously discussed that red shifting of the Urbach tail can lead to a reduced damage threshold in silica.[3] The role of defects in decreasing the damage threshold has also been documented in various materials including hafnia monolayers.[4]

The optical gap and Urbach tail are in the 200- to 350-nm spectral region for both silica and hafnia layers. Based on the above considerations, this work explores the relationship of the laser-induced–damage threshold (LIDT) (using 1053-nm, 800-fs laser pulses) of silica and hafnia layers obtained by different vendors, using different deposition methods, to the characteristics of the Urbach tail in each material. The damage threshold is estimated following normalization for the electric-field distribution within each layer and is typically referred to as the "intrinsic" LIDT.[5] The damage thresholds are investigated as a function of the estimated optical gap (Tauc gap) of each material and further evaluated as a function of the red-shifted Urbach tail absorption. Analysis of the absorption-edge characteristics is performed via (a) spectroscopic analysis in the UV spectral region and (b) photothermal absorption imaging using 355-nm excitation.

The results suggest that although the fabrication process has a large influence on the intrinsic LIDT, it only marginally affects the estimated optical gap energy. The samples (both silica and hafnia) that exhibit the highest intrinsic LIDT also exhibit the lowest absorption in the three- to five-photon absorption spectral range (≈200 to 350 nm), while the lowest LIDT samples exhibit the highest absorption. This trend was quantified in Figs. 1(a) and 1(b) by plotting the absorption coefficient as a function of the intrinsic LIDT for monolayers of hafnia at 351 nm and silica at 266 nm. The choice of the wavelength is based on using a threshold absorption coefficient value of the order of 10^3 cm^{-1}. These results suggest the presence of a correlation between the absorption at the Urbach tail to the intrinsic LIDT at 1053 nm using 800-fs pulses.

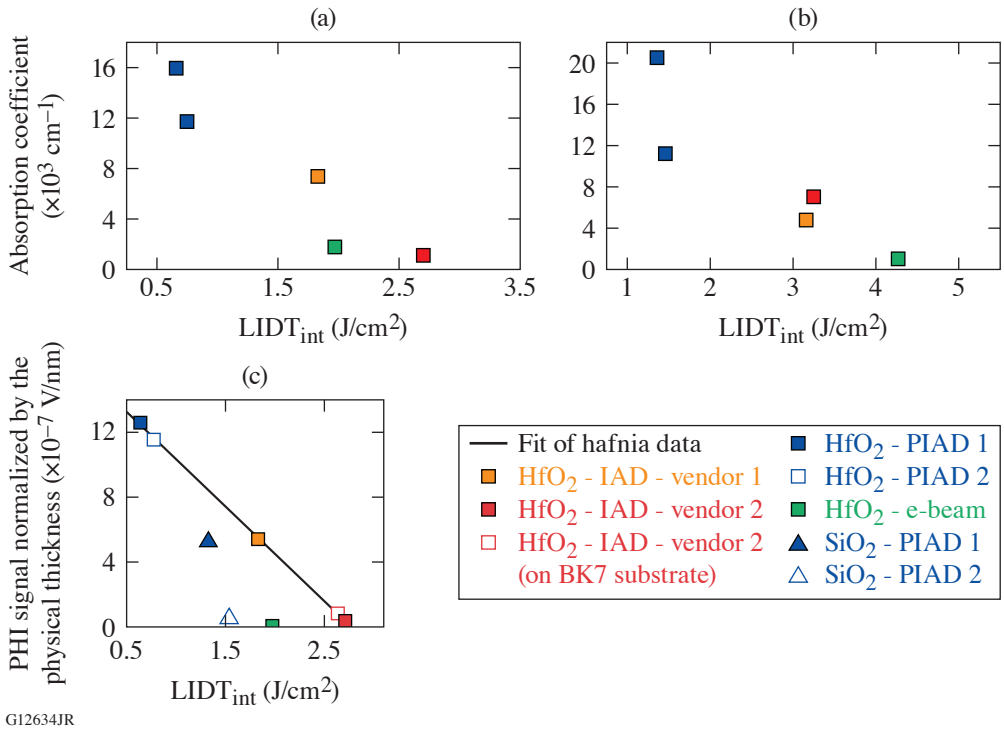

Figure 1
The absorption coefficient of (a) hafnia monolayers at 351 nm and (b) silica monolayers at 266 nm as a function of their intrinsic LIDT. (c) Photothermal heterodyne imaging (PHI) signal at 355 nm normalized by the physical thickness as a function of the intrinsic LIDT for hafnia (squares) and silica (triangles) samples.

The absorption in the UV spectral range was also probed using a photothermal heterodyne imaging system. This technique is based on a pump–probe approach and utilized a 355-nm pump beam to probe the local absorption with spatial resolution of the order of 500 nm. For each sample, several intensity maps were acquired by raster scanning, and an average value of every map for each sample was calculated. The photothermal absorption was normalized by the physical thickness of the layer. The results displayed in Fig. 1(c) demonstrate a direct relationship of the LIDT to the strength of the photothermal absorption signal.

This material is based upon work supported by the Department of Energy National Nuclear Security Administration under Award Number DE-NA0003856, the University of Rochester, and the New York State Energy Research and Development Authority.

1. A. A. Kozlov *et al.*, Sci. Rep. **9**, 607 (2019).
2. F. Urbach, Phys. Rev. **92**, 1324 (1953).
3. B. Sadigh *et al.*, Phys. Rev. Lett. **106**, 027401 (2011).
4. S. Papernov *et al.*, Opt. Express **26**, 17,608 (2018)
5. A. Hervy *et al.*, Opt. Eng. **56**, 011001 (2016).

Measurement of the Angular Dependence of Spontaneous Raman Scattering in Anisotropic Crystalline Materials Using Spherical Samples: Potassium Dihydrogen Phosphate as a Case Example

T. Z. Kosc, A. Maltsev, and S. G. Demos

Laboratory for Laser Energetics, University of Rochester

A new and flexible experimental configuration has been developed and tested to measure the spontaneous Raman scattering for samples with any crystal cut, probed with any specific pump polarization, and for which the scatter signal in any direction and with any polarization can be measured. This experimental requirement stems from the challenges, arising from the complexity of light propagation, in obtaining accurate measurements of the angular dependence of the Raman scattering cross section in birefringent materials. The nonlinear optical material KH_2PO_4 (KDP) is used as the model medium. This study is motivated by the need to improve our understanding and management of transverse stimulated Raman scattering (TSRS) in KDP crystals typically used for frequency conversion and polarization control in large-aperture laser systems. Key to this experimental platform is the use of high-quality spherical samples that enable one to measure the Raman scattering cross section in a wide range of geometries using a single sample. The system demonstrated in this work is designed to enable experiments to (1) develop a better understanding of the Raman polarizability tensor and (2) directly measure the angular dependence of the spontaneous Raman scattering in a crystal cut suitable for polarization control.

The spontaneous Raman scattering is an experimentally measureable quantity from which the Raman polarizability tensor of vibrational modes of interest can be established using the theoretically expected formulation based on symmetry as a guide.[1] Given this tensor, the Raman-scattering cross section can be estimated at any orientation and the corresponding TSRS gain coefficient can be calculated. Efforts to develop an empirical description of the Raman tensor has provided an approximation for the off-diagonal elements, but its precise form remains incomplete,[2] while measurements for the Raman scattering cross section are limited.[3] An accurate Raman polarizability tensor would enable (1) the modeling of TSRS for multiple crystal-cut configurations to guide the design of KDP-based optical elements that provide minimum SRS gain, (2) the estimation of material limits in inertial confinement fusion laser designs, and (3) the optimization of hardware designs and operational conditions.

Based on the consideration discussed above, we developed an experimental Raman scattering spectroscopy system (Fig. 1) that uses spherical crystal (KDP) samples and facilitates the measurement of the angular dependence of the spontaneous Raman scattering cross section in directions orthogonal to beam propagation for any specific crystal orientation of interest. The optic axis of the sample sphere is oriented by two programmable rotation stages. Custom vacuum chucks, installed in the open aperture of the rotation stages, are used to "hold" the sphere and rotate it. Any position on the sphere (4π steradians) can be reached with a combination of, at most, three stage moves. Linear stages provide additional vertical and horizontal alignment capabilities in the x–y plane to overlap the sphere center and the excitation laser beam focus with the focal point of the signal collection optics.

The Raman scattering intensity of the totally symmetric mode (914 cm^{-1}) integrated over 100 cm^{-1} about the peak (860 to 960 cm^{-1}) as a function of the azimuthal angle ϕ is shown in the results presented in Fig. 2. The optic axis (OA) was aligned in the azimuthal (horizontal) plane, and for $\phi = 0°$, the OA was oriented along the laboratory z axis (beam propagation direction). Four combinations of polarization of the excitation laser and the analyzer were used, with the excitation polarization parallel to the laboratory x or y axis and the analyzer parallel to the laboratory z or y axis. Accordingly, the inset in Fig. 2 describes the ini-

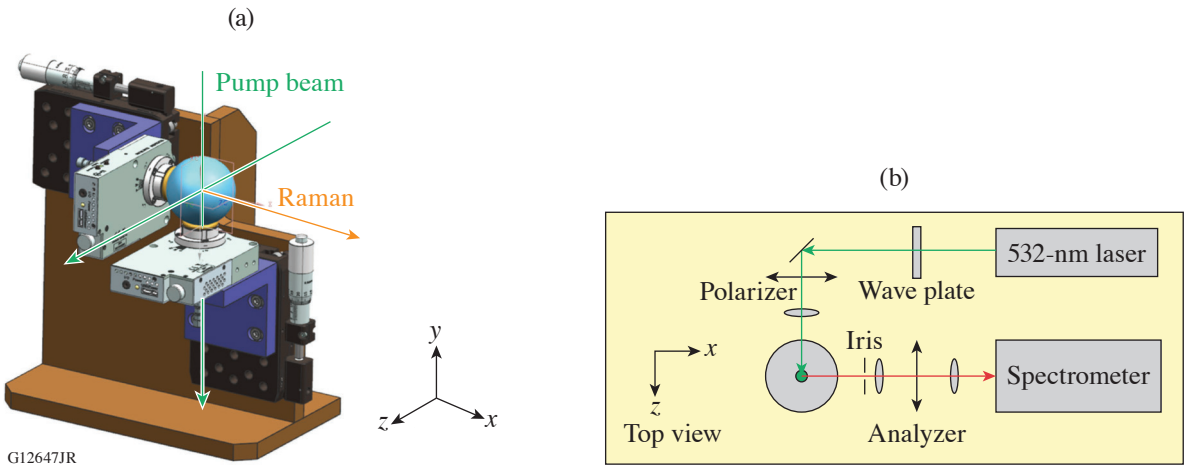

Figure 1
Schematic depiction of (a) the sample holder and (b) the Raman scattering spectroscopy system utilizing high-quality spherical samples to measure the Raman scattering signal orthogonal to the laser excitation beam. The excitation beam propagates along the horizontal laboratory z axis, while the Raman signal was measured at an orthogonal direction along the horizontal laboratory x axis.

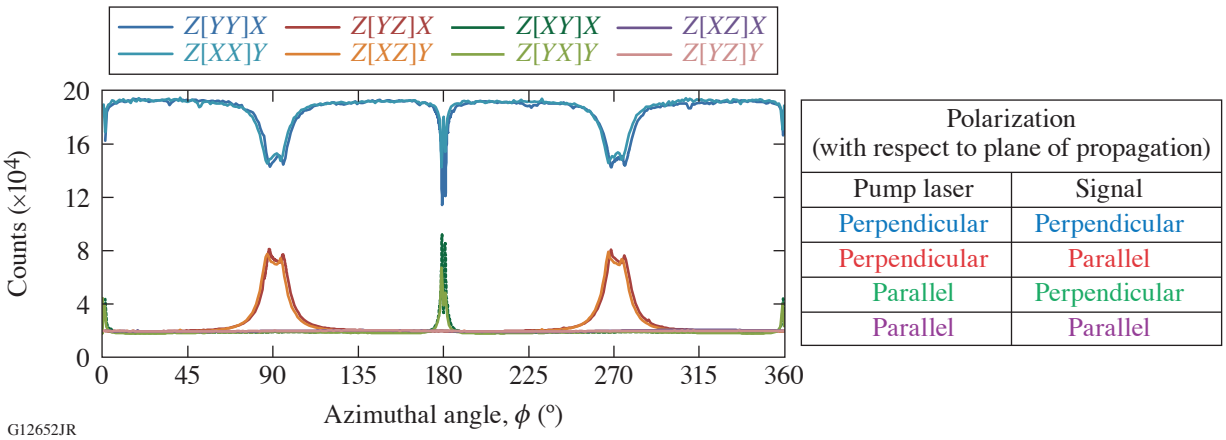

Polarization (with respect to plane of propagation)	
Pump laser	Signal
Perpendicular	Perpendicular
Perpendicular	Parallel
Parallel	Perpendicular
Parallel	Parallel

Figure 2
The integrated spontaneous Raman scattering signal of the totally symmetric internal PO_4 mode is measured as a function of the azimuthal angle for four different initial configurations, which are given in the legend and follow Porto notation. The letters to the left and right of the brackets define the propagation direction of the incident and scattered light; the letters inside the brackets, left to right, are the polarization of the incident and scattered light. Additional information on measurement geometry is provided in the table.

tial setting of the Raman scattering measurement in the Porto notation.[4] The notation in the legend of Fig. 2 refers to the crystal axes (X, Y, Z) at the initial position $\phi = 0°$. Measurements were performed with the Raman signal initially measured along the X crystal axis and then after rotating the sample by 90° about the Z crystal axis to measure the Raman signal along the Y crystal axis (X or Y directions are indistinguishable during measurement and therefore arbitrarily assigned). Consequently, eight different measurements were performed with the above-described initial alignment conditions.

The blue traces in Fig. 2 represent data acquired when both the excitation and signal polarizations were perpendicular to the (horizontal) plane of propagation. Wide double valleys are found at $\phi = 90°$ and 270°, while narrow double valleys are found at $\phi = 0°$ and 180°. An inverse set (red trace) of wide (only) double peaks is seen when the excitation laser is perpendicularly

polarized. The presence of narrow double peaks (green trace) requires a parallel polarized excitation laser, but perpendicularly polarized Raman signal. The Raman signal is very low when both the excitation and the signal polarizations are parallel to the plane of propagation. Data sets were nearly indistinguishable when the sphere was rotated 90° about the optics axis to interchange to crystal *X* and *Y* axes.

The data acquired using a 30-mm polished KDP crystal in this new experimental configuration demonstrate that a more-precise measure of the Raman tensor can now be performed. This system was designed to help improve predictive capabilities in order to minimize TSRS-induced effects in large-aperture laser systems by enabling direct measurement to obtain information regarding the optimal crystal cut and crystal mounting configuration.

This material is based upon work supported by the Department of Energy National Nuclear Security Administration under Award Number DE-NA0003856, the University of Rochester, and the New York State Energy Research and Development Authority.

1. R. Loudon, Adv. Phys. **13**, 423 (1964).
2. W. L. Smith, M. A. Henesian, and F. P. Milanovich, "Spontaneous and Stimulated Raman Scattering in KDP and Index-Matching Fluids," 1983 Laser Program Annual Report, pp. 6-61– 6-69, Lawrence Livermore National Laboratory, Livermore, CA, UCRL-500.21-83 (1984).
3. S. G. Demos *et al.*, Opt. Exp. **19**, 21050 (2011).
4. T. C. Damen, S. P. S. Porto, and B. Tell, Phys. Rev. **142**, 570 (1966).

Comparison of Shadowgraphy and X-Ray Phase-Contrast Methods for Characterizing a DT Ice Layer in an Inertial Confinement Fusion Target

D. R. Harding, M. D. Wittman, N. Redden, D. H. Edgell, and J. Ulreich

Laboratory for Laser Energetics, University of Rochester

Shadowgraphy and x-ray phase-contrast (XPC) imaging are two techniques that are used to characterize the deuterium–tritium (DT) ice layer in inertial confinement fusion targets. Each technique has limitations that affect how accurately they can characterize small crystalline defects and measure ice-thickness nonuniformities that may be only a few micrometers in height. The purpose of this study is to determine if shadowgraphy is overly sensitive to the size of defects at the ice surface and insufficiently sensitive to the shape of longer-wavelength roughness, and if XPC is too insensitive to defects at the ice's inner surface.

Multiple ice layers with different thicknesses (40 to 63 μm), thickness uniformities (peak-to-valley variations that range from <2 to 12 μm), and crystal defects were analyzed using shadowgraphy and XPC techniques. The inability to rotate the target so that the same region of the ice layer was imaged by each method limited how extensively the two techniques could be compared; however, the relative accuracy of each technique for measuring the size of the perturbation to the ice near the fill tube could be compared because the thermal profile (and therefore the low-mode ice thickness distribution) around the target is axisymmetric around the fill-tube axis: crystal defects that intersected the fields of view of both techniques could also be compared. Results from each technique agreed when the ice layer was uniformly thick and the crystal lacked defects. That agreement worsened as the number of defects at the surface of the ice layer increased or as the perturbation to the ice layer at the fill tube increased. Shadowgraphy is very sensitive to identifying defects in the crystal, and the size of those defects was consistently larger than the size reported by XPC and unlikely to be physically possible since β-heating is expected to smoothen them. Large defects, such as features that typically occur at each end of the *c* axis of the DT crystal, were measured using both techniques.

The dimensions of the ice layer near the fill tube that was thicker (or thinner) than elsewhere were reported by shadowgraphy to be smaller in height and area than by XPC. This is shown in the ice-thickness measurement of a 2-D slice through the target (Fig. 1). XPC analysis reported the ice layer to have a shape with the majority of the spectral power in low modes, which is expected for a thermal nonuniformity induced by the fill tube; shadowgraphic analysis of the ice layer showed the profile at the fill tube to be smaller in height and width. Two separate shadowgraphic analyses that use caustics to trace different paths through the target and, in theory, image the same ice/vapor surface, did not consistently report the ice perturbations to have the same size or shape. The XPC method, in theory and from the consistency of the experimental results, provided the best assessment of low-mode ($\ell < 7$) roughness in ice layers, and the shadowgraphy method using the brightest caustic provided the best method for detecting the presence of grooves in the ice, although not for quantifying the size of them. Caution: If multiple grooves are present, the analysis can be ambiguous and it is best to melt and reform the ice layer.

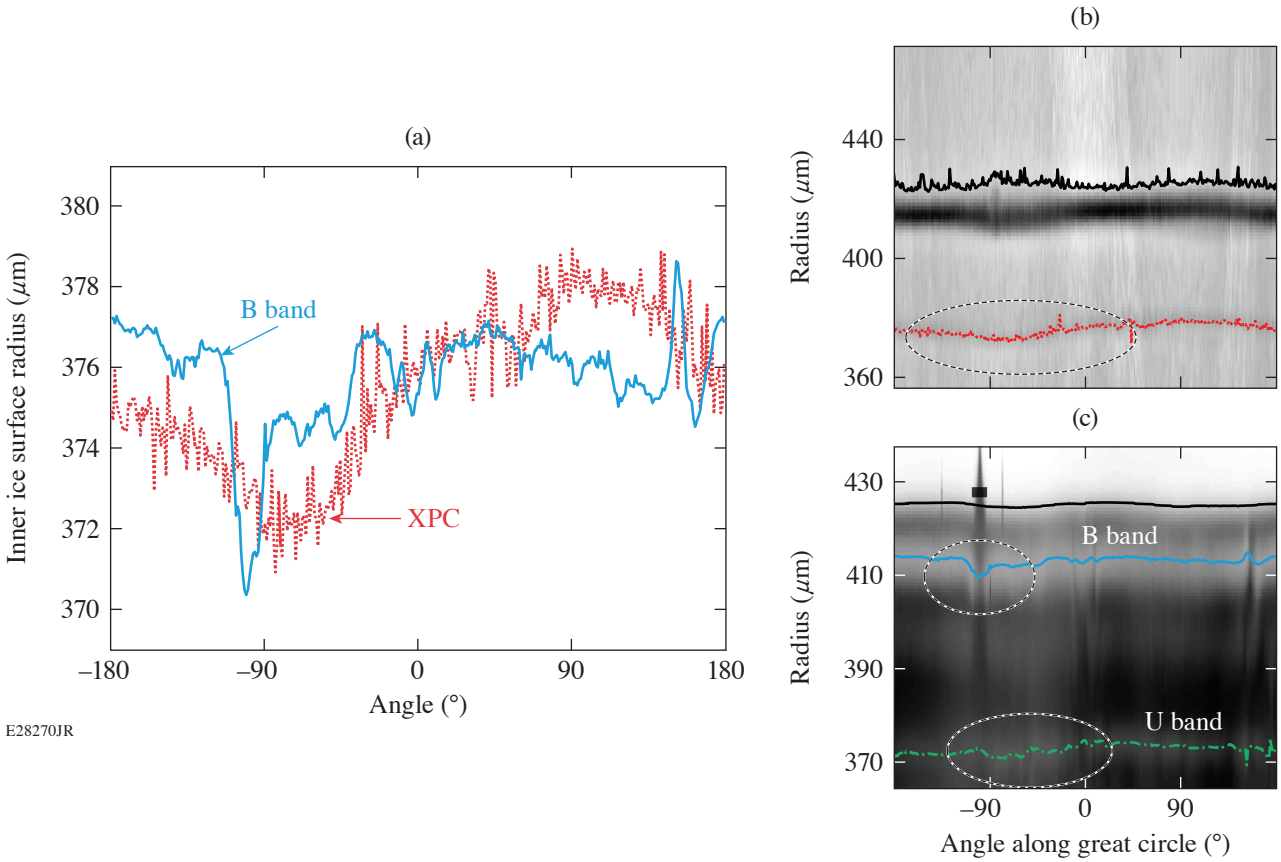

Figure 1
(a) Unwrapped ice/vapor interfaces characterized by shadowgraphy (B band) and XPC analysis are superimposed over each other to demonstrate the effect of the fill tube on the thickness uniformity of the ice layer. The 41-μm-thick ice layer is reported to have a larger and wider perturbed region (circled) in (b) the XPC image and analysis than in (c) either of the (circled) B- and U-band analyses (solid blue line and dashed green line, respectively). The fill tube is located at –90°.

This material is based upon work supported by the Department of Energy National Nuclear Security Administration under Award Number DE-NA0003856, the University of Rochester, and the New York State Energy Research and Development Authority.

Prediction of Deuterium–Tritium Ice-Layer Uniformity in Direct-Drive Inertial Confinement Fusion Target Capsules

B. S. Rice,[1] J. Ulreich,[2] and M. J. Shoup III[2]

[1]Rochester Institute of Technology
[2]Laboratory for Laser Energetics, University of Rochester

High-yield inertial confinement fusion targets require that the uniformity of the DT ice layer be less than 1-μm rms (Ref. 1). The uniformity of the ice layer (i.e., the solid/gas phase boundary) is affected by the surrounding helium environment and the structure that supports the target. To aid the designer of target support structures, the sensitivity of ice-layer uniformity to support structure thermal conductivity and a 3-mW heat source in the surrounding helium are studied using computational fluid dynamic simulations.

Figure 1 shows the detailed geometry used for the multiphase conjugate heat-transfer numerical model. The environment around the target and target support consists of low-pressure (2-Torr) helium gas that carries the heat produced by tritium beta decay to a surrounding copper shroud, which is connected to the cryocooler.

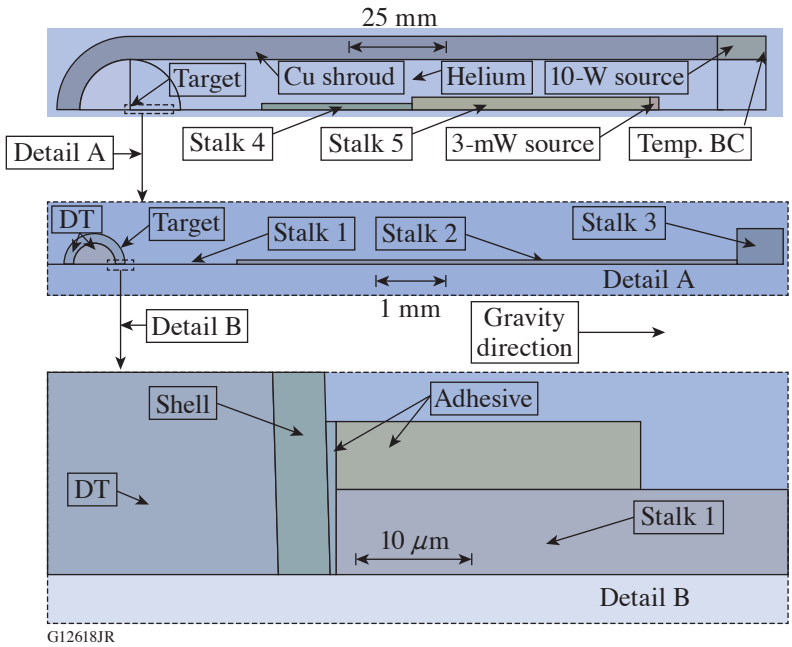

Figure 1
Model geometry detail. Temp. BC: temperature boundary condition.

Figure 2 shows one of the meshes used. The outer portion of DT closest to the target capsule uses an element size of ~5 × 5 μm to resolve the gas/ice phase boundary. Elements representing the 17-μm SiC support, target capsule shell, and adhesive are also ~5 × 5 μm in size. Other areas of the model use a coarser mesh for a more-efficient solution. Based on a mesh refinement study, the results presented are mesh independent. Sensitivities to various parameters were studied with this model.

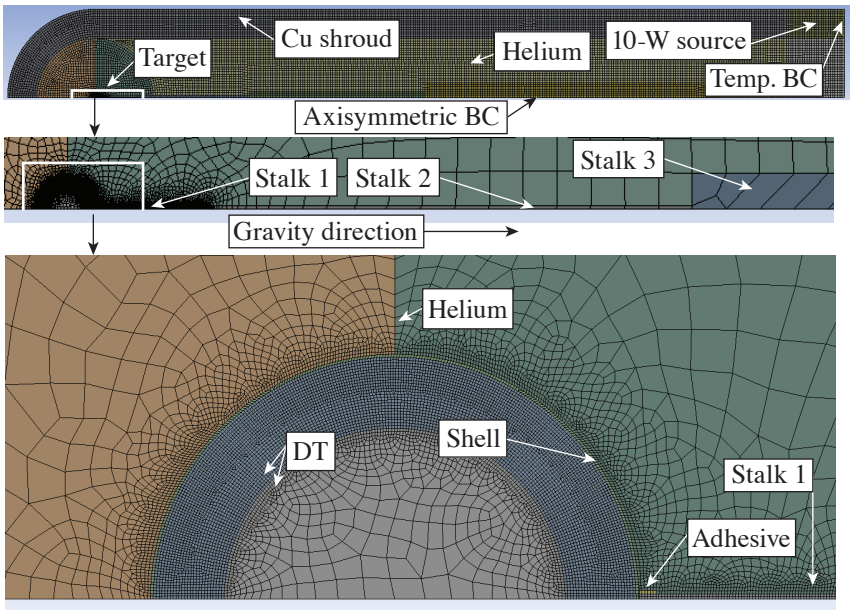

Figure 2
Model of mesh detail.

Experimental data of DT ice-layer uniformity were used to validate several of the multiphase conjugate heat-transfer numerical simulations. Based on experiment results and/or numerical simulations, the following conclusions were made:

- When heat sources are present in the helium environment, it is advantageous for the lower portion of the support structure to have a thermal conductivity of less than ~2 W/m/K.
- For the temperature variations and helium pressures studied, multiphase conjugate heat-transfer ice-layer models yield the same results as multiphase conduction-only models.
- The thermal conductivity of the fiber directly touching the target capsule must be a close match to helium thermal conductivity (0.026 W/m/K) to produce uniform ice layers.
- High target-shell thermal conductivity (~27 W/m/K) mitigates locally thick ice near a highly conductive (~1.5-W/m/K) support stalk.

This material is based upon work supported by the Department of Energy National Nuclear Security Administration under Award Number DE-NA0003856, the University of Rochester, and the New York State Energy Research and Development Authority.

1. S. X. Hu *et al.*, Phys. Plasmas **17**, 102706 (2010).

Developing a Curriculum for the Translation of Microscopy with Ultraviolet Surface Excitation (MUSE) into a High School Science Classroom

K. Kopp and S. G. Demos

Laboratory for Laser Energetics, University of Rochester

The translation of microscopy with ultraviolet surface excitation (MUSE) into a high school science classroom is investigated with the goal of providing a suitable new modality to enhance life science education. A key part of this effort is the development of laboratory exercises that can integrate the advanced capabilities of MUSE into a classroom setting. We consider that MUSE in education can eliminate the need for premade microscope slides and provide a far more engaging and rewarding experience for students.

MUSE is a new microscope technology originally developed to locate defects in optical materials that were responsible for introducing laser-induced damage in optical materials for large-aperture laser systems such as OMEGA. This method is based on the salient property of UV light at wavelengths between 250 and 285 nm to propagate into only the top 10 μm of a tissue specimen, illuminating only the top cell layer.[1–3] The resulting fluorescence images, arising from either the native tissue fluorophores or extrinsic contrast agents, are also localized within this narrow range. This enables one, with proper selection of imaging optics, to acquire high-quality images without implementing any additional optical sectioning method (such as confocal imaging) or physical sectioning of the specimen into very thin layers. In addition, UV light can photoexcite a wide range of common fluorescing stains, which subsequently emit light typically in the visible spectrum.[2,3]

Tissues produce autofluorescence when exposed to any form of photoexcitation, but UV light causes a relatively larger amount of autofluorescence, typically dominated by the emission by tryptophan.[1] MUSE imaging relies on the visible structural differentiation caused by either the nonuniform cellular distribution of naturally occurring biomolecules or the use of fluorescing stains to highlight different cellular compartments. This allows one to image the cellular organization and microstructure without laborious effort (fix, dehydrate, embed in wax, cut, and stain) to produce a thin stained section. In this work, tissue samples were stained using Hoechst 33342 and Eosin Y, which stain the nuclei and cytoplasm, respectively, and are safe for classroom handling and use.[4] Premixed powders in a gelatin capsule have been made with 20 g of Eosin Y and 5 g of Hoechst 33342, and the capsule is readily soluble in 100 mL of de-ionized water, resulting in a stain solution that is plenty for a single class. The goal of this work was to develop a curriculum involving MUSE that can be adapted to life science education. To do this, laboratory exercises for a high school science class were created to enhance student interest with a personalized learning approach.

A MUSE imaging setup was configured similar to that described in Ref. 4. In short, the UV LED illumination is at an oblique angle and focused on the sample directly under the 10× objective. This system was used to view plant and animal microanatomy with a quick, simple, and inexpensive process. This system was also used to image tissues without any preparation, as well as stained tissue samples. Imaging experiments of various objects, plants, and animal tissues were performed toward (a) exploring the spectrum of MUSE imaging suitable for an education setting and (b) developing laboratory experiments relevant to the high school science classroom. Laboratory procedures, background, and examples were written for each experiment. These exercises utilize MUSE technology while complementing the current life science curriculum standards. The labs bring a personalized learning approach to obtaining high-quality images of tissue microstructure that reinforce material learned through classwork. The developed MUSE curriculum focuses on exposing high school students to scientific practices that reinforce their knowledge

about life science. Each practice learned through the laboratory exercises is relevant to the public high school life science standards, and the coordinating Next Generation science standard is referenced.[5]

The first practice that this curriculum emphasizes is the identification of major structures in plant samples. Students can view organisms such as leaves (see Fig. 1), grass, and flowers under the microscope and use the resulting images to find certain microstructures, such as leaf veins. By looking at various cells and structures within one organism, students are learning about cellular specialization and organization. This practice reinforces Next Generation standards HS-LS1-1 and HS-LS1-2.

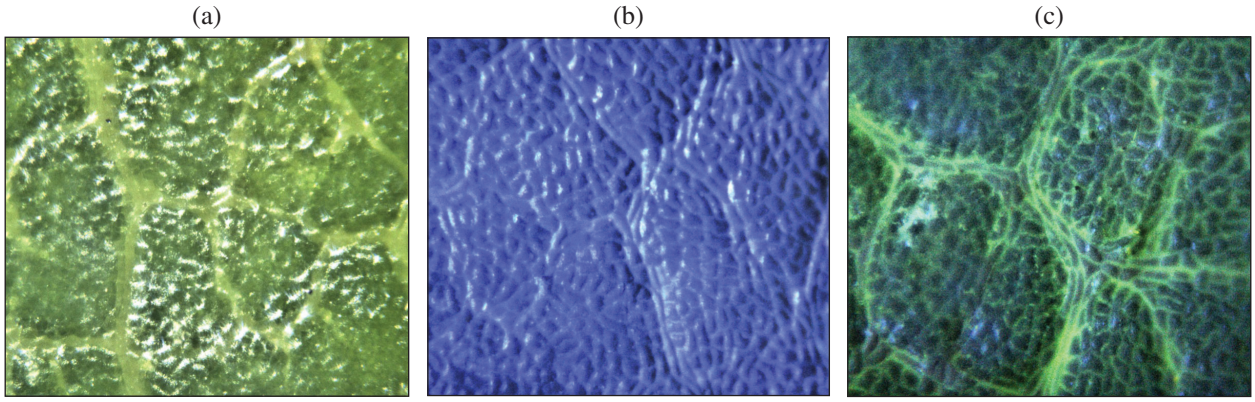

Figure 1
Images from the surface of a maple leaf: (a) conventional white-light illumination, (b) autofluorescent image, and (c) staining with Hoechst 33342 and Eosin Y.

The next scientific practice with which students are involved is the dissection of an organism to view gross anatomy as well as tissue microstructure. When students dissect an organism, they work to understand the hierarchical levels of organization within a multicellular organism. This corresponds to Next Generation standard HS-LS1-2. Students can identify organs and organ systems in an organism and then take a tissue sample to view the same organism's microanatomy at the cellular level.

The last emphasized practice is the comprehension of the structure and function of plant and animal cells. This practice works on a microscopic scale and focuses on life processes at the cellular level. Plant and animal cells have different organelles to perform different functions, and each organelle and cell has specific structures that relate to its function. The various cells work together to perform life processes to maintain homeostasis within an organism. This is shown in Next Generation standard HS-LS1-2.

Additional laboratory exercises can be developed to offer distinctive experiences to students such as experiments that enable one to monitor the dynamic response of cells and tissues to an external stimulus.

This material is based upon work supported by the Department of Energy National Nuclear Security Administration under Award Number DE-NA0003856, the University of Rochester, and the New York State Energy Research and Development Authority.

1. B. Lin *et al.*, Opt. Express **18**, 21,074 (2010).
2. R. M. Levenson *et al.*, Proc. SPIE **9703**, 97030J (2016).
3. F. Fereidouni *et al.*, Nat. Biomed. Eng. **1**, 957 (2017).
4. C. Z. R. Huang, R. W. Wood, and S. G. Demos, J. Biomed. Opt. **23**, 12,1603 (2018).
5. *Next Generation Science Standards: For States, by States*, The National Academies Press, Washington, DC (2013).

FY19 Q2 Laser Facility Report

J. Puth, M. Labuzeta, D. Canning, and L. J. Waxer

Laboratory for Laser Energetics, University of Rochester

During the second quarter (Q2) of FY19, the Omega Laser Facility conducted 380 target shots on OMEGA and 196 target shots on OMEGA EP for a total of 576 target shots (see Tables I and II). OMEGA averaged 12.2 target shots per operating day averaging 95.0% Availability and 96.2% Experimental Effectiveness.

Table I: OMEGA Laser System target shot summary for Q2 FY19.

Program	Laboratory	Planned Number of Target Shots	Actual Number of Target Shots
ICF	LLE	99	106
	LANL	11	8
	LLNL	33	35
ICF subtotal		143	149
HED	LLE	22	21
	LANL	44	46
	LLNL	27.5	30
HED subtotal		93.5	97
LBS		33	33
NLUF		22	25
LLE calibration	LLE	0	76
Grand total		291.5	380

Table II: OMEGA EP Laser System target shot summary for Q2 FY19.

Program	Laboratory	Planned Number of Target Shots	Actual Number of Target Shots
ICF	LLE	52.5	73
	LLNL	14	12
ICF subtotal		66.5	85
HED	LLE	21	29
	LLNL	28	38
	SNL	7	7
HED subtotal		56	74
LBS		21	26
LLE calibration	LLE	0	11
Grand total		143.5	196

OMEGA EP was operated extensively in Q2 FY19 for a variety of user experiments. OMEGA EP averaged 8.2 target shots per operating day averaging 93.6% Availability and 98.4% Experimental Effectiveness.

In Q2 FY19, the full-beam in-tank (FBIT) diagnostic was used to characterize the on-shot, on-target focal spot of five additional OMEGA beams, bringing the total to 11 beams characterized. Measurements included near fields and far fields. The far fields have been measured with and without distributed phase plates, smoothing by spectral dispersion, and distributed polarization rotators. The far-field data represent on-shot conditions during OMEGA cryogenic experiments. An additional 20 beams will be characterized during the remainder of FY19 and early FY20, providing a more-complete characterization of on-target laser uniformity.

Publications and Conference Presentations

Publications

H. Aluie, "Convolutions on the Sphere: Commutation with Differential Operators," Int. J. Geomath. **10**, 9 (2019).

S.-W. Bahk, "Current Status of Chirped–Pulse Amplification Technology and Its Applications," Phys. High Technol. **27**, 16 (2018).

K. A. Bauer, M. Heimbueger, S. Sampat, L. J. Waxer, E. C. Cost, J. H. Kelly, V. Kobilansky, J. Kwiatkowski, S. F. B. Morse, D. Nelson, D. Weiner, G. Weselak, and J. Zou, "Comparison of On-Shot, In-Tank, and Equivalent-Target-Plane Measurements of the OMEGA Laser System Focal Spot," Proc. SPIE **10898**, 108980G (2019).

I. A. Begishev, M. Romanofsky, S. Carey, R. Chapman, G. Brent, M. J. Shoup III, J. D. Zuegel, and J. Bromage, "High-Efficiency, Large-Aperture Fifth-Harmonic–Generation of 211-nm Pulses in Ammonium Dihydrogen Phosphate Crystals for Fusion Diagnostics," Proc. SPIE **10898**, 108980N (2019).

R. L. Berger, C. A. Thomas, K. L. Baker, D. T. Casey, C. S. Goyon, J. Park, N. Lemos, S. F. Khan, M. Hohenberger, J. L. Milovich, D. J. Strozzi, M. A. Belyaev, T. Chapman, and A. B. Langdon, "Stimulated Backscatter of Laser Light from BigFoot Hohlraums on the National Ignition Facility," Phys. Plasmas **26**, 012709 (2019).

W. A. Bittle, M. Bock, R. Boni, J. Kendrick, A. Sorce, and C. Sorce, "A Rate-Doubled 10-GHz Fiducial Comb Generator for Precision Optical Timing Calibration," Rev. Sci. Instrum. **90**, 035103 (2019).

J. Bromage, S.-W. Bahk, I. A. Begishev, C. Dorrer, M. J. Guardalben, B. N. Hoffman, J. B. Oliver, R. G. Roides, E. M. Schiesser, M. J. Shoup III, M. Spilatro, B. Webb, D. Weiner, and J. D. Zuegel, "Technology Development for Ultraintense All-OPCPA Systems," High Power Laser Sci. Eng. **7**, e4 (2019).

S. Chawla, M. Bailly-Grandvaux, H. S. McLean, P. K. Patel, M. S. Wei, and F. N. Beg, "Effect of Target Material on Relativistic Electron Beam Transport," Phys. Plasmas **26**, 033111 (2019).

A. R. Christopherson, R. Betti, and J. D. Lindl, "Thermonuclear Ignition and the Onset of Propagating Burn in Inertial Fusion Implosions," Phys. Rev. E **99**, 021201(R) (2019).

A. Colaïtis, J. P. Palastro, R. K. Follett, I. V. Igumenshchev, and V. Goncharov, "Real and Complex Valued Geometrical Optics Inverse Ray-Tracing for Inline Field Calculations," Phys. Plasmas **26**, 032301 (2019).

J. R. Davies, D. H. Barnak, R. Betti, E. M. Campbell, V. Yu. Glebov, E. C. Hansen, J. P. Knauer, J. L. Peebles, and A. B. Sefkow, "Inferring Fuel Areal Density from Secondary Neutron Yields in Laser-Driven Magnetized Liner Inertial Fusion," Phys. Plasmas **26**, 022706 (2019).

W. R. Donaldson and A. Consentino, "Co-Timing UV and IR Laser Pulses on the OMEGA EP Laser System," Proc. SPIE **10898**, 108980O (2019).

T. S. Duffy and R. F. Smith, "Ultra-High Pressure Dynamic Compression of Geological Materials," Front. Earth Sci. **7**, 23 (2019).

D. E. Fratanduono, M. Millot, A. Fernandez Pañella, P. A. Sterne, G. W. Collins, D. G. Hicks, J. H. Eggert, T. R. Boehly, and P. M. Celliers, "Measurement of the Sound Speed in Dense Fluid Deuterium Along the Cryogenic Liquid Hugoniot," Phys. Plasmas **26**, 012710 (2019).

J. A. Frenje, R. Florido, R. Mancini, T. Nagayama, P. E. Grabowski, H. Rinderknecht, H. Sio, A. Zylstra, M. Gatu Johnson, C. K. Li, F. H. Séguin, R. D. Petrasso, V. Yu. Glebov, and S. P. Regan, "Experimental Validation of Low-*Z* Ion-

Stopping Formalisms Around the Bragg Peak in High-Energy-Density Plasmas," Phys. Rev. Lett. **122**, 015002 (2019).

D. H. Froula, J. P. Palastro, D. Turnbull, A. Davies, L. Nguyen, A. Howard, D. Ramsey, P. Franke, S.-W. Bahk, I. A. Begishev, R. Boni, J. Bromage, S. Bucht, R. K. Follett, D. Haberberger, G. W. Jenkins, J. Katz, T. J. Kessler, J. L. Shaw, and J. Vieira, "Flying Focus: Spatial and Temporal Control of Intensity for Laser-Based Applications," Phys. Plasmas **26**, 032109 (2019) (invited).

L. Gao, E. Liang, Y. Lu, R. K. Follett, H. Sio, P. Tzeferacos, D. H. Froula, A. Birkel, C. K. Li, D. Lamb, R. Petrasso, W. Fu, M. Wei, and H. Ji, "Mega-Gauss Plasma Jet Creation Using a Ring of Laser Beams," Astrophys. J. Lett. **873**, L11 (2019).

M. Gatu Johnson, B. D. Appelbe, J. P. Chittenden, A. Crilly, J. Delettrez, C. Forrest, J. A. Frenje, V. Yu. Glebov, W. Grimble, B. M. Haines, I. V. Igumenshchev, R. Janezic, J. P. Knauer, B. Lahmann, F. J. Marshall, T. Michel, F. H. Séguin, C. Stoeckl, C. Walsh, A. B. Zylstra, and R. D. Petrasso, "Impact of Imposed Mode 2 Laser Drive Asymmetry on Inertial Confinement Fusion Implosions," Phys. Plasmas **26**, 012706 (2019).

V. Gopalaswamy, R. Betti, J. P. Knauer, N. Luciani, D. Patel, K. M. Woo, A. Bose, I. V. Igumenshchev, E. M. Campbell, K. S. Anderson, K. A. Bauer, M. J. Bonino, D. Cao, A. R. Christopherson, G. W. Collins, T. J. B. Collins, J. R. Davies, J. A. Delettrez, D. H. Edgell, R. Epstein, C. J. Forrest, D. H. Froula, V. Y. Glebov, V. N. Goncharov, D. R. Harding, S. X. Hu, D. W. Jacobs-Perkins, R. T. Janezic, J. H. Kelly, O. M. Mannion, A. Maximov, F. J. Marshall, D. T. Michel, S. Miller, S. F. B. Morse, J. Palastro, J. Peebles, P. B. Radha, S. P. Regan, S. Sampat, T. C. Sangster, A. B. Sefkow, W. Seka, R. C. Shah, W. T. Shmayda, A. Shvydky, C. Stoeckl, A. A. Solodov, W. Theobald, J. D. Zuegel, M. Gatu Johnson, R. D. Petrasso, C. K. Li, and J. A. Frenje, "Tripled Yield in Direct-Drive Laser Fusion Through Statistical Modelling," Nature **565**, 581 (2019).

M. G. Gorman, A. L. Coleman, R. Briggs, R. S. McWilliams, A. Hermann, D. McGonegle, C. A. Bolme, A. E. Gleason, E. Galtier, H. J. Lee, E. Granados, E. E. McBride, S. Rothman, D. E. Fratanduono, R. F. Smith, G. W. Collins, J. H. Eggert, J. S. Wark, and M. I. McMahon, "Recovery of Metastable Dense Bi Synthesized by Shock Compression," Appl. Phys. Lett. **114**, 120601 (2019).

R. J. Henchen, M. Sherlock, W. Rozmus, J. Katz, P. E. Masson-Laborde, D. Cao, J. P. Palastro, and D. H. Froula, "Measuring Heat Flux from Collective Thomson Scattering with Non-Maxwellian Distribution Functions," Phys. Plasmas **26**, 032104 (2019) (invited).

D. P. Higginson, J. S. Ross, D. D. Ryutov, F. Fiuza, S. C. Wilks, E. P. Hartouni, R. Hatarik, C. M. Huntington, J. Kilkenny, B. Lahmann, C. K. Li, A. Link, R. D. Petrasso, B. B. Pollock, B. A. Remington, H. G. Rinderknecht, Y. Sakawa, H. Sio, G. F. Swadling, S. Weber, A. B. Zylstra, and H.-S. Park, "Kinetic Effects on Neutron Generation in Moderately Collisional Interpenetrating Plasma Flows," Phys. Plasmas **26**, 012113 (2019).

D. M. H. Hung, E. G. Blackman, K. J. Caspary, E. P. Gilson, and H. Ji, "Experimental Confirmation of the Standard Magnetorotational Instability Mechanism with a Spring-Mass Analogue," Commun. Phys. **2**, 7 (2019).

A. Kar, T. R. Boehly, P. B. Radha, D. H. Edgell, S. X. Hu, P. M. Nilson, A. Shvydky, W. Theobald, D. Cao, K. S. Anderson, V. N. Goncharov, and S. P. Regan, "Simulated Refraction-Enhanced X-Ray Radiography of Laser-Driven Shocks," Phys. Plasmas **26**, 032705 (2019).

P. M. King, N. Lemos, J. L. Shaw, A. L. Milder, K. A. Marsh, A. Pak, B. M. Hegelich, P. Michel, J. Moody, C. Joshi, and F. Albert, "X-Ray Analysis Methods for Sources from Self-Modulated Laser Wakefield Acceleration Driven by Picosecond Lasers," Rev. Sci. Instrum. **90**, 033503 (2019).

P. F. Knapp, M. R. Gomez, S. B. Hansen, M. E. Glinsky, C. A. Jennings, S. A. Slutz, E. C. Harding, K. D. Hahn, M. R. Weis, M. Evans, M. R. Martin, A. J. Harvey-Thompson, M. Geissel, I. C. Smith, D. E. Ruiz, K. J. Peterson, B. M. Jones, J. Schwartz, G. A. Rochau, D. B. Sinars, R. D. McBride, and P.-A. Gourdain, "Origins and Effects of Mix on Magnetized Liner Inertial Fusion Target Performance," Phys. Plasmas **26**, 012704 (2019).

K. Kopp and S. G. Demos, "Microscopy with Ultraviolet Surface Excitation (MUSE) Enables Translation of Optical Biopsy Principles to Enhance Life Science Education," Proc. SPIE **10873**, 108731D (2019).

A. Koroliov, G. Chen, K. M. Goodfellow, A. N. Vamivakas, Z. Staniszewski, P. Sobolewski, M. El Fray, A. Łaszcz, A Czerwinski, C. P. Richter, and R. Sobolewski, "Terahertz Time-Domain Spectroscopy of Graphene Nanoflakes Embedded in Polymer Mix," Appl. Sci. **9**, 391 (2019).

A. A. Kozlov, J. C. Lambropoulos, J. B. Oliver, B. N. Hoffman, and S. G. Demos, "Mechanisms of Picosecond Laser-Induced Damage in Common Multilayer Dielectric Coatings," Sci. Rep. **9**, 607 (2019).

B. E. Kruschwitz, J. Kwiatkowski, C. Dorrer, M. Barczys, A. Consentino, D. H. Froula, M. J. Guardalben, E. M. Hill, D. Nelson, M. J. Shoup III, D. Turnbull, L. J. Waxer, and D. Weiner, "Tunable UV Upgrade on OMEGA EP," Proc. SPIE **10898**, 1089804 (2019).

A. S. Liao, S. Li, H. Li, K. Flippo, D. Barnak, K. Van Kelso, C. F. Kawaguchi, A. Rasmus, S. Klein, S. Klein, J. Levesque, C. Kuranz, and C. K. Li, "Design of a New Turbulent Dynamo Experiment on the OMEGA-EP," Phys. Plasmas **26**, 032306 (2019).

Y. Lu, P. Tzeferacos, E. Liang, R. K. Follett, L. Gao, A. Birkel, D. H. Froula, W. Fu, H. Ji, D. Lamb, C. K. Li, H. Sio, R. Petrasso, and M. S. Wei, "Numerical Simulation of Magnetized Jet Creation Using a Hollow Ring of Laser Beams," Phys. Plasmas **26**, 022902 (2019).

A. Macrander, N. Pereira, C. Stoeckl, X. Huang, and E. Kasman, "Quartz Conditioning Crystal for X-Ray Rocking Curve Topography," J. Appl. Cryst. **52**, 115 (2019).

P. Michel, M. J. Rosenberg, W. Seka, A. A. Solodov, R. W. Short, T. Chapman, C. Goyon, N. Lemos, M. Hohenberger, J. D. Moody, S. P. Regan, and J. F. Myatt, "Theory and Measurements of Convective Raman Side Scatter in Inertial Confinement Fusion Experiments," Phys. Rev. E **99**, 033203 (2019).

A. L. Milder, S. T. Ivancic, J. P. Palastro, and D. H. Froula, "Impact of Non-Maxwellian Electron Velocity Distribution Functions on Inferred Plasma Parameters in Collective Thomson Scattering," Phys. Plasmas **26**, 022711 (2019).

R. Paul, S. X. Hu, and V. V. Karasiev, "Anharmonic and Anomalous Trends in the High-Pressure Phase Diagram of Silicon," Phys. Rev. Lett. **122**, 125701 (2019).

M. J. Rosenberg, R. Epstein, A. A. Solodov, W. Seka, J. F. Myatt, P. A. Michel, M. A. Barrios, D. B. Thorn, M. Hohenberger, J. D. Moody, and S. P. Regan, "X-Ray Spectroscopy of Planar Laser-Plasma Interaction Experiments at the National Ignition Facility," Phys. Plasmas **26**, 012703 (2019).

M. J. Rosenberg, D. B. Thorn, N. Izumi, D. Williams, M. Rowland, G. Torres, M. Haugh, P. Hillyard, N. Adelman, T. Schuler, M. A. Barrios, J. P. Holder, M. B. Schneider, K. B. Fournier, D. K. Bradley, and S. P. Regan, "Image-Plate Sensitivity to X Rays at 2 to 60 keV," Rev. Sci. Instrum. **90**, 013506 (2019).

M. Sadek and H. Aluie, "Extracting the Spectrum of a Flow by Spatial Filtering," Phys. Rev. Fluids **3**, 124610 (2018).

J. Serafini, A. Hossain, R. B. James, S. B. Trivedi, and R. Sobolewski, "Time-Resolved, Nonequilibrium Carrier and Coherent Acoustic Phonon Dynamics in (Cd,Mg)Te Single Crystals for Radiation Detectors," Semicond. Sci. Technol. **34**, 035021 (2019).

H. Sio, J. A. Frenje, A. Le, S. Atzeni, T. J. T. Kwan, M. Gatu Johnson, G. Kagan, C. Stoeckl, C. K. Li, C. E. Parker, C. J. Forrest, V. Glebov, N. V. Kabadi, A. Bose, H. G. Rinderknecht, P. Amendt, D. T. Casey, R. Mancini, W. T. Taitano, B. Keenan, A. N. Simakov, L. Chacón, S. P. Regan, T. C. Sangster, E. M. Campbell, F. H. Seguin, and R. D. Petrasso, "Observations of Multiple Nuclear Reaction Histories and Fuel-Ion Species Dynamics in Shock-Driven Inertial Confinement Fusion Implosions," Phys. Rev. Lett. **122**, 035001 (2019).

R. B. Spielman and D. B. Reisman, "On the Design of Magnetically Insulated Transmission Lines for *Z*-Pinch Loads," Matter Radiat. Extremes **4**, 027402 (2019).

L. J. Waxer, K. A. Bauer, E. C. Cost, M. Heimbueger, J. H. Kelly, V. Kobilansky, S. F. B. Morse, D. Nelson, R. Peck, R. Rinefierd, S. Sampat, M. J. Shoup III, D. Weiner, G. Weselak, and J. Zou, "In-Tank, On-Shot Characterization of the OMEGA Laser System Focal Spot," Proc. SPIE **10898**, 108980F (2019).

B. Webb, M. J. Guardalben, C. Dorrer, S. Bucht, and J. Bromage, "Simulation of Grating Compressor Misalignment Tolerances and Mitigation Strategies for Chirped-Pulse–Amplification Systems of Varying Bandwidths and Beam Sizes," Appl. Opt. **58**, 234 (2019).

J. Xin, R. Yan, Z.-H. Wan, D.-J. Sun, J. Zheng, H. Zhang, H. Aluie, and R. Betti, "Two Mode Coupling of the Ablative Rayleigh-Taylor Instabilities," Phys. Plasmas **26**, 032703 (2019).

R. P. Young, C. C. Kuranz, D. Froula, J. S. Ross, and S. Klein, "Observation of Collisionless-to-Collisional Transition in Col-

liding Plasma Jets with Optical Thomson Scattering," Phys. Plasmas **26**, 012101 (2019).

M. Zaghoo, T. R. Boehly, J. R. Rygg, P. M. Celliers, S. X. Hu, and G. W. Collins, "Breakdown of Fermi Degeneracy in the Simplest Liquid Metal," Phys. Rev. Lett. **122**, 085001 (2019).

X. Zhang, Y. Zhang, and M. Z. Yates, "Hydroxyapatite Nanocrystal Deposited Titanium Dioxide Nanotubes Loaded with Antibiotics for Combining Biocompatibility and Antibacterial Properties," MRS Advances **3**, 1703 (2018).

Forthcoming Publications

X. Bian and H. Aluie, "Decoupled Cascades of Kinetic and Magnetic Energy in Magnetohydrodynamic Turbulence," to be published in Physical Review Letters.

D. Broege and J. Bromage, "Measurements of Heat Flow from Surface Defects in Lithium Triborate," to be published in Optics Express.

D. Broege, S. Fochs, G. Brent, J. Bromage, C. Dorrer, R. F. Earley, M. J. Guardalben, J. A. Marozas, R. G. Roides, J. Sethian, X. Wang, D. Weiner, J. Zweiback, and J. D. Zuegel, "The Dynamic Compression Sector Laser: A 100-J UV Laser for Dynamic Compression Research," to be published in Review of Scientific Instruments.

M. Chorel, S. Papernov, A. A. Kozlov, B. N. Hoffman, J. B. Oliver, S. G. Demos, T. Lanternier, É. Lavastre, L. Lamaignère, N. Roquin, B. Bousquet, N. Bonod, and J. Néauport, "The Influence of Absorption-Edge Properties on Subpicosecond Intrinsic Laser-Damage Threshold at 1053 nm in Hafnia and Silica Monolayers," to be published in Optics Express.

A. S. Davies, D. Haberberger, J. Katz, S. Bucht, J. P. Palastro, W. Rozmus, and D. H. Froula, "Picosecond Thermodynamics in Underdense Plasmas Measured with Thomson Scattering," to be published in Physical Review Letters.

S. G. Demos, B. N. Hoffman, C. W. Carr, D. A. Cross, R. A. Negres, and J. D. Bude, "Mechanisms of Laser-Induced Damage in Absorbing Glasses with Nanosecond Pulses," to be published in Optics Express.

L. Divol, D. P. Turnbull, T. Chapman, C. Goyon, and P. Michel, "An Analytical Study of Non-Resonant Transient Cross-Beam Power Transfer Relevant to Recent Progress in Plasma Photonics," to be published in Physics of Plasmas.

C. Dorrer, "Spatiotemporal Metrology of Broadband Optical Pulses," to be published in IEEE Journal on Selected Topics in Quantum Electronics.

C. Fagan, M. Sharpe, W. T. Shmayda, and W. U. Schröder, "Tritium Retention in Hexavalent Chromate-Conversion–Coated Aluminum Alloy," to be published in Fusion Science and Technology.

R. Ghosh, O. Swart, S. Westgate, B. L. Miller, and M. Z. Yates, "Antibacterial Copper–Hydroxyapatite Composite Coatings via Electrochemical Synthesis," to be published in Langmuir.

K. R. P. Kafka and S. G. Demos, "Interaction of Short Laser Pulses with Model Contamination Microparticles on a High Reflector," to be published in Optics Letters.

V. V. Karasiev, S. B. Trickey, and J. W. Dufty, "Status of Free-Energy Representations for Homogeneous Electron Gas," to be published in Physical Review B.

S. Le Pape, L. Divol, A. Macphee, J. McNaney, M. Hohenberger, D. Froula, V. Glebov, O. L. Landen, C. Stoeckl, E. Dewald, S. Khan, C. Yeamans, P. Michel, M. Schneider, J. Knauer, J. Kilkenny, and A. J. Mackinnon, "Optimization of High Energy X Ray Production Through Laser Plasma Interaction," to be published in High Energy Density Physics.

M. Millot, F. Coppari, J. R. Rygg, A. Correa Barrios, S. Hamel, D. C. Swift, and J. H. Eggert, "Nanosecond X-Ray Diffraction of Shock-Compressed Superionic Water Ice," to be published in Nature.

S. Papernov, "Spectroscopic Setup for Submicrometer-Resolution Mapping of Low-Signal Absorption and Luminescence Using Photothermal Heterodyne Imaging and Photon-Counting Techniques," to be published in Applied Optics.

S. Sampat, T. Z. Kosc, K. A. Bauer, R. D. Dean, W. R. Donaldson, J. Kwiatkowski, R. Moshier, A. L. Rigatti, M. H. Romanofsky, L. J. Waxer, and J. H. Kelly, "Power Balancing a Multibeam Laser," to be published in the Proceedings of SPIE.

J. P. Sauppe, B. M. Haines, S. Palaniyappan, P. A. Bradley, S. H. Batha, E. N. Loomis, and J. L. Kline, "Modeling of Direct-Drive Cylindrical Implosion Experiments with an Eulerian Radiation-Hydrodynamics Code," to be published in Physics of Plasmas.

R. Sobolewski, "Optical Sensors," to be published in the Handbook of Superconducting Materials.

M. Stoeckl and A. A. Solodov, "Refining Instrument Response Functions with 3-D Monte Carlo Simulations of Differential Hard X-Ray Spectrometers," to be published in Nuclear Instruments and Methods in Physics Research, A.

S. Zhang, A. Lazicki, B. Militzer, L. H. Yang, K. Caspersen, J. A. Gaffney, M. W. Däne, J. E. Pask, W. R. Johnson, A.Sharma, P. Suryanarayana, D. D. Johnson, A. V. Smirnov, P. A. Sterne, D. Erskine, R. A. London, F. Coppari, D. Swift, J. Nilsen, A. J. Nelson, and H. D. Whitley, "Equation of State of Boron Nitride Combining Computation, Modeling, and Experiment," to be published in Physical Review B.

Conference Presentations

M. Wei, "LaserNetUS Facility Readiness—Omega Laser Facility," presented at the LaserNetUS PI Meeting, Rockville, MD, 16 January 2019.

The following presentations were made at the Japan–U.S. Symposium, Washington, DC, 23–24 January 2019:

G. W. Collins, "Forging a New Frontier of HED Science Through Japan–U.S. Collaborations."

D. H. Froula, "Japan–U.S. Collaborations—Future Collaborations and the Direction of LLE Laser Science and Plasma Physics Research."

E. M. Campbell, "Fusion: Making a Star on Earth and the Quest for the Ultimate Energy Source to Power the Planet," presented at the Cornell University Seminar, Ithaca, NY, 31 January 2019.

The following presentations were made at LASE 2019, San Francisco, CA, 2–7 February 2019:

K. A. Bauer, M. Heimbueger, S. Sampat, L. J. Waxer, E. C. Cost, J. H. Kelly, V. Kobilansky, J. Kwiatkowski, S. F. B. Morse, D. Nelson, D. Weiner, G. Weselak, and J. Zou, "Comparison of On-Shot, In-Tank, and Equivalent-Target-Plane Measurements of the OMEGA Laser System Focal Spot."

W. R. Donaldson and A. Consentino, "Co-Timing UV and IR Laser Pulses on the OMEGA EP Laser System."

B. E. Kruschwitz, J. Kwiatkowski, C. Dorrer, M. Barczys, A. Consentino, D. H. Froula, M. J. Guardalben, E. M. Hill, D. Nelson, M. J. Shoup III, D. Turnbull, L. J. Waxer, and D. Weiner, "Tunable UV Upgrade on OMEGA EP."

S. Sampat, T. Z. Kosc, K. A. Bauer, R. D. Dean, W. R. Donaldson, J. Kwiatkowski, R. Moshier, A. L. Rigatti, M. H. Romanofsky, L. J. Waxer, and J. H. Kelly, "Power Balancing a Multibeam Laser."

L. J. Waxer, K. A. Bauer, E. C. Cost, M. Heimbueger, J. H. Kelly, V. Kobilansky, S. F. B. Morse, D. Nelson, R. Peck, R. Rinefierd, S. Sampat, M. J. Shoup III, D. Weiner, G. Weselak, and J. Zou, "In-Tank, On-Shot Characterization of the OMEGA Laser System Focal Spot."

The following presentations were made at Photonics West, San Francisco, CA, 2–7 February 2019:

I. A. Begishev, M. H. Romanofsky, S. Carey, R. Chapman, G. Brent, M. J. Shoup III, J. D. Zuegel, and J. Bromage, "High-Efficiency, Large-Aperture Fifth-Harmonic–Generation of

211-nm Pulses in Ammonium Dihydrogen Phosphate Crystals for Fusion Diagnostics."

K. Kopp and S. G. Demos, "Microscopy with Ultraviolet Surface Excitation (MUSE) Enables Translation of Optical Biopsy Principles to Enhance Life Science Education."

T. Z. Kosc, T. J. Kessler, H. Huang, R. A. Negres, and S. G. Demos, "Raman Scattering Cross-Section Measurements Using KDP Polished Crystal Spheres to Understand Transverse Stimulated Raman Scattering."

S. P. Regan, R. Epstein, M. Bedzek, R. Betti, T. R. Boehly, M. Bonino, N. Chartier, G. W. Collins, J. A. Delettrez, D. H. Froula, V. Yu. Glebov, V. N. Goncharov, S. X. Hu, I. V. Igumenshchev, D. R. Harding, J. P. Knauer, M. Lawrie, F. J. Marshall, D. T. Michel, P. B. Radha, M. J. Rosenberg, J. R. Rygg, R. Saha, R. C. Shah, M. J. Shoup III, C. Stoeckl, T. C. Sangster, W. Theobald, E. M. Campbell, H. Sawada, R. C. Mancini, K. Falk, E. Rowe, J. Topp-Mugglestone, P. Kozlowski, G. Gregori, J. Wark, J. A. Frenje, M. Gatu Johnson, N. Kabadi, C. K. Li, H. Sio, R. D. Petrasso, P. Keiter, P. X. Belancourt, R. P. Drake, N. Woolsey, I. E. Golovkin, J. J. MacFarlane, S. H. Glenzer, B. A. Hammel, L. J. Suter, S. Ayers, M. A. Barrios, P. M. Bell, D. K. Bradley, M. J. Edwards, K. B. Fournier, S. W. Haan, O. A. Hurricane, C. A. Iglesias, N. Izumi, O. L. Landen, D. Larson, A. Nikroo, M. Schneider, H. A. Scott, T. Ma, P. K. Patel, D. Thorn, B. G. Wilson, D. A. Haynes, D. D. Meyerhofer, H. Huang, J. Jaquez, J. D. Kilkenny, L. Gao, K. Hill, B. Kraus, P. Efthimion, Y. Lu, X. Huang, and P. Fan, "X-Ray Spectroscopy and Inertial Confinement Fusion," presented at the University of Nebraska, Lincoln, NE, 13 February 2019.

E. M. Campbell, "Fusion: Making a Star on Earth and the Quest for the Ultimate Energy Source to Power the Planet," presented at SUNY Geneseo Seminar, Geneseo, NY, 14 February 2019.

E. M. Campbell, "Fusion: Making a Star on Earth and the Quest for the Ultimate Energy Source to Power the Planet," presented at the ASME Student Banquet, Rochester, NY, 15 February 2019.

M. S. Wei, "LaserNetUS-OMEGA EP Laser System and Experimental Capability," presented at LaserNetUS, Virtual Meeting, 15 February 2019.

The following presentations were made at the 59th Sanibel Symposium, St. Simons Island GA, 17–22 February 2019:

J. Hinz, V. V. Karasiev, S. X. Hu, M. Zaghoo, and D. Mejia-Rodriguez, "Deorbitalized Meta-GGA with the Long-Range van der Waals Exchange-Correlation Functional Calculations of the Insulator–Metal Transition of Hydrogen."

V. V. Karasiev, S. X. Hu, M. Zaghoo, T. R. Boehly, S. B. Trickey, and J. W. Dufty, "Exchange-Correlation Thermal Effects: Softening the Deuterium Hugoniot and Thermophysical Properties."

R. Paul, V. V. Karasiev, and S. X. Hu, "High-Pressure Phases and Spectral Properties of Silicon."

J. L. Peebles, J. R. Davies, R. Moshier, M. Bradley, T. Nguyen, G. Weselak, G. Fiksel, R. Shapovalov, R. Spielman, G. Brent, D. W. Jacobs-Perkins, A. Bose, M. Gatu Johnson, C. K. Li, J. A. Frenje, R. D. Petrasso, and R. Betti, "Magnetizing 60-Beam Spherical Implosions on OMEGA," presented at the 2019 Stewardship Science Academic Programs Symposium, Albuquerque, NM, 19–20 February 2019.

E. M. Campbell, "LLE Priorities FY2020–FY2021," presented at the ICF Executives Meeting, Albuquerque, NM, 21–22 February 2019.

G. W. Collins, "Extreme Matters: A Laboratory Exploration of Planets, Stars, and Quantum Matter," presented at the Phelps Colloquium, Rochester, NY, 27 February 2019.

G. W. Collins, J. R. Rygg, T. R. Boehly, M. Zaghoo, D. N. Polsin, B. J. Henderson, X. Gong, L. Crandall, R. Saha, J. J. Ruby, G. Tabak, M. F. Huff, Z. K. Sprowal, D. A. Chin,

M. K. Ginnane, P. M. Celliers, J. H. Eggert, A. Lazicki, R. F. Smith, R. Hemley, F. Coppari, B. Bachmann, J. Gaffney, D. E. Fratanduono, D. G. Hicks, Y. Ping, D. Swift, D. G. Braun, S. Hamel, M. Millot, M. Gorman, R. Briggs, S. Ali, R. Kraus, P. Loubeyre, S. Brygoo, R. Jeanloz, R. Falcone, M. McMahon, F. N. Beg, C. Bolme, A. Gleason, S. Glenzer, H. Lee, T. Duffy, J. Wang, J. Wark, and G. Gregori, "Laser Focus on Planets: Exploring Planets and Stars Through High Energy Density Science," presented at the APS March Meeting, Boston, MA, 4–8 March 2019.

The following presentations were made at Matter in Extreme Conditions from Material Science to Planetary Physics, Montgenevre, France, 17–23 March 2019:

G. W. Collins, J. R. Rygg, T. R. Boehly, M. Zaghoo, D. N. Polsin, B. J. Henderson, X. Gong, L. E. Crandall, R. Saha, J. J. Ruby, G. Tabak, M. F. Huff, Z. K. Sprowal, D. A. Chin, M. K. Ginnane, P. M. Celliers, J. H. Eggert, A. Lazicki, R. F. Smith, R. Hemley, F. Coppari, B. Bachman, J. Gaffney, D. E. Fratanduono, D. G. Hicks, Y. Ping, D. Swift, D. G. Braun, S. Hamel, M. Millot, M. Gorman, R. Briggs, S. Ali, R. Kraus, P. Loubeyre, S. Brygoo, R. Jeanloz, R. Falcone, M. McMahon, F. N. Beg, C. Bolme, A. Gleason, S. H. Glenzer, H. Lee, T. Duffy, J. Wang, J. Wark, and G. Gregori, "Shock Physicists: Today's Explorers of the Universe."

B. J. Henderson, M. Zaghoo, X. Gong, D. N. Polsin, J. R. Rygg, T. R. Boehly, G. W. Collins, S. Ali, P. M. Celliers, A. E. Lazicki, M. Gorman, M. Millot, J. H. Eggert, and M. McMahon, "Broadband Reflectivity Diagnostic Development for Dynamic Compression Experiments on OMEGA EP."

J. R. Rygg, D. N. Polsin, X. Gong, T. R. Boehly, G. W. Collins, S. P. Regan, C. Sorce, J. H. Eggert, R. Smith, A. Lazicki, M. Ahmed, A. Arsenlis, M. A. Barrios, J. Bernier, K. Blobaum, D. G. Braun, R. Briggs, P. M. Celliers, A. Cook, F. Coppari, D. E. Fratanduono, M. Gorman, B. Heidl, M. Hohenberger, D. H. Kalantar, S. Khan, R. Kraus, J. McNaney, D. Swift, J. Ward, C. Wehrenberg, A. Higginbothom, M. Suggit, J. Wark, J. Wang, T. Duffy, J. Wicks, and M. McMahon, "X-Ray Diffraction in the Terapascal Regime."

W. T. Shmayda, C. Fagan, and R. C. Shmayda, "Reducing Releases from Tritium Facilities," presented at the First Tritium School, Ljubljana, Slovenia, 25–28 March 2019.

The following presentations were made at the International Conference on High Energy Density Science, Oxford, UK, 31 March–5 April 2019:

R. Betti, "Recent Advances in Direct-Drive Laser Fusion."

S. X. Hu, Y. H. Ding, V. V. Karasiev, R. Paul, M. Ghosh, J. Hinz, P. M. Nilson, T. R. Boehly, P. B. Radha, V. N. Goncharov, S. Skupsky, J. R. Rygg, G. W. Collins, S. P. Regan, E. M. Campbell, L. A. Collins, J. D. Kress, A. J. White, O. Certik, and B. Militzer, "Warming Up Density Functional Theory (DFT) for High-Energy-Density Plasmas."

D. N. Polsin, X. Gong, M. F. Huff, L. E. Crandall, G. W. Collins, T. R. Boehly, J. R. Rygg, A. Lazicki, M. Millot, P. M. Celliers, J. H. Eggert, and M. I. McMahon, "High-Pressure Structural and Electronic Properties of Ramp-Compressed Sodium."


1850
MELIORA
UNIVERSITY of
ROCHESTER